Title
Heat Transfer in Pebble-Bed Nuclear Reactor Cores Cooled by Fluoride Salts

Author
Huddar, Lakshana Ravindranath

Publication Date
2016

Peer reviewed|Thesis/dissertation

Heat Transfer in Pebble-Bed Nuclear Reactor Cores Cooled by Fluoride Salts

By

Lakshana Ravindranath Huddar

A dissertation submitted in partial satisfaction of the
requirements for the degree of
Doctor of Philosophy

in

Engineering – Nuclear Engineering

in the

Graduate Division

of the

University of California, Berkeley

Committee in charge:

Professor Per F. Peterson
Professor Massimiliano Fratoni
Professor Ralph Greif

Fall 2016

Heat Transfer in Pebble-Bed Nuclear Reactor Cores Cooled by Fluoride Salts

By

Lakshana Ravindranath Huddar

ABSTRACT

Heat Transfer in Pebble-Bed Nuclear Reactor Cores Cooled by Fluoride Salts

By
Lakshana Ravindranath Huddar

Doctor of Philosophy in Engineering – Nuclear Engineering
University of California, Berkeley

Professor Per F. Peterson, Chair

With electricity demand predicted to rise by more than 50% within the next 20 years and a burgeoning world population requiring reliable emissions-free base-load electricity, can we design advanced nuclear reactors to help meet this challenge? At the University of California, Berkeley (UCB) Fluoride-salt-cooled High Temperature Reactors (FHR) are currently being investigated. FHRs are designed with better safety and economic characteristics than conventional light water reactors (LWR) currently in operation. These reactors operate at high temperature and low pressure making them more efficient and safer than LWRs. The pebble-bed FHR (PB-FHR) variant includes an annular nuclear reactor core that is filled with randomly packed pebble fuel. It is crucial to characterize the heat transfer within this unique geometry as this informs the safety limits of the reactor. The work presented in this dissertation focused on furthering the understanding of heat transfer in pebble-bed nuclear reactor cores using fluoride salts as a coolant. This was done through experimental, analytical and computational techniques.

A complex nuclear system with a coolant that has never previously been in commercial use requires experimental data that can directly inform aspects of its design. It is important to isolate heat transfer phenomena in order to understand the underlying physics in the context of the PB-FHR, as well as to make decisions about further experimental work that needs to be done in support of developing the PB-FHR. Certain organic oils can simulate the heat transfer behaviour of the fluoride salt if relevant non-dimensional parameters are matched. The advantage of this method is that experiments can be done at a much lower temperature and at a smaller geometric scale compared to FHRs, thereby lowering costs. In this dissertation, experiments were designed and performed to collect data demonstrating similitude. The limitations of these experiments were also elucidated by underlining key distortions between the experimental and the prototypical conditions.

This dissertation is broadly split into four parts. Firstly, the heat transfer phenomenology in the PB-FHR core was outlined. Although the viscous dissipation term and the thermal diffusion term (including thermal dispersion) were similar in magnitude, they were overshadowed by the advection term which was about 10^4 times bigger during normal operation and 10^5 times bigger during accident transients in which natural circulation becomes the main mode of fluid flow. Thus it is safe to neglect the viscous dissipation and the thermal diffusion terms in the PB-FHR core without a significant loss of accuracy.

Secondly, separate effects tests (SET) were performed using simulant oils, and the results were compared to the prototypical conditions using flinak as the fluoride salt. The main purpose of these experiments was to study natural convection heat transfer and identify any distortions between the two cases. An isolated copper sphere was immersed in flinak and a parallel experiment was performed using simulant oil. A large discrepancy between the flinak and the oil was noted, due to distortions from assuming quasi-steady state conditions. A steady state experiment using a cylindrical heater immersed in oil was also performed, and the results compared to a similar experiment done at Oak Ridge National Laboratory (ORNL) using flinak. The Nusselt numbers matched within 10% for laminar flows. This supports the conclusion that natural convection similitude does exist for oils used in scaled experiments, allowing natural convection data to be used for for FHR and MSR modeling. This is important, due to the lack of significant experimental data showing natural convection in fluoride salts, so these SETs add to the overall understanding of their heat transfer properties.

With the knowledge of the distortions between the oil and the salt, an experiment to measure heat transfer coefficients within a pebble-bed test section was designed, constructed and performed. Oil was pumped through a test section filled with randomly packed copper spheres. The temperature of the oil was pulsed at a constant frequency, which caused a temperature difference between the pebbles and the oil. An excellent match was found between the measured heat transfer coefficients and the literature. This data provides an essential closure parameter for multiphysics modeling of the PB-FHR. Using frequency response techniques in scaled experiments is an innovative approach for extracting dynamic responses to coolant-structure interactions. Finally, an integrated model of the passive decay heat removal system was presented using Flownex and the simulations compared to experimental data. A good match was found with the data, which was within 14%.

The work presented in this dissertation shows fundamental details on heat transfer in the PB-FHR core using experimental data and simulations, leading us closer to developing advanced nuclear reactors that can later be commercialized. Advanced nuclear reactors

such as the PB-FHR have immense potential in reducing greenhouse gas emissions and combating climate change while being exceedingly safe and providing reliable electricity.

:||: श्री :||:

To my grandfather Narasimha Konnur.
In loving memory of my grandparents, Anantrao Huddar, Mahalakshmi Huddar and Mandakini Konnur.
You all have taught me so much since I was a little girl, and your lessons will stay with me forever.

ACKNOWLEDGEMENTS

Back in 2011, I never imagined the day would come when I would write the acknowledgements page of my PhD dissertation. I never even believed I would make it this far. Every time things got tough I wondered what my life would have been like if I hadn't turned down that lucrative job offer from an oil company. But if I had accepted it, I wouldn't have learned about how fascinating advanced nuclear reactors are, and what unlimited potential they have to protect our world. I wouldn't have been able to travel to all corners of the country to learn about them in depth, and apply that knowledge to my own research. And most importantly, I wouldn't have met all the people who truly believed in me and my work, and knew I would one day earn that PhD.

I am so grateful to my PhD advisor, Professor Per Peterson, for teaching me everything I know about conducting research with integrity, about leadership, and about the importance of being unfailingly enthusiastic about new ideas. I learned neutronics from Prof Max Fratoni, and he was truly one of the best teachers I had at UC Berkeley. I really appreciated the advice and insight from Prof Ralph Greif, who is always so positive and kind.

My parents Ravi and Anjali Huddar have been my most supportive, patient, and encouraging cheerleaders throughout grad school. Their excitement and curiosity at every small step of progress I made pushed me to go further and make them proud. My little sister Prerana Huddar calmly listened to all my problems even though she works a job that is at least one hundred times more challenging and stressful. She truly deserved to win the competition of which Huddar sister gets to be addressed as 'Doctor' first.

I owe my success and sanity to my close-knit and supportive group of friends from the Nuclear Engineering department. I always enjoyed the stimulating conversations about anything and everything with Alejandra Jolodosky on our weekly walks/hikes. Madicken Munk's humor, liveliness and courageous attitude always put me at ease. I learned so much from Patricia Schuster especially when preparing for talks together, travelling abroad together or just hanging out together.

I am indebted all my mentors and peers from the Thermal Hydraulics Lab. Nicolas Zweibaum, Harry Andreades and Raluca Scarlat were formative during my early years as a grad student. It was wonderful getting to know the younger students, especially

Andrew Greenop, Brian He, James Kendrick, April Novak, Chris Poresky and Xin Wang. They made 4118 Etcheverry Hall a lot brighter, even though it is a room with no windows. Jeff Bickel was instrumental in getting PBHTX up and running. My inexperience must have frustrated him but I learned so much in the process, and I hope he knows how thankful I am.

Without the help of my undergraduate students I'm fairly sure I would have never reached this point. They are resourceful, tenacious and inquisitive - all key qualities any budding researcher needs. I especially want to thank Connie Lee, AJ Albaaj, Felicia Sutanto, Brandon Kuhnert for helping with PBHTX and CHEX. Sea Hong was invaluable during the isolated pebble tests and Makoto Lalwani helped with the Flownex models.

I owe a debt of gratitude to my cousin Vasudha Shivamoggi. Without her I probably would not have considered applying for a PhD at UC Berkeley. Her perspicacious advice and kind personality sustained me when I doubted myself. I am extremely grateful to my aunt and uncle Anupama and Parag Hukeri, who helped me get settled in the United States when I first arrived here. It is impossible to list the ways in which they helped me throughout the years. My cousins Payal and Pooja are so energetic and full of life, and brought me so much happiness and optimism. I want to thank my cousin Bhargavi Agnihotri and her husband Prasanna Krishna for always welcoming me on the weekends. Their older son Pareekshith's hunger for new knowledge inspired me to take my mentorship duties seriously. It was such a joy to see their younger son Pradyumna grow from a new born baby, which was when I started the PhD.

I am extremely thankful to my new family, especially my in-laws Desh and Jaishree Deshpande. Their energy and zeal keeps me extremely excited about my post-PhD future. And finally, I want to thank my incredible and brilliant husband Ashwin Deshpande. Our intellectual and silly conversations always cheer me up. The writing period is traditionally very demanding, but every day with him feels like a holiday.

TABLE OF CONTENTS

LIST OF FIGURES

LIST OF TABLES

1. INTRODUCTION

We live in an era of high energy consumption. As the global population grows, electricity demand is expected to increase by two-thirds the current demand by the year 2035 [1], and developing countries will be playing a significant role in this increase [2]. We need to ensure that zero emissions, reliable base load electricity is available to all consumers. Nuclear energy is a crucial part of the solution to the energy crisis we are presently facing. Twenty percent of electricity in the U.S. comes from nuclear power, and accounts for 63% of U.S. low greenhouse gas (GHG) electricity production. Many plants will be decommissioned in the coming decades due to old age. If we want to replace them with more zero emissions power then advanced nuclear reactors are essential to our energy future.

Most of today's operating commercial reactors are water cooled. This technology was optimal for naval submarine use, and this directly influenced the design of civilian power reactors. Gen III+ light water reactors (LWR) such as the AP1000 improve upon previous generations in several key ways. They are designed to be constructed using factory-prefabricated mechanical and structural modules, thereby reducing construction time costs. They are intended to have a sixty-year lifespan, whereas older reactors were designed to operate for forty years. Gen III+ reactors implement passive safety systems. This means that reactors can safely shut down during emergencies without the need for operator intervention or AC power.

However, there is still a potential to improve current nuclear reactor technology in terms of safety and economics. Fluoride-Salt-Cooled High-Temperature Reactors (FHRs) seek to boost economics, efficiency and safety characteristics in comparison to current nuclear reactors on the market, and in comparison to other advanced nuclear reactor designs. FHRs utilize several nuclear innovations that have been tested and implemented in other nuclear reactor designs.

The Pebble-Bed FHR (PB-FHR) is a variant within the FHR class of reactors, with an annular reactor core composed of randomly packed fuel spheres, or 'pebbles'. The PB-FHR is a small modular reactor (SMR). The Mk1 PB-FHR [3] provides an example of a recent design, where reactor module produces 236 megawatt thermal (MWth) of power, which corresponds to about 100 megawatt electric (MWe). Heat is transferred from nuclear fission reactions in the fuel pebbles to a power conversion system via the fluoride salt coolant, flibe, described in section 1.2.1. The power conversion system is a nuclear air combined cycle (NACC).

In order to get PB-FHRs commercialized in the U.S., the design must be licensed by the U.S. Nuclear Regulatory Commission (NRC). This process involves presenting

experimental data and simulations of reactor behavior. This dissertation focuses on showing that simulant oils can be used to develop a thermal hydraulics validation basis for licensing purposes. Additionally, the work presented aims to present a deeper understanding of the heat transfer characteristics of the PB-FHR.

It is in society's best interest to dedicate resources to developing zero emissions technologies, and there has never been a more appropriate time to develop advanced nuclear reactors such as the PB-FHR. There are a multitude of design challenges to overcome before the PB-FHR becomes a reality, but once commercialized it will play a key role in clean and reliable electricity production.

The purpose of Chapter 1 is to present the research motivations and goals, present background material and discuss the implications of the results from a scale analysis of governing equations in the PB-FHR.

1.1 Research Motivation

The key motivation for this dissertation is to present work in support of the development of advanced nuclear reactor technology, PB-FHRs in particular. However there is some overlap between this work and other fields of research.

- Molten salt reactors (MSR) are ones in which the fuel is dissolved in the coolant, a fluoride salt in most designs. Since the focus of the work reported here is in heat transfer in fluoride salts, there will be some applicability to MSRs, especially with regards to potential distortions in SETs
- The common area of interest between PB-FHRs and high temperature gas-cooled reactors (HTR) is the pebble-bed fuel configuration. Experimental techniques outlined in this dissertation may be applicable to gas-cooled reactors as well, especially with regard to dynamic response of heat structures during conjugate heat transfer between fluids and solids
- Packed beds for heat exchangers and thermal energy storage for solar power [4][5]

1.2 Background Review

This section focuses on describing the PB-FHR, introducing key concepts in heat transfer phenomenology in pebble-bed nuclear reactors, and outlining the main research objectives of this dissertation.

1.2.1 Description of the PB-FHR (pebble-bed fluoride-salt-cooled high temperature reactor)

As mentioned in the Introduction, the PB-FHR is a small modular reactor. In the Mark-1 (Mk1) iteration, each unit designed to produce about 100 MWe in base-load operation [6]. The coolant is called flibe, a composition of lithium fluoride and beryllium fluoride ($2LiF$-BeF_2). Flibe is an ideal coolant for an advanced reactor design given its superior convective heat transfer capabilities compared to other reactor coolants such as helium, sodium and water. Its volumetric heat capacity also exceeds that of helium, sodium and water. Figure 1-1 shows a schematic of the Mk1 PB-FHR, including the coolant flow paths. Flibe transports heat produced in the reactor core to the coiled tube air heaters (CTAH), heating the power conversion fluid air. It is interesting to note that there is no secondary salt loop in the system. Air in the heat exchangers is directly heated by the primary circuit flibe coolant.

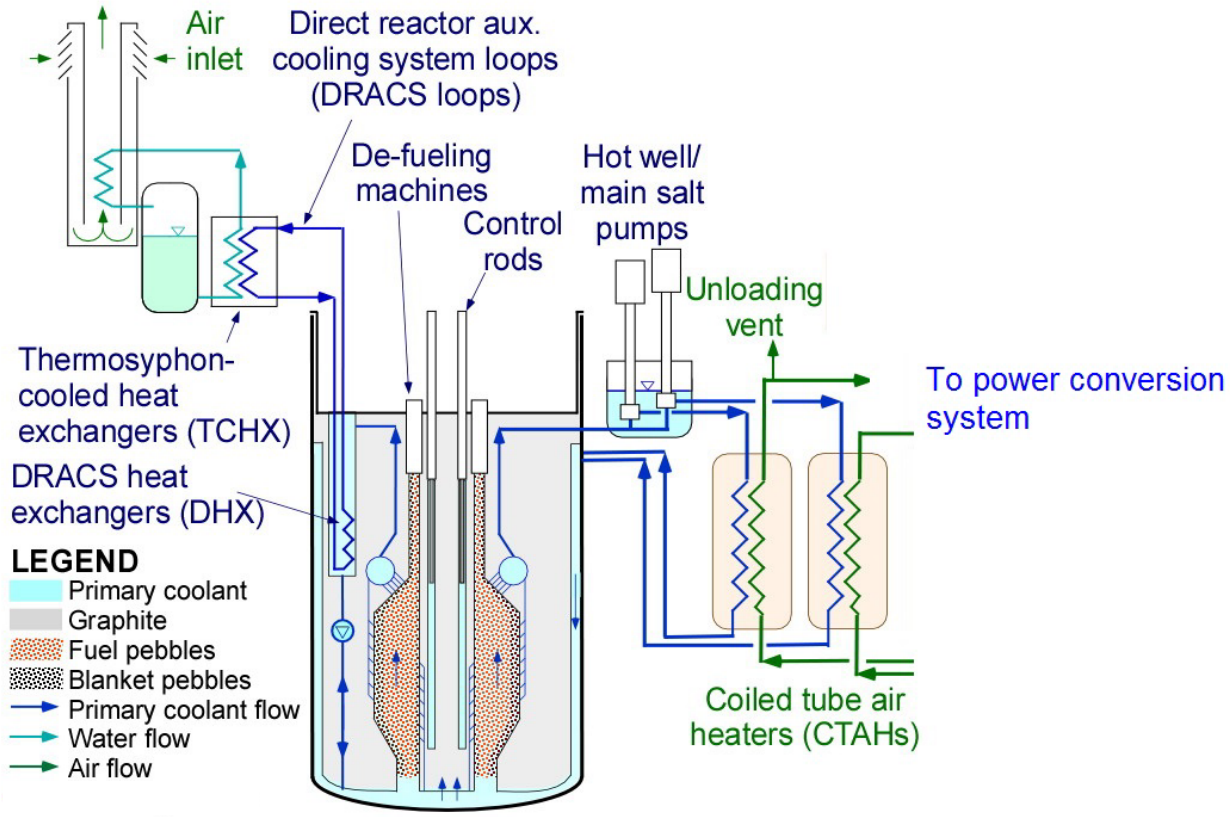

Figure 1-1: Schematic of the PB-FHR main salt loop showing coolant flow paths

Under shutdown conditions, heat is still produced in the reactor core even if the fission reactions have ceased. This is known as decay heat and is about 2-4% of the total operational power immediately after shut down. Decay heat is produced from the radioactive decay of fission products in the fuel. The decay heat must be removed to avoid temperature increases in the core. Under emergency shutdown conditions in the Mk1 PB-FHR, when normal shutdown cooling is not available, decay heat removal is achieved via a passive safety system that relies on natural circulation to induce salt flow through the reactor core. This is called the Direct Reactor Auxiliary Cooling System (DRACS). The Mk1 PB-FHR has three DRACS loops to ensure redundancy in passive safety systems. Flibe is also the working fluid in the DRACS system. The decay heat is ejected to the atmosphere, the final heat sink. The DRACS system is a coupled loop connected by the DRACS heat exchanger (DHX), as shown in Figure 1-1. When the pumps are tripped, the main salt coolant follows the flow path shown in Figure 1-2.

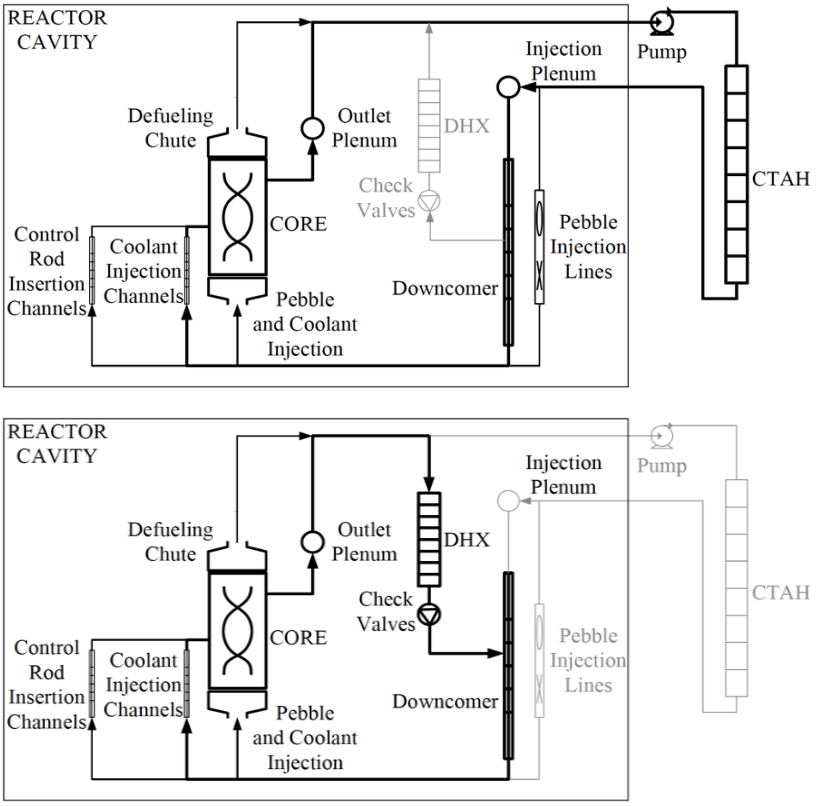

Figure 1-2: Coolant flow path during normal operation and emergency shutdown [6]

Figure 1-3 shows the basic principles of a natural circulation loop. The heat source (in the PBFHR that is the reactor core) is situated at a lower elevation than the heat sink (the DHX). The driving force of the fluid arises due to the difference in density in the loop. The fluid density in the hot leg is lower than in the rest of the loop because of the heat source. As the fluid passes through the heat sink, its density increases as it is cooler. This

change in density causes a pressure differential which is the driving force. In a steady state closed loop system, the buoyancy-driven forces and the friction induced forces are balanced.

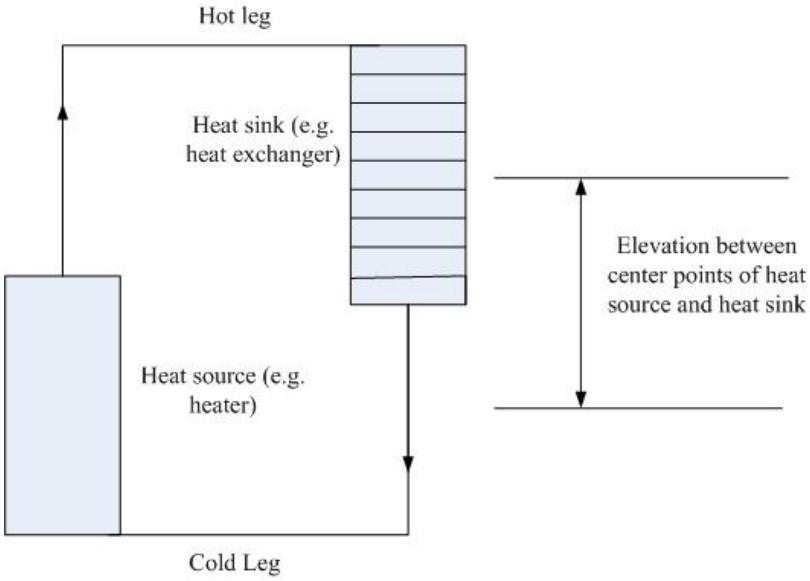

Figure 1-3: Schematic of a general natural circulation loop

Normally, decay heat removal occurs using an active shutdown cooling system that provides controlled heat removal to minimize thermal stresses in the reactor vessel. For emergency passive decay heat removal through the DRACS, natural circulation is established in the primary system, with flow upwards through the core and outlet plenum, then downwards through the DHX, fluidic diode, downcomer and inlet plenum. During normal power operation of the reactor, the primary coolant flows in forced circulation upwards through the core, and a small amount of coolant bypasses the core and flows upwards through the fluid diode and DHX. Figure 1-2 shows a schematic diagram of the coolant flow paths and the bypass flows during forced circulation and natural circulation operational modes. The function of the fluid diode is to provide high flow resistance for upwards flow during forced convection, and low flow resistance for downwards flow during natural circulation.

There are three DRACS loops in the FHR to ensure redundancy, thereby significantly decreasing the risk that decay heat from the reactor cannot be removed. The decay heat from the reactor acts as the heat source and the DRACS heat exchangers (DHX) serve as the heat sinks. Secondary salt loops link the DHXs to the ultimate heat sink. The thermosyphon cooled heat exchangers (TCHXs) that remove heat from the DRACS loops are designed so that the rate of heat removal can be controlled, thereby making it possible to prevent the salt from freezing. This is a concern because the melting point of flibe is high, 459 °C [7]. If too much heat is removed at once the salt could easily freeze.

This dissertation work is primarily focused on the reactor core, specifically the heat transfer within the pebble bed. Chapter 4 discusses the DRACS system in more detail, and the natural circulation implementation in particular.

1.2.2 Role of Scaled Experiments

To design and implement a small affordable experiment that is valid at full-scale is challenging. The design of multi-scale and multi-physics experiments is crucial to extracting the most valuable data for validation. Often it is not possible to build full size experiments that replicate the exact multi-physics dependencies, due to limitations in cost, space and other factors. However, it is possible to perform these experiments at a reduced geometric and temperature scale and with reduced heating and pumping power. This can be done by ensuring that the geometry, dynamics and kinematics between the experiment and the prototypical system are matched [8]. For most thermal-hydraulics experiments, one approach to choose the appropriate geometric and temperature scales are to ensure that the relevant non-dimensional numbers between the experiment and prototype are matched. It may also be possible to use simulant materials depending on the phenomena of concern. This is useful in cases where the reactor materials are expensive or hazardous. In the case of the PB-FHR, non-dimensional number matching shows that heat transfer oils can be used in experiments in place of fluoride salts (a high Prandtl number reactor coolant) [9]. This is advantageous because it allows experiments to be performed at smaller geometric scales and at lower temperatures than the prototypical system. In this manner, integral effects tests (IET) can be designed to simulate the PB-FHR. Further details are provided in Chapter 4 of the dissertation.

Therefore, the first step in designing scaled experiments for the purpose of code and model validation is to determine the dominant phenomena, and the dominant coupling of physics. For example, for two loosely coupled physics it might be sufficient to perform two scaled separate effects tests.

Separate effects tests

There are several reasons why SETs are a crucial part of FHR development:

- They serve to explore phenomenology that has not been previously investigated, at a smaller scale than integral effects tests
- They are used to develop a basis for code validation
- They are required to develop data for closure models for systems level codes
- They are necessary for component-scale testing

This dissertation is mainly focused on the first three points.

1.2.3 Introduction to heat transfer in pebble bed nuclear reactors

The purpose of this section is to elucidate key background concepts that are used throughout the dissertation. Typical reactor parameters that are used to make order of magnitude estimations are also provided. References are also provided for further details.

Key reactor parameters for order of magnitude estimations

The important parameters that are used in this chapter to estimate orders of magnitude are given in Table 1-1. It is important to note that the upper bound of the Reynolds number used is the theoretical maximum, as it assumes pure axial flow in the bed, when in reality there would be some cross-flow as well. Therefore a range of Reynolds numbers is given.

Table 1-1: Key reactor parameters for order of magnitude estimations

Parameter/Property	Symbol	Unit	Value	References
Fuel pebble diameter	D	m	0.03	[6]
Porosity	ε	Dimensionless	0.39	[10]
Fuel thermal conductivity	k_s	$Wm^{-1}K^{-1}$	15	[11]
Coolant thermal conductivity at 650°C	k_f	$Wm^{-1}K^{-1}$	1.091	[12]
Coolant density at 650°C	ρ	kgm^{-3}	1963	[12]
Coolant specific heat at 650°C	c_p	$Jkg^{-1}K^{-1}$	2416	[12]
Coolant dynamic viscosity at 650°C	μ	$kg(ms)^{-1}$	0.0068	[12]
Reactor thermal power	Q	MWth	236	[3]
Temperature difference across reactor (Coolant outlet – coolant inlet)	ΔT	K	100	[6]
Coolant mass flow rate	$m = \frac{Q}{c_p \Delta T}$	kgs^{-1}	977	[6]

Inner reflector radius	r	m	0.35	[6]
Outer radius of graphite pebble region	R	m	1.25	[6]
Cross-sectional area of axial flow (assuming core is empty for superficial velocity)	$A=\pi(R^2-r^2)$	m^2	4.52	[6]
Specific surface area in the core (surface area per volume)	a_v	m^{-1}	120	Section 1.3
Reynolds	Re	Dimensionless	500-952	Table 1-3
Prandtl	Pr	Dimensionless	12-18	Upper bound evaluated at 600°C. Lower bound at 700°C

Characteristics of fluoride salt coolant

Flibe is the salt coolant in the PB-FHR with a melting point of 459°C. It is composed of lithium fluoride (LiF) and beryllium fluoride (BeF_2). The properties of flibe are described by equations as a function of temperature [12] These equations are generally applicable to a given temperature range, so outside of that the properties must be extrapolated. Flinak is a beryllium-free fluoride salt composed of LiF, sodium fluoride (NaF) and potassium fluoride (KF). Its properties are also a function of temperature [12]. Flinak has lower Prandtl number than flibe, so to match the Prandtl number experiments with flinak must be performed at lower temperatures than for flibe, as shown in Chapter 2. It is possible to use flinak at lower temperatures to develop an experimental basis for heat transfer in fluoride salts. Additionally, the lack of beryllium in flinak means that SETs are more straightforward to design and conduct. The use of flinak in natural convection experiments is described in Chapter 2.

Characteristics of porous media

A pebble-bed reactor core is a porous medium. A porous medium can be thought of as composed of two parts – a solid phase and fluid phase. Pores refer to the space between the solid phase (for example, the fuel pebbles). The porous media described in this work is for a randomly packed pebble bed configuration. In this work the solid objects are spherical and each element is of equal size. Depending on the packing process the porosity can vary. The porosity, ε, is defined as the ratio between the volume of void space to the total volume.

The superficial velocity, U, is the fluid velocity in the container if it was empty. It is defined in Equation (1.1).

$$U = \frac{Q}{A} \tag{1.1}$$

In Equation (1.1), Q is the flowrate of the fluid and A is the cross-sectional area that the fluid flows through. In the PB-FHR this is the cross-sectional area of the annular reactor core, defined in Table 1-1. This assumes no radial flow in the core, which is an over simplification as there is 3D flow in the core. Therefore the superficial velocity estimated (and the resulting Reynolds number) with this method is the upper limit. The effective cross-section is dependent on the radial and axial flow conditions at that location. The superficial velocity is used when calculating the Reynolds number, defined in Table 1-2.

The permeability of a porous media, K (m^2), can be thought of as the ease with which fluid is allowed to pass through it. It is dependent on the geometry and dimensions of the pores as well as the porosity. The form coefficient C (m^{-1}) is a property of the porous media, and is a measure of the resistance that is exerted on a fluid flowing through it due to solid obstacles. For a given porous medium, K and C need to be known to provide closure to the momentum equation. Darcy's law is a model for momentum balance through a porous medium. It states that pressure drop varies linearly with flowrate in a cylinder filled with a porous medium. This is introduced in Section 1.3, and Darcy's model is expanded upon to include effects at higher flowrates (higher Reynolds numbers). Both K and C are independent of the fluid itself. These are defined in Section 1.2.3. In Chapter 3, K and C are experimentally determined for a pebble-bed test section.

Radiation heat transfer

Radiation is the process by which heat energy is transported through electromagnetic waves [13]. In the PB-FHR, radiation heat transfer between the fuel pebbles and the coolant may play a significant role. The coolant may act as a participating medium [9]

which means that the fluid may absorb infrared radiation. When doing scaled experiments with oil, radiation heat transfer is not included, and this could result in a distortion. However, the temperature difference between the average fuel pebble surface temperature and the surrounding flibe coolant temperature is small, and it is likely that the majority of the fission heat is transferred primarily through convection. The ratio of radiation to convection in the PB-FHR core during steady state normal operation can be estimated. The temperature difference used was at the location near the exit of the core [6]. This is shown in Chapter 3.

The estimation does not take into account that the salt coolant may act as a participating medium. Thermal radiation is likely to be small compared to convection. It is possible that the distortions regarding radiation heat transfer when using simulant fluids is not large assuming steady state normal operation conditions. This may not be true for accident transients, given the higher temperatures and larger temperature differences. Further study is merited to understand thermal radiation effects in salt systems and their potential scaling distortions in using oil data to characterize salt system convective heat transport.

Specific surface area in the core

For spherical particles, the specific surface area is given by Equation (1.2). a_v is the specific surface area (surface area per unit volume), ε the porosity and d the particle diameter in m, in this case the diameter of each fuel pebble. Reynolds number based on particle diameter is used because the predictive correlations for Nusselt number (a non-dimensional number which is the ratio of convective to conductive heat transfer in the fluid) use Reynolds number based on particle diameter [14].

$$a_v = \frac{6(1-\varepsilon)}{d} = \frac{6(1-0.39)}{0.03} = 120 m^{-1} \tag{1.2}$$

The diameter d refers to the diameter of the solid phase. Since the fuel pebbles in the Mk1 reactor are spherical, their diameter can directly be used. Each fuel pebble is 3 cm [3]. The porosity ε is for a random close packed configuration assuming the pebbles were poured into a container [10]. This is the closest case to the Mark-1 reactor core.

1.2.4 Dissertation research aims

The overall goal of the dissertation work is to better characterize heat transfer in pebble-bed nuclear reactor cores cooled by fluoride salts. An experimental approach has been

taken in this body of work, with supporting computational and analytical methods. The experimental approach is important for two reasons:

(1) Experiments provide direct data regarding the behavior of the PB-FHR, especially given the general dearth of data for this class of reactors. Elucidating basic heat transfer characteristics is valuable in developing the PB-FHR.
(2) Simulation codes can be validated against experimental data, which is an important step in ensuring a particular code is verified and validated (code V&V) before use in predicting reactor thermal hydraulic behavior.

Heat transfer needs to be accurately modeled in reactor systems and coupled-physics codes in order to predict temperature distributions within the reactor core. This is crucial since temperature distributions during power operation, transients and accidents need to be precisely predicted. This is necessary to draw conclusions about the integrity of the reactor and its surrounding structural material during such accident transients, and reactivity feedback due to fuel and coolant temperature. The results from multiphysics code simulations are used to assess reactor safety.

The main research objectives of this dissertation work can be summarized as follows:

- To improve the understanding of heat transfer in high Prandtl number coolants through separate effects tests. The coolant in the PB-FHR is defined by its Prandtl number of about 10-20. This is much higher than other nuclear reactor coolants, such as pressurized water (around 5), helium (around 0.7) or liquid metal (less than 0.01). Therefore it is crucial to characterize the basic heat transfer phenomenology in these fluoride salt coolants.
- To demonstrate how simulant oils can be used in place of the prototypical coolant provided where the relevant non-dimensional numbers are matched between experiment and prototypical system. A class of oils has been identified that match non-dimensional numbers of flibe at temperatures of around 100 °C, which is much lower than the salt operational temperatures which is from 600-700 °C. However, high quality experimental data is required to prove the similitude for a variety of conditions, such as natural convection. This is one of the aims of this dissertation work.
- To understand better the distortions that occur when using simulant oils versus fluoride salts. It is important to be able to qualify and quantify the distortions when oils are used, especially if the data is being used to validate PB-FHR simulation codes used for licensing.
- To develop an experimental facility to measure heat transfer coefficients from a pebble-bed test section, using frequency response techniques. The collected experimental data also serves to expand the literature in high Prandtl number

fluids and a range of Reynolds number flows (going from natural circulation to normal operation flowrates) as most of the currently reported data has been collected using air or water. This point will be elaborated in Chapter 3.

- To demonstrate flexible, simple and previously unused techniques that can be used to fabricate simple oil loops. This class of loops can be used in the future for further separate effects testing, especially to investigate coolant-structure boundaries in the PB-FHR.
- To show that frequency response techniques could be used to extract information about the thermal inertia and coupling between structural components and coolants. This becomes crucial in characterizing the transient thermal response of metallic structures in the PB-FHR.

1.3 Introduction to Porous Media Equations

The governing equations for porous media can be used to describe the mass, momentum and energy balances in the randomly packed pebble-bed reactor core. The equations presented below are in three dimensions with all terms included. Section 1.3.1 will prove that some terms can be neglected in the PB-FHR. However some general assumptions were still made when composing Equations (1.3) to (1.9). Additionally, these assumptions apply to the PB-FHR pebble-bed core.

- Porosity is constant with respect to time (examples where this is not the case involve swelling, such as when a porous sponge is submerged in water). Additionally, the porosity is not a function of position.
- Void spaces are interconnected
- The fluid in the void spaces is in single phase
- Volume averaged equations
- Saturated media, which means that the pores are completely filled
- Isotropic, implying that the properties of the porous media are not a function of the direction
- The solid phase (i.e. the pebbles) are stationary with respect to the fluid. In the PB-FHR the fuel pebbles are slightly buoyant in the coolant and are mobile. On average a particular fuel pebble takes about two months to travel from the core entrance to the exit. The coolant velocity in the pores during normal operation is 0.11 m/s, resulting in a residence time in the core of about 15 seconds. The residence time of a fuel pebble far exceeds that of the coolant, so the reactor core can be regarded as a fixed bed.

Mass conservation

$$\varepsilon \frac{\partial \rho_f}{\partial t} + \nabla \bullet (\rho_f \underline{v}) = 0 \tag{1.3}$$

In Equation (1.3), ε is the pebble-bed porosity, ρ_f the fluid density in kgm^{-3}, t time, and v velocity vector in ms^{-1}. Equation (1.3) states that the rate of change of fluid mass within a control volume is equal to the mass flux entering the control volume. This is the continuity equation.

Momentum

There are several ways to express momentum conservation in a porous medium. Darcy's law [15] is a simple expression related the pressure drop through the porous medium as a linear function of the fluid superficial velocity, fluid dynamic viscosity and the permeability. Darcy's law is only applicable to creeping flows, or flows with a Reynolds number (based on $K^{1/2}$) less than 10. For higher Reynolds number flows other effects must also be taken into account, such as the resistance due to turbulence. The HDD model [16] is shown in Equation (1.4).

$$\nabla P = -\frac{\mu}{K}\underline{v} - C\rho|\underline{v}|\underline{v} \tag{1.4}$$

For uni-directional flow, Equation (1.4) simplifies to Equation (1.5).

$$\nabla P = -\frac{\mu}{K}U - C\rho U^2 \tag{1.5}$$

In Equations (1.4) and (1.5), P is the pressure and v the velocity vector. The first term in the equation represents pressure drop due to viscous losses and the second term represents form losses that become significant when the Reynolds number is high or in the transition regime. Coolant flow could be in the transition regime during normal operation.

Energy

The energy conservation equations for the fluid and solid phases are detailed in Section 1.3.1.

1.3.1 Order of magnitude analysis of energy equations in the PB-FHR core

It is important to understand the relative magnitudes of the terms in the energy conservation equations. This will allow for simplification of the equations, which can provide insights for dominant phenomena and simplify modeling and simulation. Nield [17] postulated that viscous dissipation in the fluid phase would be non-negligible in pebble-bed nuclear reactors, due to the large flow rates within the core. It is useful to

compare the order of magnitudes of each term in the fluid energy equations to see if viscous dissipation needs to be included in subsequent analysis. The energy equations for each phase are given in Equations (1.6) and (1.7).

Fluid phase:

$$\varepsilon(\rho c_p)_f \frac{\partial T_f}{\partial t} + (\rho c_p)_f \underline{U} \bullet \nabla T_f = \varepsilon k_f \nabla \bullet \nabla T_f + \Phi + h_{sf} a(T_s - T_f) \quad (1.6)$$

Solid phase:

$$(1-\varepsilon)(\rho c_p)_s \frac{\partial T_s}{\partial t} = (1-\varepsilon)k_s \nabla \bullet \nabla T_s + (1-\varepsilon)q''' + h_{sf} a(T_f - T_s) \quad (1.7)$$

In Equations (1.6) and (1.7), ε is the pebble-bed porosity, ρc_p the volumetric heat capacity in Jm^3K^{-1}, T_f the coolant temperature in K, t time in s, U the coolant velocity in ms^{-1}, k_f the coolant thermal conductivity in $Wm^{-1}K^{-1}$, Φ the viscous dissipation term in Wm^{-3}, h_{sf} the interfacial convective heat transfer coefficient in $Wm^{-2}K^{-1}$, a the specific surface area (surface per unit volume) in m^{-1}, T_s the average fuel temperature in K, and q''' the heat generation in the fuel in Wm^{-3}. The subscript s refers to 'solid' or fuel and f refers to 'fluid' or coolant. Viscous dissipation is an irreversible process by which work done against viscous forces in the fluid is converted to internal energy in the fluid.

Since the Mk1 PB-FHR core is an annular cylindrical core, Equations (1.6) and (1.7) should be written in cylindrical coordinates. Equations (1.8) and (1.9) could be further simplified, but all the directional dependencies in the fluid direction are important. Cross-flow is used in the PB-FHR core, along with axial flow, to enhance the uniformity of heat removal and reduce overall core pressure drop. Power generation also varies radially and axially, and combined this means that the fluid temperature will also be dependent on the radial direction. The azimuthal temperature variation may also be significant because the bed itself is not perfectly axisymmetric. The fuel pebbles are randomly packed in the core, and it is also possible that the heat generation within the core is not axisymmetric. This may be due to non-axisymmetric control rod insertion or withdrawal, or due to pebbles remaining longer in certain locations. Therefore it is unlikely that the fluid temperature will be perfectly axisymmetric. Clearly the fluid temperature varies with the axial position given that there is heat generation within the core and that the fluid enters from the bottom and exits at the top of the core. It may be possible to neglect the azimuthal terms in the solid and fluid equations for ease of computations, but the results may only apply in a limited number of cases. The energy balance equations for the fluid and solid phases in terms of cylindrical co-ordinates are given in Equations (1.8) and (1.9).

Fluid phase:

$$\varepsilon(\rho c_p)_f \frac{\partial T_f}{\partial t} + \varepsilon(\rho c_p)_f \left[u_r \frac{\partial T_f}{\partial r} + \frac{u_\theta}{r} \frac{\partial T_f}{\partial \theta} + u_z \frac{\partial T_f}{\partial z} \right]$$
$$= \varepsilon k_f \left[\frac{1}{r} \frac{\partial}{\partial r} \left(r \frac{\partial T_f}{\partial r} \right) + \frac{1}{r^2} \frac{\partial^2 T_f}{\partial \theta^2} + \frac{\partial^2 T_f}{\partial z^2} \right] + \Phi + h_{sf} a (T_s - T_f) \quad (1.8)$$

Solid phase:

$$(1-\varepsilon)(\rho c_p)_s \frac{\partial T_s}{\partial t}$$
$$= (1-\varepsilon) k_s \left(\frac{1}{r} \frac{\partial}{\partial r} \left(r \frac{\partial T_s}{\partial r} \right) + \frac{1}{r^2} \frac{\partial^2 T_s}{\partial \theta^2} + \frac{\partial^2 T_s}{\partial z^2} \right) + (1-\varepsilon) q''' + h_{sf} a (T_f - T_s) \quad (1.9)$$

In Equations (1.8) and (1.9), r is the radial coordinate, θ azimuthal and z axial.

Assumptions

Several assumptions have been applied Equations (1.8) and (1.9). It should be noted that the fuel temperatures are an average temperature. In the prototypical reactor each spherical fuel element is made up of layers of different materials, one of which is composed of fuel particles. Thus the temperature in each layer will be different. This should be captured in Equations (1.8) and (1.9) as they include radial dependence of temperature. Furthermore the solid phase is assumed to be stationary. This is a valid assumption given that the fuel residence time in the core is about two months and the slowest axial fluid phase velocity is on the order of 0.002 m/s (which is during natural circulation). The fuel thermal conductivity is assumed to be constant with respect to space, simplifying calculations. The fuel is primarily composed of graphite, whose properties may not be well characterized especially when it has been irradiated. For the purposes of this order of magnitude analysis the graphite properties (specifically the thermal conductivity) were assumed to be the same as the TRISO fuel pebbled from high-temperature helium-cooled reactors [11] [18].

The permeability K is defined by Darcy's equation for flow in porous media. However, Darcy's relationship is not applicable in the PB-FHR reactor core as it was developed for Darcy flows which typically have Reynolds numbers based on $K^{1/2}$ of less than 10 [16]. It can be estimated using Carmen-Kozeny's relationship for a bed of packed spheres. Carman-Kozeny is an analytical relationship based on spherical particles [16], which is the case in the PB-FHR given the fuel element shape. The permeability for a pebble-bed should be determined experimentally, but since this is first-order analysis such levels of precision are not necessary. The drag coefficient C can also be estimated as shown in Equation (1.11) [16].

$$K = \frac{D^2 \varepsilon^3}{180(1-\varepsilon)^2} = \frac{0.03^2 \times 0.39^3}{180(0.61)^2} = 8 \times 10^{-7} m^2 \quad (1.10)$$

$$C = \frac{1.75*(1-\varepsilon)}{D\varepsilon^3} = \frac{1.75*(1-0.39)}{0.03*0.39^3} = 600 m^{-1} \quad (1.11)$$

The flow in the Mk1 PB-FHR core is non-Darcian, and this can be seen from the Reynolds number based on the permeability *K* as shown in Equation (1.12). Therefore the Hazen-Dupuit-Darcy (HDD) model is used to find the pressure drop in the porous medium. The properties of flibe are taken at 650 °C given that the inlet salt temperature is 600°C and the outlet 700°C.

$$\mathrm{Re}_K = \frac{\rho U K^{1/2}}{\mu} = \frac{1963 \times 0.11 \times (8 \times 10^{-7})^{1/2}}{0.0068} = 30 \quad (1.12)$$

In Equation (1.12), ρ is the flibe density, *U* the superficial velocity, *K* the permeability and μ the dynamic viscosity.

The importance of the viscous dissipation term can be checked by comparing the order of magnitude of different terms in the fluid energy balance equation and the viscous dissipation term. This term is checked for forced circulation (which is during normal power operation) and natural circulation (which occurs during an accident scenario).

The viscous dissipation term is given in Equation (1.13) [16].

$$\Phi = \frac{\mu}{K} U^2 + C \rho U^3 \quad (1.13)$$

The variables have been previously defined.

Table 1-2 gives the order of magnitudes for the different terms in the fluid phase equation (1.8). The properties were taken at 650°C because that is the average between the inlet and outlet fluid temperatures in the PB-FHR.

The length scale L is taken to be the height of the PB-FHR core. In forced circulation, the velocity used for the order of magnitude analysis is the superficial velocity in the core, as estimated in Equations (1.14) and (1.15).

$$m = \frac{Q}{c_p \Delta T} = \frac{236000000}{2416 \times 100} = 977 kgs^{-1} \quad (1.14)$$

$$U = \frac{m}{\rho A} = \frac{977}{1963 \times 4.52} = 0.11 ms^{-1} \quad (1.15)$$

Table 1-2: Magnitudes of terms in the governing energy equation during forced convection

Viscous dissipation	$\frac{\mu}{K}U^2 + C\rho U^3 = \frac{0.0068}{8\times10^{-7}}0.11^2 + (600*1963*0.11^3)$	Wm^{-3}	1.6×10^3
Diffusion term	$\frac{k\Delta T}{L^2} = \frac{1.091*100}{4.58^2}$	Wm^{-3}	5
Advection term	$(\rho c_p)_f U\frac{\Delta T}{L} = 1963*2416*0.11\frac{100}{4.58}$	Wm^{-3}	1.1×10^7

Table 1-3: Non-dimensional numbers in the core during normal operation (forced convection)

Peclet number (Pe)	$\frac{UD}{\alpha} = \frac{0.11*0.03}{1.091/(1963*2416)}$	1.4×10^4
Reynolds number (Re)	$\frac{\rho UD}{\mu} = \frac{1963*0.11*0.03}{0.0068}$	952
Prandtl number (Pr)	$\frac{\mu c_p}{k_f} = \frac{0.0068*2416}{1.091}$	15

It can be seen that the viscous dissipation term is much larger in magnitude compared to the diffusion term. It is much smaller in magnitude compared to the advection term and therefore can probably be neglected when modeling heat transfer in the PB-FHR. It is important to note that the diffusion term in Table 1-2 only considers pure thermal diffusion and no thermal dispersion, which is likely to be significant in pebble-bed reactors. This is further discussed below.

In natural circulation, the superficial velocity is 0.0022 m/s. The reactor power used to calculate this was 2% of the total power.

$$m = \frac{Q}{c_p \Delta T} = \frac{236000000\times0.02}{2416\times100} = 19.54 kgs^{-1} \quad (1.16)$$

$$U = \frac{m}{\rho A} = \frac{19.54}{1963\times4.52} = 0.0022 ms^{-1} \quad (1.17)$$

A single DRACS system is sized to remove 1% of the full reactor power. During emergency shut down a minimum of two DRACS systems would be operational. To estimate the coolant velocity during natural circulation, 2% of the total reactor power was used.

Table 1-4: Magnitudes of the terms in the governing energy equation during natural circulation

Viscous dissipation	$\frac{\mu}{K}U^2 + C\rho U^3 = \frac{0.0068}{8\times10^{-7}}0.0022^2 + (600*1963*0.0022^3)$	Wm^{-3}	20
Diffusion term	$\frac{k\Delta T}{L^2} = \frac{1.091*100}{4.58^2}$	Wm^{-3}	5
Advection term	$(\rho c_p)_f U\frac{\Delta T}{L} = 1963*2416*0.0022\frac{100}{4.58}$	Wm^{-3}	1×10^6

Table 1-5: Non-dimensional numbers in the core during emergency shutdown (natural circulation)

Peclet number (Pe)	$\frac{UD}{\alpha} = \frac{0.0022*0.03}{1.091/(1963*2416)}$	1.3×10^3
Reynolds number (Re)	$\frac{\rho UD}{\mu} = \frac{1963*0.0022*0.03}{0.0068}$	19
Prandtl number (Pr)	$\frac{\mu c_p}{k_f} = \frac{0.0068*2416}{1.091}$	15

Clearly, viscous dissipation can be neglected during natural circulation operation.

The thermal boundary conditions of the reactor include a fixed inlet and outlet temperature, which are the same during normal operation and emergency heat removal.

Thermal dispersion is also an important phenomenon that should be included [19]. It refers to heat transferred through local mixing due to fluid flow around the multitude of obstacles (the fuel pebbles). It can be treated similarly to thermal conduction. During normal operation the Peclet number in the core is large, which means that thermal energy is transported more by advection than diffusion, as expected for a fluoride salt coolant. The effect of dispersion is to enhance heat transfer in the porous media, so ignoring it will yield localized temperatures within the core that are larger than in reality. Thermal dispersion effects are greater in areas where the fluid velocity in the pores is high (so, away from the walls of the reactor core). The dispersion effect can be included within the fluid thermal conductivity term. As a side note, the large Peclet number in the reactor core implies that thermal diffusion can be neglected, but that thermal dispersion may be important. This is because a larger fluid velocity is likely to result in more fluid mixing due to vortices around the solid obstacles. In the PB-FHR core lateral thermal diffusion may also be non-negligible given that radial flow will be significant. However, the thermal dispersion will likely overshadow it.

It is possible that thermal dispersion and viscous dissipation energy cancel each other out in the PB-FHR core during normal operation. The order of magnitude of the thermal dispersion term is estimated. The correlations for axial and transverse dispersion coefficients were evaluated. The axial term far exceeds the transverse term as is usually the case in a randomly packed, isotropic pebble-bed [15]. The magnitudes are shown in Table 1-6.

Table 1-6: Correlations for thermal dispersion

Reference	**Correlation**	**Evaluation (W/m K)**	**Additional comments**
Elsari and Hughes [20]	$\frac{k_{eax}}{k_f} = 7.24 + 8.49\,\mathrm{Re}$	8800	Axial thermal dispersion. Experimentally derived.
Alazmi and Vafai [21]	$k_{eax} = \left(\varepsilon + 0.5\,\mathrm{Pr}\,\mathrm{Re}\right)k_f$	7800	Axial thermal dispersion
Hsu and Cheng [22]	$k = D'\frac{1-\varepsilon}{\varepsilon}k_f Pe \;\; (D' = 0.04)$	90	Radial thermal dispersion. Derived from volume averaging methods of velocity and temperature. For $Re > 10$ (high Reynolds number flows, based on particle diameter)
Wakao and Kaguei [23] [24]	$k_e = k_f + \gamma k_f Pe \; (\gamma = 0.1)$	1500	Effective thermal dispersion (includes axial and transverse dispersion).

The fuel thermal conductivity k_s was taken to be 15 W/m K [11]. These values for the thermal dispersion coefficient imply that the magnitude of the thermal conduction in the fluoride-salt-cooled pebble bed core is about 7000 to 8000 times larger than if thermal dispersion were not included. The axial thermal dispersion was used for the scale analysis as it is larger than the transverse component. This will overshadow the viscous dissipation term, and thus viscous dissipation during normal operation may still be

ignored. Table 1-7 shows the order of magnitudes of each term in the fluid equation taking into account thermal dispersion during normal operation and natural circulation. However the conduction term is still much smaller than the advection term during normal operation and natural circulation.

Table 1-7: Magnitudes of thermal diffusion terms including and excluding thermal dispersion for forced convection and natural circulation, units in Wm^{-3}

	Forced Convection	Natural Convection
Order of magnitude of diffusion only	5	5
Order of magnitude of diffusion and dispersion	3×10^4	3×10^4

Nield [17] suggested that viscous dissipation may be non-negligible in pebble-bed nuclear reactors. He did not include the form loss term in his expression for viscous dissipation, opting to use the Darcian expression. However in this order of magnitude analysis the form loss term was included as shown in Equation (1.13). The form loss term is much larger in magnitude compared to the viscous losses and therefore should not be neglected (this is because of the large velocities in the core during normal operation). Nonetheless the viscous dissipation term can be neglected in the PB-FHR during forced convection and natural circulation given that the advection term is substantially larger. Flibe is excellent at transporting heat advectively, so this makes sense intuitively despite the large velocities and small particle size. The thermal dispersion term will serve to counter these heat additions as it is about 10 times larger than the viscous dissipation term. Another way to think about this is to compare total circulating power to the thermal power. The circulating power is the product of the pressure drop and the volumetric flow rate. The higher the volumetric flow rate the larger the corresponding viscous dissipation term. For the PB-FHR the circulating power is much smaller compared to the thermal power, and thus viscous dissipation may be neglected.

The magnitude of viscous dissipation in helium-cooled pebble-bed nuclear reactors can also be estimated as shown in Table 1-8. The properties of helium were evaluated at 700 °C and 9 MPa, which are the operating conditions of the Pebble-Bed Modular Reactor (PBMR) [25]. The permeability K and the form coefficient C differ from the PB-FHR core because the fuel diameter is different. The porosity was assumed to be the same. It is immediately noticeable that the dispersion term is large, and is of the same order of magnitude as the viscous dissipation term. Both terms are about 10 times smaller than the advection term. Including viscous dissipation is important for the PB-FHR case as well as the gas-cooled reactor case. The values for the core dimensions and reactor

parameters (such as the temperatures and the velocities) used in Table 1-8 were found in [26] and [27]. When modeling gas-cooled pebble-bed reactors, none of the terms can be neglected in the governing equation for energy. In gas-cooled reactors, the volumetric flow rate of the coolant is high, which means that the circulating power cannot be ignored, and thus neither can viscous dissipation.

Table 1-8: Order of magnitude of terms in the porous media governing equation for energy for the PBMR

Viscous dissipation	$\frac{\mu}{K}U^2 + C\rho U^3 = \frac{4.5\times10^{-5}}{8.2\times10^{-6}}5.74^2 + (300*4.4*5.74^3)$	Wm^{-3}	2.5×10^5
Diffusion + dispersion term	$\frac{k\Delta T}{L^2} = \frac{5\times10^4*400}{11^2}$	Wm^{-3}	1.7×10^5
Advection term	$(\rho c_p)_f U \frac{\Delta T}{L} = 4.4*5195*5.74\frac{400}{11}$	Wm^{-3}	4.8×10^6

Table 1-9: Non-dimensional numbers in the PBMR core during normal operation, used to evaluate thermal dispersion

Peclet number (Pe)	$\frac{UD}{\alpha} = \frac{5.74*0.06}{0.36/(4.4*5195)}$	2.2×10^4
Reynolds number (Re)	$\frac{\rho UD}{\mu} = \frac{4.4*5.74*0.06}{4.5\times10^{-5}}$	3.4×10^4
Prandtl number (Pr)	$\frac{\mu c_p}{k_f} = \frac{4.5\times10^{-5}*5195}{0.36}$	0.65

In general the viscous dissipation term will become non-negligible if the viscosity of the coolant is large and the permeability in the pebble-bed is small. Additionally if the reactor design is such that the temperature difference between the inlet and outlet of the reactor core is small and the length of the reactor core is large, the advection term becomes less significant. If the superficial velocity is large, it increases the viscous dissipation term given the cubed velocity term. The viscous dissipation term is more significant in that case. Furthermore small particle diameters and large packing fractions will also serve to increase viscous dissipation in the core given the large number of obstacles to the fluid flow. Higher circulating power is necessary in these cases.

1.4 Structure of the Dissertation

This dissertation is split into five chapters. This chapter provides the required background in order to be able to place the work done in a broader context. Chapter 2

concentrates on experiments designed to prove similitude between the prototypical coolant (the fluoride salt) and the simulant fluid (heat transfer oils). When sufficient proof exists that simulant oils are equivalent to fluoride salts in the non-dimensional space (accounting for distortions), then data from experiments using oils can be used to draw conclusions about the thermal hydraulic behavior of molten salt systems, and this data could eventually be used for code validation. Chapter 3 focuses on separate effects tests done to measure heat transfer coefficients for the range of non-dimensional numbers applicable to the PB-FHR. Chapter 4 shows that thermal-hydraulics systems codes such as Flownex can be used to simulate the PB-FHR and that the results can be validated using data from integral effects tests. It stresses the importance of accurate closure models in multiphysics simulation codes. This chapter will concentrate on the passive safety system in the PB-FHR that removes the decay heat from the core during emergency shutdown. Chapter 5 completes the dissertation by summarizing the work done and detailing salient conclusions.

This dissertation is structured in such a way that every chapter can be read as a standalone piece of work. However the work done in Chapter 2 was critical in informing the experimental methodology in Chapter 3. Chapter 4 demonstrates how the conclusions from Chapter 3 will influence the multiphysics simulations of the PB-FHR. In this way, a meticulous reader may gain a thorough understanding of this body of work while an impatient one can skip straight to the chapter of interest and forego comprehensive enlightenment on the entire subject.

2. SEPARATE EFFECTS TESTS IN SUPPORT OF UNDERSTANDING HEAT TRANSFER WITHIN PEBBLE BED NUCLEAR REACTORS

While many experiments have been conducted to characterize heat transfer in salts, only a few have studied fluoride salts in particular. Ambrosek [28] performed a review of heat transfer studies that have been conducted using flinak. There have been several studies investigating forced convection in a pipe. Additionally Yoder [29] summarized flinak heat transfer experiments that have been reported so far. It should be noted that natural convection heat transfer in flinak has not been extensively studied. Therefore in order to advance the current understanding of FHR technology, natural convection heat transfer from an isolated sphere and from a heated cylindrical rod were carried out in this dissertation work using flinak.

As of yet, very few heat transfer experiments have been carried out that specifically show similitude between oils and fluoride salts, and none have been published to the knowledge of the author. It is important to be able to design an experiment to demonstrate similitude and to establish the best method in doing so, so that other potential simulant fluids can also be shown to match with the fluoride salts. In this chapter, similitude was investigated for natural convection heat transfer cases. Natural convection is the process by which heat is transferred within a fluid due to density differences in the fluid causing fluid motion. The fluid motion is not caused by an external force (such as a pump), but by buoyancy forces.

Simulant fluids are synthetic organic oils such as Dowtherm A or Drakesol 260AT. For natural convection flows, it is important to match Grashof and Prandtl numbers (defined in Section 2.1.1 and 2.2.1) between the simulant oil and the fluoride salt. Two different geometries were investigated – natural convection heat transfer from an isolated sphere and from a heated cylinder. Because the Prantl number of liquids increases with decreasing temperature, similitude can be achieved by selecting the correct temperature range for the simulant fluid. For example, the Prandtl number of flibe (Li2BeF4) at 650° can be matched by Dowtherm A at 90°C, and by the molten salt flinak (46.5% LiF- 11.5% NaF- 42% KF) at 550°C. By ensuring a match in the non-dimensional numbers, the geometry and the temperature of the scaled experiment are designed. In the following experiments, a range of non-dimensional numbers were investigated, explained in more detail in Section 2.1.1 and Section 2.2.3.

When performing separate effects tests (SET) for verifying similitude, it is important to understand any distortions that occur between the scaled and prototypical systems. This

serves to further inform how both integral and separate effects scaled experiments should be designed going forward. Additionally, previously unaccounted phenomenology in the prototypical system can be understood and included. This is one of the secondary goals as outlined in the two experiments shown in Section 2.1 and 2.2.

2.1 Heat Transfer from an Isolated Sphere [30]

The aim of this investigation was to experimentally measure the Nusselt number for natural convection heat transfer from a brass sphere immersed in a flinak salt bath, as a function of the Grashof and Prandtl numbers, and compare the data to predictions made using standard correlations for natural convection from a sphere. The predicted Nu was also compared to values calculated using the computational fluid dynamics code COMSOL.

The prediction of the performance of passive decay heat removal systems (the DRACS in the case of the PB-FHR design) depends ultimately on component-scale phenomena. These are studied using experimental and computational models. COMSOL was used to understand transient natural convection flow of high Prandtl number fluids – such as fluoride salts and Dowtherm A oil – around a hot sphere, and thus predict Nusselt number in a transient regime. Separate effects tests were done to characterize the phenomenology, using computational models to elucidate distortions. Transient natural convection from a single sphere is a simple case that is presented here, but this approach can eventually be extended to a packed bed of spheres, which is the fuel configuration in PB-FHR [7]. This is further detailed in Chapter 3 of the dissertation.

It is important to compare the Biot (Bi) number of the brass pebble with the actual graphite fuel pebbles that the brass pebble experiment simulates. If Bi is small, generally less than 0.1, for both the brass and graphite pebble, then we can assume an essentially uniform temperature within both [13]. The baseline graphite fuel pebbles for PB-FHRs are 3 cm in diameter, larger than the brass spheres used in the current investigation. Bi is defined in Equation (2.1).

$$Bi = \frac{hL_c}{k} \tag{2.1}$$

Where h is the convective heat transfer coefficient, L_c the characteristic length of the pebble and k the thermal conductivity of the pebble. The characteristic length for conduction in a sphere is usually taken as the ratio between the volume and the surface area of the sphere, which is $D/6$, where D is the sphere diameter.

Table 2-1 gives bounding values for Bi for brass and graphite spheres. The value for h was chosen based on the highest value seen in the experimental data. Bi for the brass

pebble is smaller than for graphite, but the graphite value is still smaller than 0.1. Therefore, the uniform temperature approximation within the brass sphere and the fuel pebble is justified.

Table 2-1: Typical Biot numbers for brass and graphite

Material	***h* (W/m²K)**	**D (m)**	***k* (W/mK)**	**Bi**
Brass	900	0.0127	147 @ 673 K [31]	0.0130
Graphite	900	0.03	81.4 @ 673 K [32]	0.0553
Graphite	900	0.0127	81.4 @ 673 K [32]	0.0234

Additionally, in the FHR the convection heat transfer is from the fuel pebble bed to the coolant, flibe. The current investigation only looks at heat transfer to a single sphere. This is a useful first step to confirm whether existing correlations can predict the heat transfer coefficient of fluoride salt coolants and under what transient conditions the correlations may or may not be accurate.

Furthermore, the coolant in the PB-FHR is flibe. The current investigation uses another fluoride salt, flinak (46.5% LiF- 11.5% NaF- 42% KF) (Figure 2-2 and Figure 2-3) in order to avoid experimental complications associated with beryllium toxicity. The Prandtl number of flinak is matched with flibe at a lower temperature range than the FHR operating temperatures, as shown in Figure 2-2. It is equally important to characterize heat transfer at lower temperatures (temperatures closer to the freezing point of flibe), because some accidents could result in overcooling transients, potentially freezing part of the coolant.

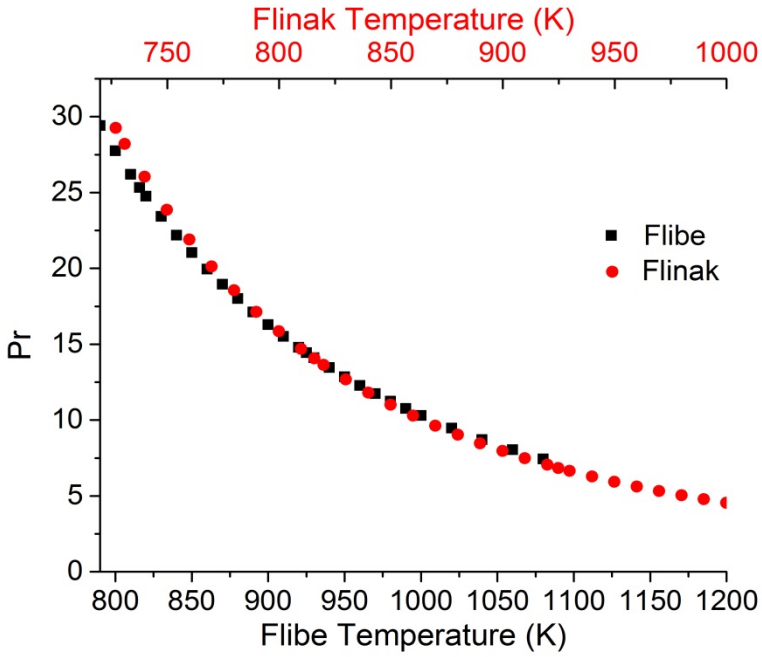

Figure 2-1: Prandtl number scaling between flinak and flibe

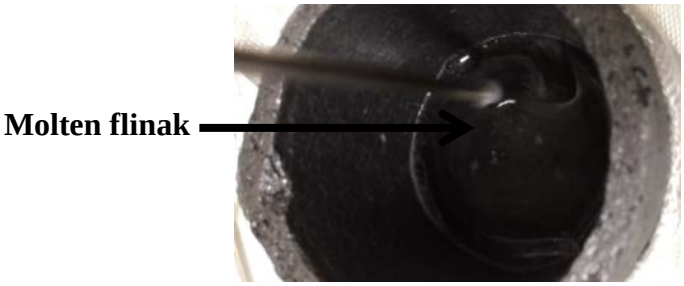

Figure 2-2: Molten flinak is transparent, as is flibe

The Prandtl (Pr) number in the experiments ranged from 10 to 30 and the Grashof (Gr) number ranged from 1500 to 350,000. The Pr and Gr are defined as

$$\mathrm{Pr} = \frac{\mu c_p}{k} \tag{2.2}$$

$$Gr = \frac{\rho^2 g \beta (T_p - T_b) D^3}{\mu^2} \tag{2.3}$$

where μ is the dynamic viscosity of the fluid, c_p the specific heat capacity, k the thermal conductivity, ρ the density, g the acceleration due to gravity, β the thermal coefficient of expansion, T_p the pebble temperature and T_b the bath temperature and D the diameter of the pebble. The thermophysical property correlations that were used to calculate Pr and Gr were taken from a report from Idaho National Laboratory (INL) [12] and the specific correlations used to estimate Pr and Gr are detailed in Section 2.1.4.

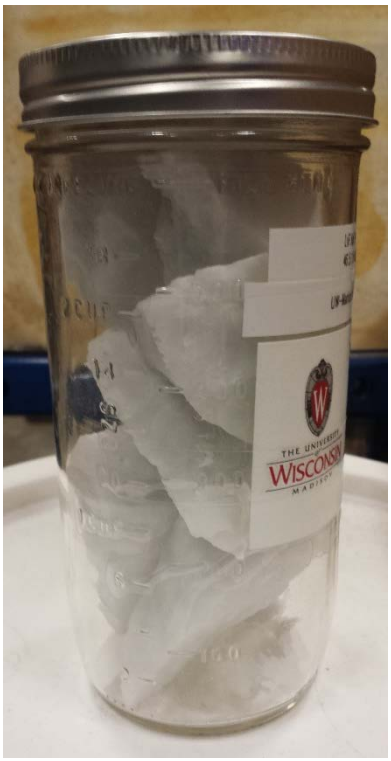

Figure 2-3: Flinak salt at room temperature, stored under inert nitrogen gas. Made at the University of Wisconsin, Madison

2.1.1 Experimental Procedure

A brass sphere, referred to as the 'pebble', was instrumented with a 0.508 mm diameter Type K sheathed thermocouple embedded in a hole drilled to the center of the pebble. Given the size of the pebbles used, it was not feasible to instrument them with additional thermocouples to experimentally verify the small Bi number assumption. Two spheres with different diameters were used, as outlined in Table 2-2. This pebble was immersed in a bath of flinak held in a stainless steel crucible wrapped with flexible ceramic insulation. The salt was supplied by the University of Wisconsin, Madison in a purified and dried state. Flinak melts at 454 °C. The experiments melted the flinak inside its crucible using either a heating blanket or a box furnace. The salt was melted in air in a period of ten minutes. A 0.508 mm Type K thermocouple was used to monitor the temperature of the flinak bath throughout the experimental run, until equilibrium

between the pebble and the bath was reached. The thermocouple monitoring the bath temperature was fixed with a clamp between the pebble and the inner wall at half the depth of the crucible (crucible dimensions are listed in Table 2-2). Due to the large thermal inertia of the salt and its container, T_b remained nearly constant while T_p reached equilibrium. The experimental set up is shown in Figure 2-4.

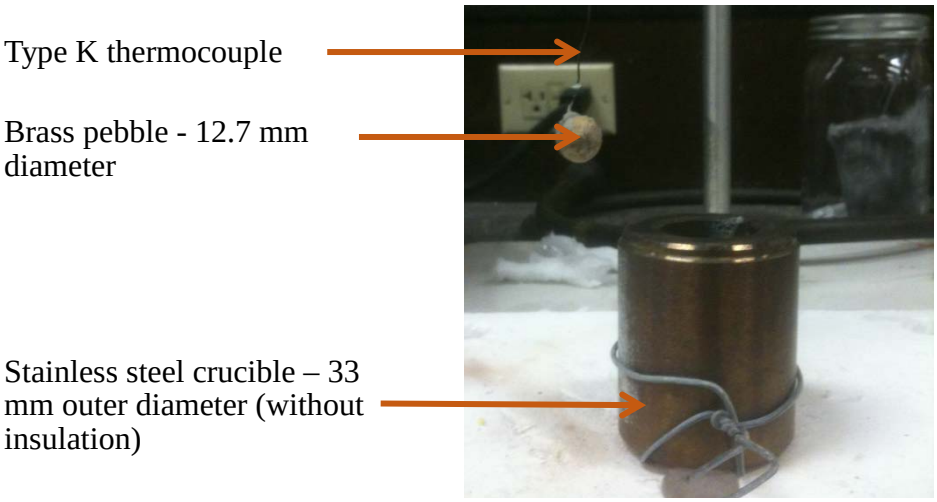

Figure 2-4: Experimental set up to measure heat transfer of a brass sphere immersed in a flinak salt bath

2.1.2 Experimental Apparatus

Five experimental runs are reported here. Table 2-2 shows the range of Pr and Gr that were investigated, as well as the apparatus that was used. A wide Gr range was studied by using various pebble diameters. The film temperature, which is the average between the pebble and bath temperatures, was used to calculate the Prandtl and Grashof numbers.

Table 2-2: Experimental range and parameters for 5 runs

Run No.	Pebble diameter (m)	Pebble mass (kg)	Initial pebble temperature T_p (°C)	Bath temperature T_b (°C)	Crucible material	Crucible inner diameter/ depth (m)	Prandtl range	Grashof range
1	0.021	0.0307	447	462	Ceramic	0.043/0.058	27-29	1500-19000
2	0.021	0.0307	543	514	Ceramic	0.043/0.058	16-22	17600-80000
3	0.0127	0.0091	683	541	Ceramic	0.043/0.058	10-11	331000-384000
4	0.0127	0.0091	360	539	Stainless steel	0.0254/0.0446	17-28	15000-39000
5	0.0127	0.0091	365	544	Stainless steel	0.0254/0.0446	15-28	15000-40000

It was assumed that the temperature variation within the pebble itself could be neglected, because pre-predictions showed that the Biot number was much smaller than 0.1. This was also confirmed after the experimental values of h were determined. Figure 2-5 shows that the temperature variance within the 0.0127-m diameter pebble is less than 1%. At 5 seconds the heat transfer coefficient h is larger than it would be at a later time, so Bi calculated with this would also be larger, thus showing that the Biot number is always much smaller than 0.1. It is more realistic to use the experimental value for h in Equation (2.1), given the large discrepancy between the prediction and the experimental values.

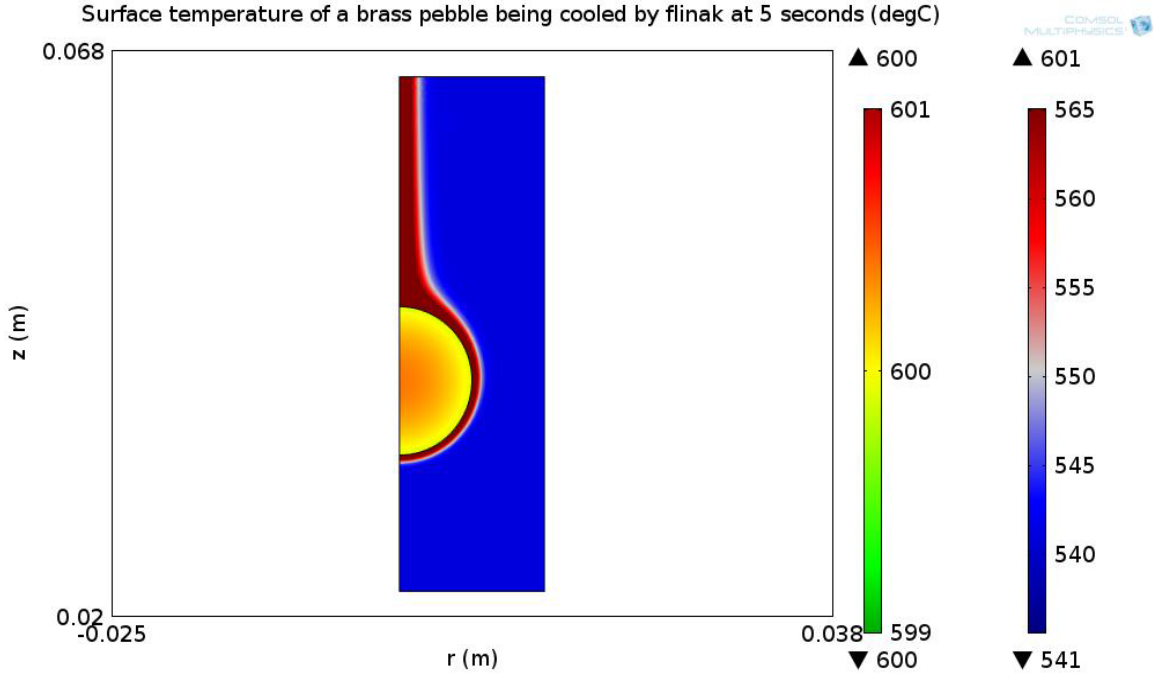

Figure 2-5: Temperature distribution of the bath and the pebble at 5 seconds as predicted by COMSOL

2.1.3 Data Reduction Procedure

Thermocouple readings from the brass pebble and the flinak salt were recorded using a National Instruments SCXI-1600 data acquisition system, held by a NI SCXI-1000 chassis. The natural convection heat transfer coefficient between the pebble and the bath, h, was calculated using Equation (2.5).

$$\frac{mc_p}{A}\frac{dT_p}{dt} = h(T_p - T_b) + \varepsilon\sigma(T_p^4 - T_b^4) \tag{2.4}$$

$$\Rightarrow h = \frac{\left(\frac{mc_p}{A}\right)_p \frac{dT_p}{dt} - \varepsilon\sigma(T_p^4 - T_b^4)}{(T_p - T_b)} \tag{2.5}$$

where m is the mass of the pebble, c_p the specific heat capacity of the brass pebble, A the surface area of the pebble, dT_p/dt the derivative of the pebble temperature with respect to time, T_p the pebble temperature, T_b the salt bath temperature, ε the emissivity of the brass and σ the Stephan-Boltzmann constant.

It should be noted that as equilibrium between the bath and pebble is approached, the error associated with the experimentally measured h goes to infinity because the difference between T_p and T_b is small. The experimental data when the pebble temperature reaches within 1°C of bath temperature was not used for the purposes of data reduction.

The radiation heat transfer correction to h is necessary because thermal radiation is not negligible at the temperatures of the experiments. The infrared absorption characteristics of flinak are not well known [9]. In this analysis it is assumed that the flinak acts as a non-participating medium. The view factor from the sphere to the salt bath is 1. The emissivity of the brass surface was estimated to be 0.15. The radiation heat transfer is relatively small compared to convection early on, and while its relative contribution increases with time, it remains relatively small. The radiation heat transfer is larger when the temperature difference between the pebble and the bath is large, and becomes less as the pebble temperature approaches the bath temperature.

The derivative of the pebble temperature dT_p/dt was calculated numerically using OriginPro 9 [33], using Equation (2.6).

$$\frac{dT}{dt} = \frac{1}{2}\left(\frac{T_{i+1} - T_i}{t_{i+1} - t_i} + \frac{T_i - T_{i-1}}{t_i - t_{i-1}}\right) \tag{2.6}$$

The temperatures T_p and T_b were both smoothed using a FFT filter with a 20 point window. This ensured that noise from the thermocouple readings was smoothed over. The ratio mc_p/A is a constant fixed by the pebble used for the experimental run.

2.1.4 Experimental Results and Comparisons to Predictions

The Nusselt number for natural convection for single spheres was predicted using Churchill's correlation [34] as shown in Equation (2.7).

$$Nu = 2 + \frac{0.589(\mathrm{Pr}\,Gr)^{1/4}}{\left[1+\left(\frac{0.469}{\mathrm{Pr}}\right)^{9/16}\right]^{4/9}} \tag{2.7}$$

Material properties for Pr and Gr were calculated using the film temperature, which is the mean of the temperatures of the pebble and the bath as shown in Equation (2.8).

$$T_f = \frac{T_p + T_b}{2} \tag{2.8}$$

The film temperature is used to evaluate material properties because it reflects the average temperature within the boundary layer, from the surface of the pebble to the edge of the boundary layer, where the temperature is T_b. It is the temperature used to evaluate the predicted Nu shown in equation (2.7) [13]. It is important to note that the material properties for flinak are not fully characterized for all temperatures. Density, viscosity and thermal conductivity had to be extrapolated at the temperatures close to the freezing point of flinak. These are detailed in Equations (2.9) through (2.12) [12]. Gr and Pr were calculated using the measured values of T_p and T_b, and these were used to predict Nu as a film temperature changed with time, using Equation (2.7). Equation (2.5) was used to derive the experimental Nu.

$$\rho = 2729.3 - 0.73T \quad (667\ ^\circ\mathrm{C} < \mathrm{T} < 897\ ^\circ\mathrm{C}) \tag{2.9}$$

$$\mu = (2.487\times10^{-5})e^{4478.62/T} \quad (497\ ^\circ\mathrm{C} < \mathrm{T} < 697\ ^\circ\mathrm{C}) \tag{2.10}$$

$$k = 0.36 + (5.6\times10^{-4})T \quad (517\ ^\circ\mathrm{C} < \mathrm{T} < 807\ ^\circ\mathrm{C}) \tag{2.11}$$

$$c_p = 1905.57 \quad (\text{for all T}) \tag{2.12}$$

where ρ is the density of flinak in kg/m^3, μ the dynamic viscosity of flinak in kg/m s, k the thermal conductivity of flinak in W/m K, c_p the specific heat of flinak in J/kg K, and T the temperature of flinak in Kelvin.

Some of the pebble heating runs started with the pebble and the film temperature below the freezing temperature of flinak. Because the properties correlations would not be accurate in this temperature range, those values were not used in the data reduction. Only data with a film temperature above 454 °C was used.

It can be seen from Figure 2-6 that there is a large discrepancy between the Churchill correlation values of Nu and the experimentally measured Nu. The experimentally measured Nu numbers are at least 3 times lower than the correlation. This is the case for both heating up and cooling down the pebble. One other point to note is that the Churchill correlation used to predict Nusselt number (Equation (2.7)) assumes steady state natural convection from a sphere immersed in a bath. It is possible that the quasi-steady state approximation is not appropriate. This is discussed in more detail in Section 2.1.5. RUN 3 shows slightly negative Nusselt numbers, which is due to fluctuating values of dT_p/dt. These arise from fluctuations in the pebble temperature.

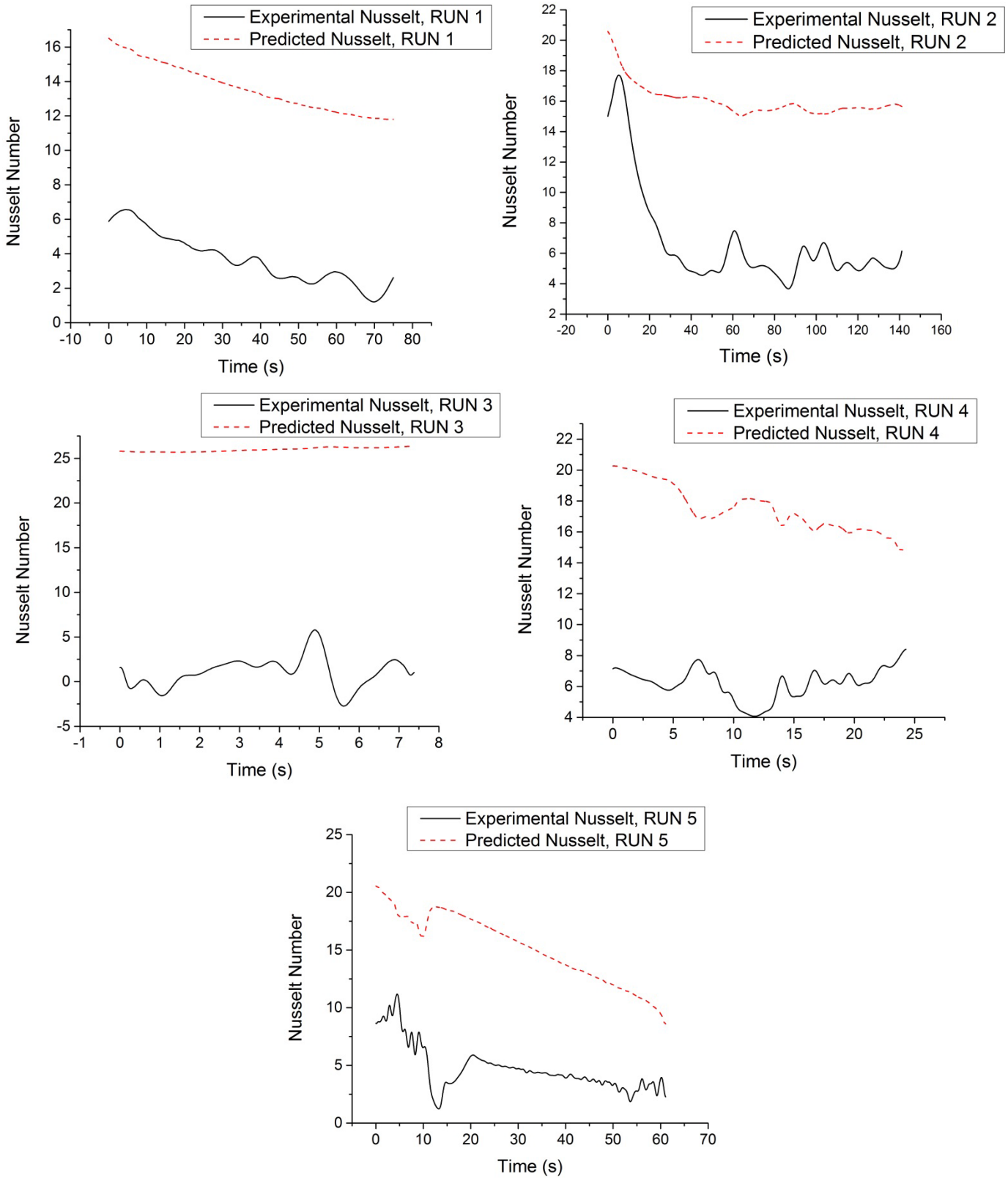

Figure 2-6: Comparison of the experimentally measured Nusselt number and the predicted Nusselt number for five runs.

From the data analysis, it was found that the radiation heat transfer accounted for up to 30 % of the total heat transfer between the pebble and the salt bath. The ratio of radiation heat transfer to convective heat transfer starts out small, on the order of 5%, and increases to about 30% as the transient continues. However this is not enough to explain the large difference that was seen between the experimental data and the prediction using the Churchill correlation.

2.1.5 Importance of Time Scale Ratios in Approximating to Quasi-Steady State Heat Transfer

A fully developed thermal boundary layer around the sphere implies that the heat transfer between the pebble and the bath can be approximated as quasi-steady. There are two time scales of significance for a single sphere being heated or cooled in a fluid by natural convection. One is the fluid transit time, which is the time it takes for a packet of fluid to move half the circumference around the pebble, denoted by τ_1. The second is the decay constant of the sphere temperature itself, denoted by τ_2 and derived from conservation of energy for a lumped capacitance system.

$$\tau_1 = \frac{L}{U} \tag{2.13}$$

$$\tau_2 = \frac{mc_p}{hA} \tag{2.14}$$

where L is the fluid transit distance around the pebble and U the average velocity of a packet of fluid travelling the distance L due to natural convection.

Quasi-steady state conditions can be assumed in the system if the fluid transit time τ_1 is much smaller than τ_2. The larger the ratio between τ_1 and τ_2, the less the temperature of moving packet of fluid is affected by the transient change in temperature of the sphere itself.

There are three ways of estimating the value of U. The three ways are:

a. Deriving U by establishing an equivalence between Gr and Re
b. Using scale analysis to estimate the order of magnitude of U
c. Using a multiphysics FEA code such as COMSOL to calculate U

It should be noted that U is a function of $|T_p - T_b|$, and is therefore decreasing as a function of time. It is 0 m/s when the system has reached thermal equilibrium.

a. Grashof-Reynolds equivalence

A natural convection U can be estimated using a method that equates Re with a modified Gr [35]. This is shown in the last line of Equation (2.15)

$$
\begin{aligned}
Gr' &= Gr^{1/2} \\
Gr' &= \left(\frac{\rho^2 g\beta (T_p - T_b) D^3}{\mu^2} \right)^{1/2} \\
\mathrm{Re} &= \frac{\rho U D}{\mu} \\
Gr' &= \mathrm{Re} \\
U &= (g\beta (T_p - T_b) D)^{1/2}
\end{aligned}
\tag{2.15}
$$

U derived in this manner has the units of velocity. Another expression for U can be derived in a similar way, by equating Gr to Re directly, which also has the units of velocity.

$$U = \frac{\rho g\beta (T_p - T_b) D^2}{\mu} \tag{2.16}$$

b. Scaling analysis to estimate order of magnitude for U

The order of magnitude for the characteristic velocity for natural convection can be found from Equation (2.17), which is a result of scaling analysis by A. Bejan [36] for high Pr fluids, as is the case with flinak.

$$
\begin{aligned}
U &\sim \frac{k}{\rho c_p D} (Gr\,\mathrm{Pr})^{1/2} \\
U &\sim \left(\frac{k g\beta (T_p - T_b) D}{c_p \mu} \right)^{1/2}
\end{aligned}
\tag{2.17}
$$

where U is the Bejan natural convection velocity, which is a function of flinak material properties and the diameter of the pebble.

c. COMSOL to estimate the order of magnitude for U

U was also estimated using a COMSOL Multiphysics model. The velocity distribution between the pebble surface and the crucible wall at cutline A is depicted. The maximum velocity at the cut line shown in Figure 2-7, calculated near the beginning of the transient simulation at 5 seconds, was found to be the highest (at 1 second the velocity was 0.0055

m/s). This maximum velocity predicted by COMSOL is shown in Table 2-3, where it can be compared with values predicted by scaling. It is interesting to note that there is a slight bump in the COMSOL velocity profile further out in the r direction. The velocity from 0.0085 to 0.0127 m is in the opposite direction to the velocity close to the pebble. This implies that a small natural circulation loop has been set up within the crucible. This recirculation is at a maximum at the cutline shown in Figure 2-7. This recirculation would serve to enhance heat transfer, which means that the temperature measured in the pebble may be lower than it would have been without any recirculation. This could also contribute to the lower than expected experimental Nusselt numbers.

Table 2-3 shows examples of the estimates for U for RUN 4. The values for U predicted by the three methods vary significantly. The COMSOL value for U was used to calculate

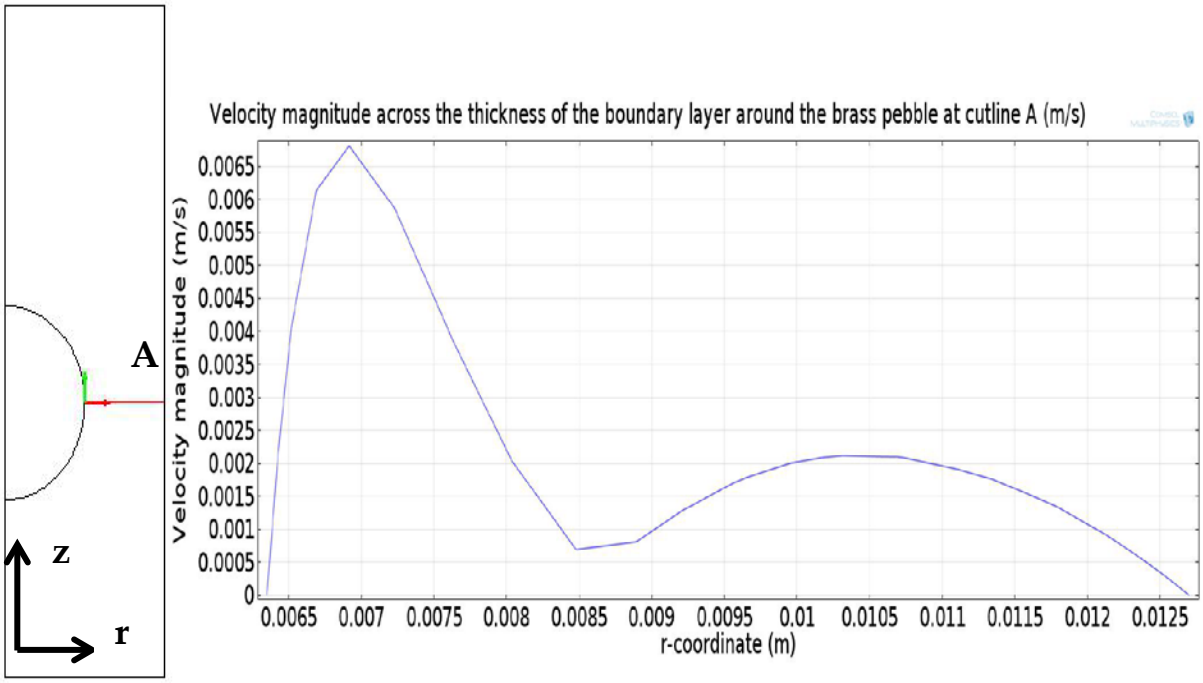

Figure 2-7: Diagram showing cutline A and the corresponding velocity boundary layer 5 seconds into the transient computation

τ_1 because it is likely to be the most accurate, as it is based on actual computation as opposed to scaling.

Table 2-3: Order of magnitude of U as estimated by three methods

Natural convection velocity, *U*	**Expression used to calculate *U***	**Natural convection velocity, *U* (m/s)**
Gr-Re equivalency	$(g\beta(T_p - T_b)D)^{1/2}$ $\frac{\rho g\beta(T_p - T_b)D^2}{\mu}$	0.1371 0.00351
Bejan	$\left(\frac{kg\beta(T_p - T_b)D}{c_p\mu}\right)^{1/2}$	0.0102
COMSOL	N/A	0.007

In order to ensure a quasi-steady fully developed boundary layer around the sphere, τ_2/τ_1 must be large. It is possible to develop a relationship between the size and properties of the sphere and the ratio τ_2/τ_1, given that the sphere material and the fluid remain unchanged.

$$\frac{\tau_2}{\tau_1} = \frac{\rho V c_p / hA}{\pi D / 2U} \to \infty$$
$$\frac{\tau_2}{\tau_1} = \frac{\rho c_p U}{3\pi h} \qquad (2.18)$$

Equation (2.18) shows that in order to ensure quasi-steady experimental conditions, ρ, c_p and U need to be high and h needs to be small. ρ and c_p can be changed by using a different material sphere. U is generally a function of the fluid properties, temperature difference and the diameter of the sphere. The temperature difference varies with time, so this is a difficult parameter to adjust. A larger D will ensure a larger U, but will also increase h given its dependence on Gr. This is counterintuitive because the transit distance L is larger. However, the natural convection velocity is also higher due to the dependence of h and U on the geometry of the sphere. It should be noted that too large a sphere will increase the Biot number, and thus cause the temperature to be non-uniform within it, and corrections will have to be made to take this into account. COMSOL models were set up to test the validity of Equation (2.18), and this is explained further in Section 2.1.6.

The temperature difference between the pebble and the bath is important because it impacts Gr which in turn impacts the U. The larger it is the higher U and the smaller τ_1. This is why the ratio of τ_1 to τ_2 becomes smaller as the temperature difference between

the pebble and the salt decreases as time progresses and the temperatures approach equilibrium, as shown in Figure 2-8.

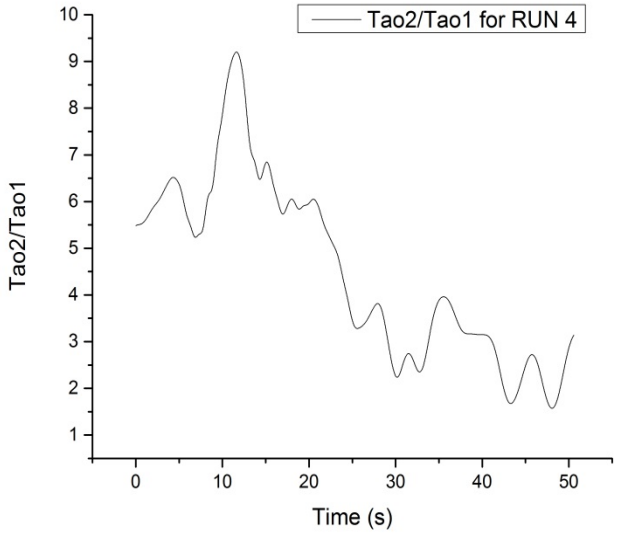

Figure 2-8: Ratio of time constants with respect to time, as calculated by Equation (2.18). τ_2 is the pebble temperature decay time scale and τ_1 is the fluid transit time scale

It has been found that designing experiments with heated pebbles, which would allow for steady state conditions, is challenging. Therefore there is merit in developing a way of achieving quasi-steady conditions. Equation (2.18) provides a start to accomplish this. These experiments will eventually be important for validating passive cooling in the reactor core of FHRs. The ratio τ_2/τ_1 shown in Figure 2-8 was calculated using Equation (2.18). The data used to calculate τ_2/τ_1 in Figure 2-8 came from experimental RUN 4, however all the runs show a similar trend. Experimental data for h and the COMSOL-estimated value for U were used in Equation (2.18). Using the predicted h (which is higher than the experimental) would result in a smaller time scale ratio. The smaller τ_2/τ_1 is, the larger the discrepancy between the steady state and transient solutions. Figure 2-8 shows that the ratio τ_2/τ_1 is never higher than 9.2. The average values are likely not high enough to achieve quasi-steady conditions.

It was found that approaching a large τ_2/τ_1 for the current experimental set up was not possible. The only experimental parameters that influence τ_1 and τ_2 are D, ρ and c_p of the sphere that is used. In order to ensure steady state conditions, a constant temperature boundary condition on the pebble surface could be imposed by using heating, and future iterations of the experiment will attempt this.

2.1.6 Transient Study Using COMSOL Multiphysics

The experimental set-up was replicated in COMSOL and a 60 s transient study was run. There were two reasons for performing a computational study to complement the experimental results:

a. To clarify the behavior of the transient heat convection between the sphere and the fluid with the same geometry as the experiment
b. To computationally find the natural convection velocity of the fluid around the sphere so it could be used as an estimate for U in τ_1

Computational Model

An axisymmetric 2D model, with a 'fine' mesh was developed. Continuity of heat flux was imposed on the boundary of the sphere. The inputs of the computational model are shown in Table 2-4. To replicate different experimental runs, T_p and T_b were varied accordingly. Calculations were then set up to evaluate the predicted Nu using Churchill's correlation (Equation (2.7)) at every time step.

Table 2-4: Inputs for the COMSOL Multiphysics model

Input parameter	**Units**	**Input value**
Geometry		
Sphere diameter	mm	12.7
Crucible inner diameter/height	mm	25.4/44
Boundary conditions		
Fluid bath temperature, T_b	°C	541
Pressure boundary conditions	atm	1
Initial conditions		
Fluid velocity	m/s	0
Sphere temperature, T_p	°C	683

COMSOL Results

Selected results from the COMSOL analysis are presented in Figure 2-9 and Figure 2-10. The results are shown for a pebble being cooled down by the surrounding bath, based on RUN 3.

Figure 2-9 shows a surface plot of the natural convection velocity magnitude 5 seconds into the transient, for a pebble being heated up by the surrounding bath. Figure 2-5 shows the temperature distribution of the pebble and the bath at 5 seconds.

Table 2-5 shows a comparison between the Nu as calculated by COMSOL and Nu as predicted by Equation (2.7). The COMSOL model also shows a reduction of the Nusselt number when compared to the Churchill correlation, but it is not as pronounced as the reduction seen in the experimental runs.

Figure 2-10 shows the calculated evolution of the thermal boundary layer at various time steps until equilibrium is reached between the pebble and the bath. The boundary layer shown is at cut line A in Figure 2-7. If the boundary layer thickness was uniform with time, this would validate the quasi-steady state assumption. However, we can qualitatively see from Figure 2-10 that the thickness of the thermal boundary layer changes significantly with time.

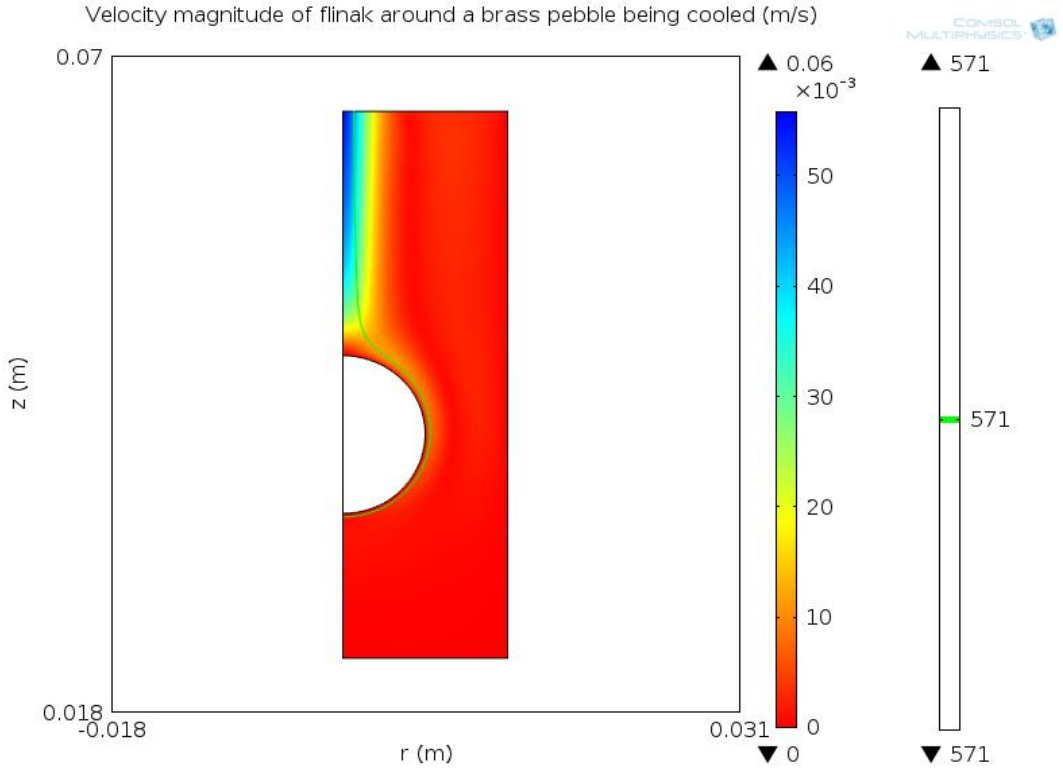

Figure 2-9: Surface plot of the velocity magnitude in m/s in the flinak bath at 5 seconds

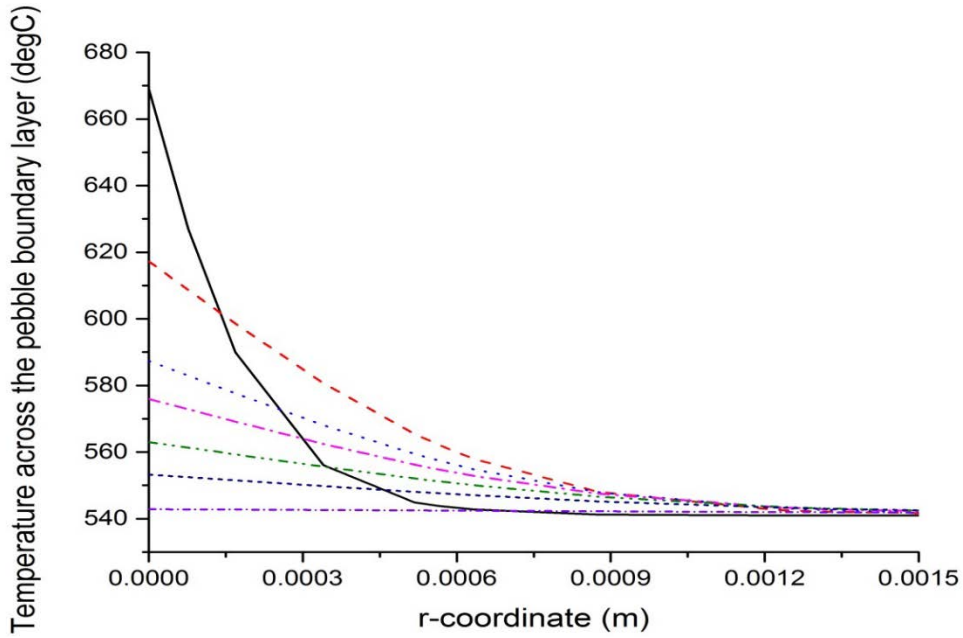

Figure 2-10: Temperature boundary layer at cut line A at various times of the transient from the COMSOL model

Table 2-5: Comparison of COMSOL Nusselt number to the Nusselt number predicted by Churchill's correlation

Time (s)	COMSOL Nu/Predicted Nu
0	2.55
5	0.854
7	0.842
10	0.832
15	0.800
20	0.779
30	0.726
40	0.674
60	0.559

Quasi-steady State COMSOL Models

Equation (2.18) proposed an expression that when approaching infinity would ensure quasi-steady state conditions for transient heat transfer from a low Bi sphere immersed in a fluid bath. A first attempt has been made using COMSOL to check if it is valid. This was done in two ways:

a. Increasing c_p of the sphere to 10,000 J/(kg K), which is about 26.5 times the value of brass, while keeping all the other properties the same
b. Changing the Pr of the fluid to lower values, while keeping other properties the same

The results are shown in Figure 2-11 and Figure 2-12. Figure 2-11 shows that using a high value for the specific heat c_p of the pebble decreases the difference between the calculated COMSOL Nu and Nu predicted by Churchill's steady state correlation, with a difference of about 5%. This is because using a high thermal capacity for the pebble in the COMSOL calculation slows its cooling rate. The expression in Equation (2.18) is sufficiently high to ensure quasi-steady state.

Lower Pr fluids were also studied using COMSOL as Pr directly affects Nu in the experiments, computations and predictions. Figure 2-12 shows that using a lower Pr fluid does not alone ensure quasi-steady state. This needs to be further investigated, as other studies suggest that Pr can affect Nu during transient forced convection [37].

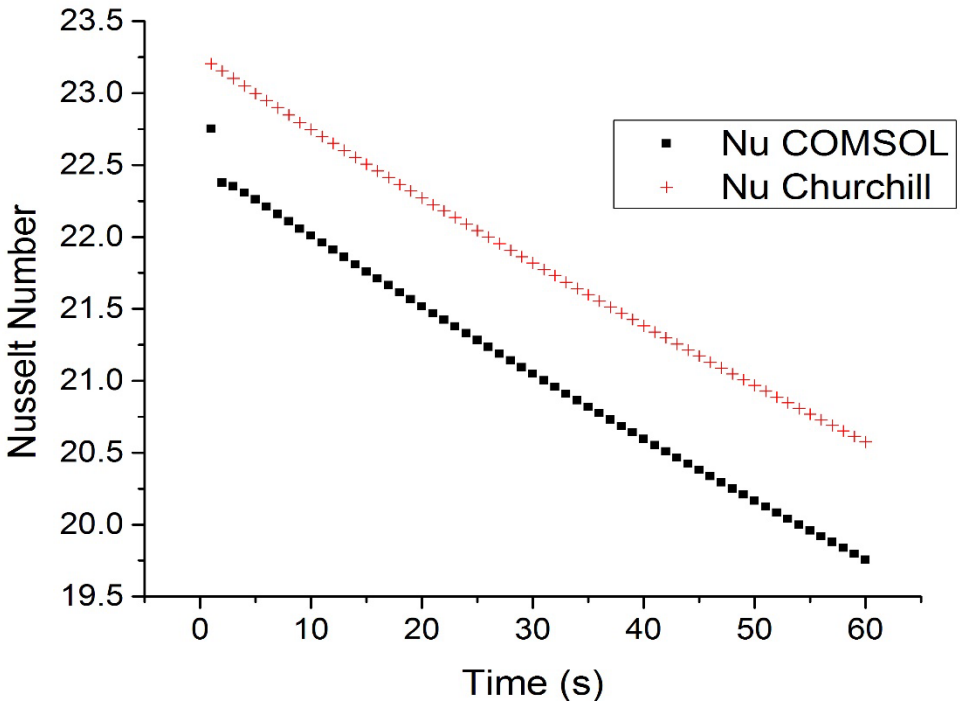

Figure 2-11: COMSOL Nu and predicted Nu for a pebble with a specific heat capacity of 10000 J/kg K

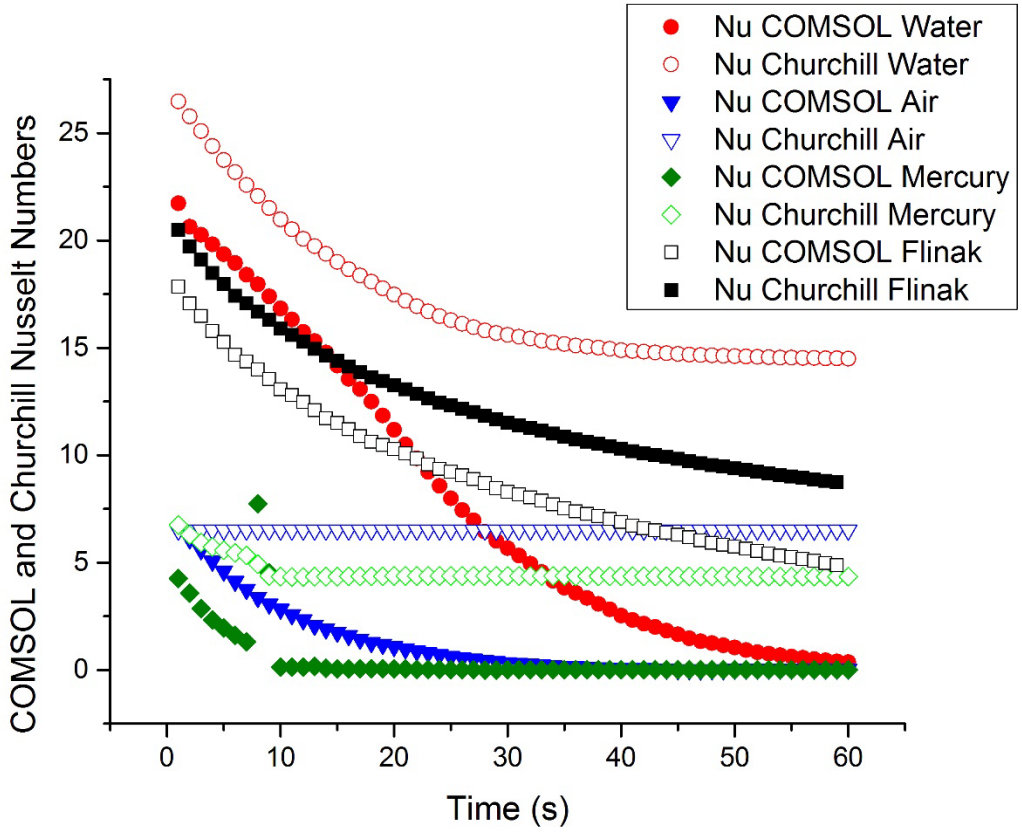

Figure 2-12: COMSOL calculated Nusselt and predicted Nusselt for fluids of differing Prandtl numbers

2.1.7 Discussion

Churchill's correlation used for predicting the Nusselt number for natural convection heat transfer of a sphere immersed in a high Prandtl number reactor coolant was compared with experiments and CFD simulation for transient heat transfer to a sphere immersed in a fluoride salt coolant. An instrumented brass sphere was immersed in a bath of molten flinak salt and the temperature of the sphere was recorded. The experimental Nusselt number was determined from this and compared to the corresponding predictions based on Churchill's correlation. It was found that the discrepancy between the predictions and the experimental data was large, with the experimental Nusselt number being at least three times smaller than predicted by the correlation. The reduction in Nusselt number could be related to the fact that the natural convection flow around the sphere was not fully developed during the transient, and thus Churchill's correlation is incorrect to use because it assumes steady state conditions. Two relevant time scales were used to determine if the boundary layer was fully developed – the temperature decay time constant of the sphere itself (τ_2), and the fluid transit time around half the sphere (τ_1). The larger the ratio τ_2/τ_1 is, the better the quasi-steady state assumption. However, in the current experimental runs this value was at most 9.2 and was at an average of 5.3, which is likely not high enough. A COMSOL Multiphysics model of the same experimental set up was developed to understand the phenomenology more closely. The COMSOL model also showed a reduction in the Nusselt number when compared to the correlation, but it was not as pronounced as in the experimental runs. The deviation between COMSOL and predictions was much less when a pebble c_p of 26.5 times that of brass was used, so that the cooling rate of the pebble slows down and quasi-steady heat transfer is approached. It is possible that the experimental and predicted Nusselt numbers were not accurately determined because the flinak fluid properties used were extrapolated in the temperature range near its freezing point, since data is not available in that range. This set of experiments showed that distortions due to transience need to be accounted for when designing experiments elucidating component scale phenomenology. Distortions due to transience can be reduced in two ways: (1) by using forced flow to increase the fluid velocity parameter (as shown in Chapter 3) or (2) using a heated element to ensure true steady state conditions (as outlined in Section 2.2).

2.1.8 Heat Transfer in Dowtherm A, the simulant fluid

An analogous experiment to the one described in Section 2.1 was carried out using Dowtherm A as the fluid. Isolated copper and brass spheres instrumented with Type T thermocouples were immersed in a bath of Dowtherm A.

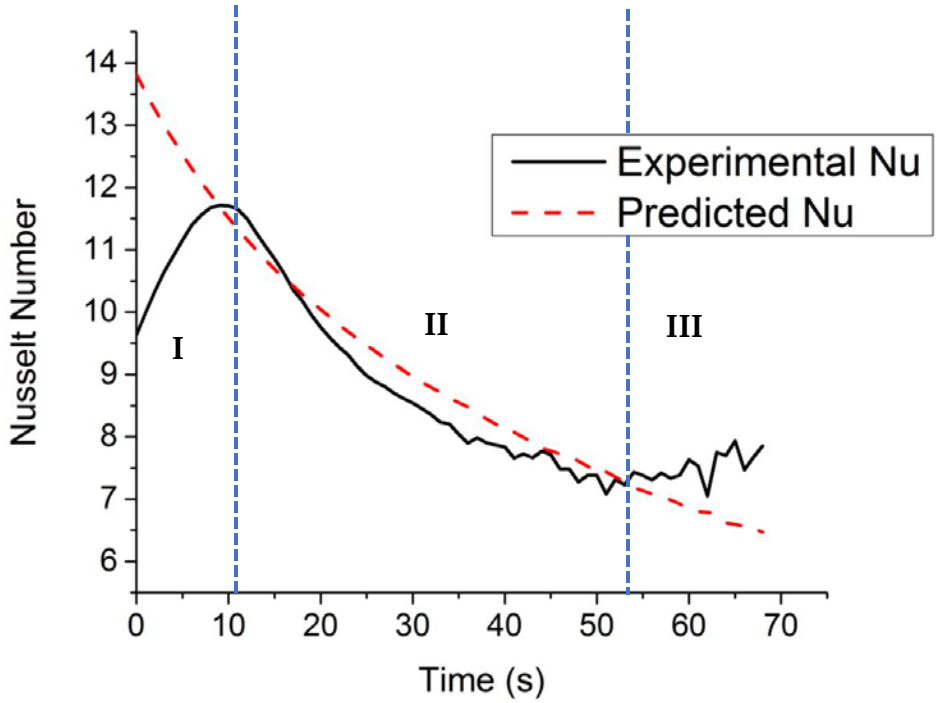

Figure 2-13: Predicted and measured Nusselt numbers from a copper isolated sphere in Dowtherm A as a function of time

Figure 2-13 shows the Nusselt number as a function of time for the experiment and the corresponding predicted values. The predicted Nusselt numbers were evaluated using the correlation for natural convection from an isolated sphere shown in Section 2.1.3. This was done for every time step based on the temperatures of the sphere and the fluid at that time step. It can be seen that the experimental Nusselt number is within 7% of the prediction between 10 and 50 seconds. The experimental range for the run shown in Figure 2-13 is shown in Table 2-6.Other transients show similar results. Phase II in Figure 2-13 shows the period during which useful data was collected. Phase I is the beginning of the transient and is subject to inaccuracies, and Phase III is at the end of the transient when equilibrium conditions have been met, meaning that the oil and the copper pebble are at the same temperature.

Table 2-6: Grashof and Prandtl number ranges for the Dowtherm A isolated sphere experiments

	Grashof range	**Prandtl range**
Figure 2-13 experimental run	18000-4000	19-23
Ranges for all Dowtherm A experimental runs	20000-2000	15-38

From Figure 2-13 it can be seen that the experimental Nusselt is close to the predictive correlation, which implies that the quasi-steady state assumption is valid. Indeed, the non-dimensional parameter shown in Equation (2.18) for the case shown in Figure 2-13 is ~10, which is higher than the flinak case.

2.1.9 Discussion

Although this experiment is a transient study, quasi-steady state conditions can perhaps be assumed. The ratio of the volumetric heat capacity between the fluid and solid phases is an indicator for whether quasi-steady conditions may be assumed. Figure 2-14 shows a schematic the volumetric heat capacities of an isolated copper pebble and the surrounding fluid. If the ratio of $(\rho c_p)_f / (\rho c_p)_s$ is smaller than 1, this implies that the temperature of the solid changes more slowly than the fluid temperature. This is the case with the Dowtherm A oil and copper, with a ratio of 0.51. This ratio is smaller than 1 but still close to unity. This means that there may be distortions due to transient effects. However the experimental results shown in Section 2.1.4 demonstrated that transient effects were not dominant. It is important to note that the measured heat transfer coefficients are being compared to correlations that assume steady state conditions. Table 2-7 compares the ratios of volumetric heat capacities for flinak and Dowtherm A.

As the temperature of the isolated sphere in the fluid bath is never constant (as it is cooling down or heating up), the thickness of the thermal boundary layer is continually changing. The question becomes whether it is possible to assume that at a single point in time we have quasi-steady state conditions or not. Therefore the time it takes for the boundary layer thickness to change should be much larger than the other time scale of interest, which is the fluid transit time around the sphere. This way it can be assumed that the thermal boundary layer forming around the pebbles is 'stationary' with respect to time in comparison to the time it takes for the fluid temperature to change. This is discussed in further detail in Section 2.1.5.

In Table 2-7 it can be seen that the ratio of volumetric heat capacities between flinak and copper is close to unity. This implies that the timescale for the boundary layer development and the timescale for the bulk fluid temperature change are of the same order of magnitude. Therefore quasi-steady state conditions are likely not attained, and this is further discussed in Section 2.1.5, in which a time scale ratio is derived for the isolated sphere case.

The experimental methodology discussed in Chapter 3 of this dissertation should be able to reduce any distortions due to transient effects as the temperature differences are designed to be periodic.

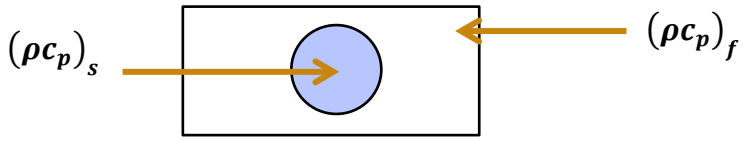

Figure 2-14: Diagram of the isolated sphere and oil (solid and fluid phases)

Table 2-7: Comparison of ratios of volumetric heat capacities in the isolated sphere experiments

	Fluid temperature (°C)	$(\rho c_p)_f / (\rho c_p)_s$	**Reference for material properties**
Flinak to copper	600	$4.0 \times 10^6 / 3.5 \times 10^6 = 1.14$	Flinak: [12] Copper: [38]
Dowtherm to copper	70	$1.8 \times 10^6 / 3.5 \times 10^6 = 0.51$	Dowtherm A: [39] Copper: [38]

2.2 Heat Transfer from a Vertical Heated Rod

To provide experimental demonstration of similitude between fluoride salt and Dowtherm A for steady-state natural convection heat transfer, it is helpful that there is a constant temperature difference between the fluid and solid. This is in order to avoid time scale distortions as were encountered in the single sphere transient tests. A heated rod assembly was immersed in Dowtherm A and the power to the heater was controlled. This allowed for constant temperature differences between the cartridge wall and the fluid with respect to time. This section gives some background on natural convection from vertical heated rods, details the experimental setup and the data collection procedure, and provides discussion of the experimental results. This series of experiments will be referred to throughout this section as 'CHEX' or Cartridge Heater Experiments. Scaling distortions are discussed, and the use of COMSOL in elucidating distortions is also detailed. The experimental results were then compared to high-temperature experiments performed using the molten salt flinak.

2.2.1 Background and Literature Review

Forced convection between a vertical cylinder and fluid has been well studied and characterized, due to it being the dominant mode of heat transfer between fuel rods and the surrounding coolant in nuclear reactors. Natural convection from a vertical cylinder has also been extensively studied for a wide range of Rayleigh numbers

Experiments performed at Oak Ridge National Laboratory (ORNL)

Natural convection heat transfer coefficients from vertical heater rods in fluoride salts were measured by Oak Ridge National Laboratory (ORNL), Electrochemical Systems, Inc., and Texas A&M University, and the experiments were performed at Oak Ridge National Laboratory [40]. A nickel cell was filled with flinak and heater rods were inserted into it under an argon atmosphere. The heater was instrumented with embedded thermocouples, and thermocouples were also used to measure the temperature of the flinak in the cell. The data from CHEX was compared to the ORNL data.

Local Grashof Number

In this set of experiments the Grashof number is defined differently to the isolated sphere case. The length dimension varies depending on the position of the thermocouple at which a temperature measurement was taken.

$$Gr = \frac{\rho^2 g \beta (T_f - T_s) \mathrm{x}^3}{\mu^2} \tag{2.19}$$

In Equation (2.19), ρ is the density of the fluid (Dowtherm A or flinak) in kg m^{-3}, μ the viscosity in kg m^{-1} s^{-1}, g the gravitational acceleration in m s^{-1}, β the coefficient of volumetric expansion in K^{-1}, and x the thermocouple location from the bottom of the heater rod assembly in m. All material properties were evaluated at the film temperature, shown in Equation (2.8), which is the average temperature between the heater rod surface and the bulk fluid temperature at that depth in the beaker.

Local Rayleigh Number

The Rayleigh number is defined as the product of the Grashof and Prandtl numbers. Ra_x refers to the Rayleigh number at location x, and is the product of Gr_x and Pr.

Scaling between CHEX and Flinak experiments

Since natural convection heat transfer was being studied, it was important to match Grashof and Prandtl numbers. Correlations from the literature (Equations (2.21) and (2.22)) suggest that matching the Rayleigh number should be sufficient, which means that only the product of the Grashof and Prandtl numbers need to be matched. Through scale analysis it can be shown that when Pr >> 1, the Nusselt number is solely a function of the Rayleigh number for external natural convection flows, whereas for low Pr numbers

Nusselt is a function of the Rayleigh and Prandtl numbers. At high Prandtl numbers, there is a balance between friction and buoyancy forces within the boundary layer [41]. Nonetheless an attempt was made to directly match Prandtl number between the Dowtherm A and flinak, as it may have an effect on the transitional Rayleigh number from laminar to turbulent flow. This is further described in Section 2.2.5.

Table 2-8 shows the range of Prandtl and Grashof numbers that were achieved during the CHEX experiments. The high Prandtl number case is applicable to the CHEX experiments given that the Prandtl number range achieved is much larger than unity. The CHEX experiment was designed such that the conditions encompassed the ORNL experiments.

Table 2-8: Range of Prandtl and Grashof numbers attained during CHEX experiments

	CHEX	**ORNL Flinak experiments**
Prandtl range	10-40	6-11
Grashof range	10^5-10^9	10^5-10^9

2.2.2 Objectives

The main experimental objective was to collect data to show similitude between simulant oils and fluoride salts for natural convection heat transfer. With a heated rod, steady state conditions are easily obtained, and thus the transient response distortions discussed in Section 2.1 are eliminated. A uniform heat flux boundary condition was established at the wall of the heated vertical cylinder.

2.2.3 Experimental Setup and Experimental Methodology

Three cartridge heaters of various lengths were purchased from McMaster-Carr. The dimensions of the heaters used in the experiments are shown in Table 2-9, and is shown in Figure 2-15 on the left. The cartridge heater was inserted into a copper sleeve. Three thermocouples were inserted in between the cartridge and the sleeve at different heights, shown in Table 2-10. The reason for three thermocouple locations was to collect data for a range of Rayleigh numbers. Silicon cement was used to attach the thermocouples to the cartridge heater. Pictures of the cartridge heater assembly are shown in Figure 2-15 and Figure 2-17. These thermocouples were connected to a data acquisition system from Omega (OM-DAQ-USB-2401). The cartridge heater power was controlled using a 400 W DC power supply from Mouser Electronics (967-Z160-2.6-U). In this way the exact power delivered to the heated rod was known, and was used for data reduction as shown in Section 2.2.4.

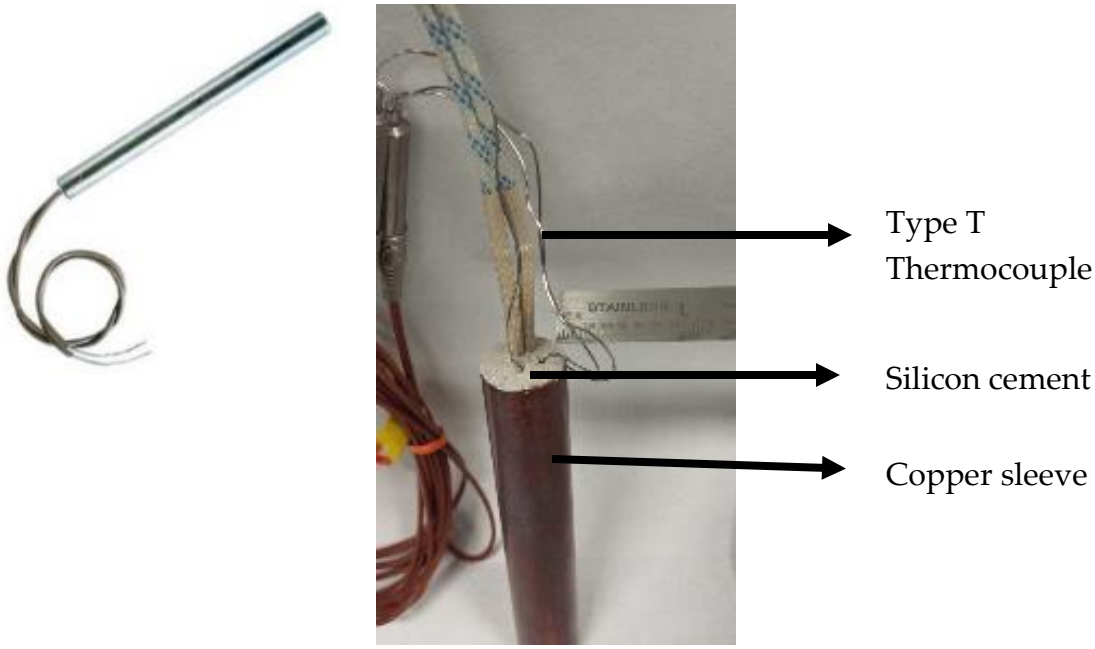

Figure 2-15: Left - cartridge heater. Right - Instrumented cartridge heater in copper sleeve

A 1000ml Pyrex beaker was filled with Dowtherm A, and this was used as the bath in which the instrumented cartridge heaters were immersed. Additionally three thermocouples were located in the oil bath at the same depths as the thermocouples located in the heated rod. All the thermocouples used in this experiment were fine diameter Type T (0.02" or 0.508mm in diameter). These three fluid thermocouples were attached to a ring clamp to keep them at the same axial position for the duration of the experimental runs. All instrumentation was separately calibrated using an ice bath and a uniformly heated oil bath. For some experimental runs a hot plate was used to keep the Dowtherm A at a constant, high temperature. The heated rod assembly was clamped in place such that it was fully immersed in the Dowtherm A oil bath, with the top of the assembly flush with the surface of the Dowtherm A fluid, as shown in Figure 2-16. Power was supplied to the cartridge heater and the thermocouple temperatures were recorded for a period of time. After the initial transient, steady state conditions were reached. This means that the temperature difference between the cartridge and the oil was constant.

Temperature readings from the thermocouples were recorded as a function of time and were logged at a frequency of 1 Hz (once a second).

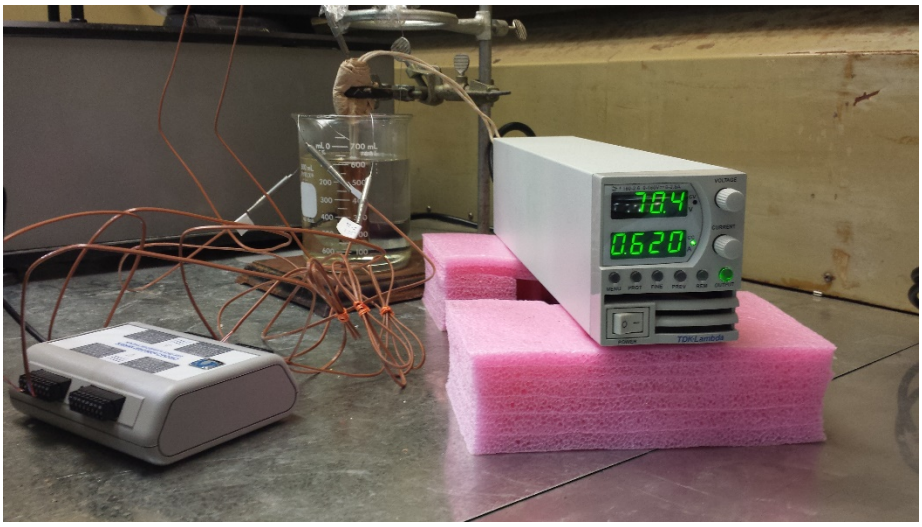

Figure 2-16: Experimental setup including the DC power supply and the DAQ

Table 2-9: Cartridge heater dimensions

Cartridge	Diameter (m)	Length (m)	Max Power (W)	Date of Run
H-1	0.009525	0.0635	75	2015-06-25
H-2	0.0127	0.1143	200	2015-06-29 and 2015-06-30
H-3	0.009525	0.1016	130	2015-08-06 and 2015-08-07

Table 2-10: Copper sleeve dimensions

Copper Sleeve	Outer Diameter (m)	Length (m)
S-1	0.01905	0.0699
S-2	0.01905	0.1205
S-3	0.01905	0.1080

Heated rod assembly

Copper sleeves were manufactured from copper rod stock for each cartridge heater. Three notches the length of the sleeve were sawed to allow space for the thermocouple. The cartridge heater was painted with a thin layer of silicon cement and inserted into the copper sleeve where the bottom of the cartridge was flush against the sleeve. The silicon cement was purchased from Omega (OMEGABOND 400). Silicon cement was chosen as

the binding material for several reasons. It has a low coefficient of thermal expansion, high thermal conductivity and is designed for attaching thermocouples to surfaces [42]. Thermocouples were installed in three axial locations on the cartridge heater, and the exact location was measured from the bottom of the copper sleeve, taken as zero. Furthermore the thermocouples were located at three different circumferential positions, about 120° apart. Though the clearance between the cartridge heater and the inner diameter of the copper sleeve was designed to be tight, the cartridge heater may still have been installed non-concentrically during assembly. This would result in a non-uniform circumferential distribution of temperatures measured at the surface of the heated rod. Thus it is useful to have thermocouples at different circumferential positions in all three assemblies.

The thermocouples were inserted while the cement was still wet, allowing for easy insertion. The length of the copper sleeve was measured using Vernier calipers. The length of thermocouple to be inserted into the sleeve was also measured. In this manner the position of the thermocouples from the bottom was determined. In short, H-1 was combined with S-1 to form A-1, and similarly for the remaining heater rod assemblies.

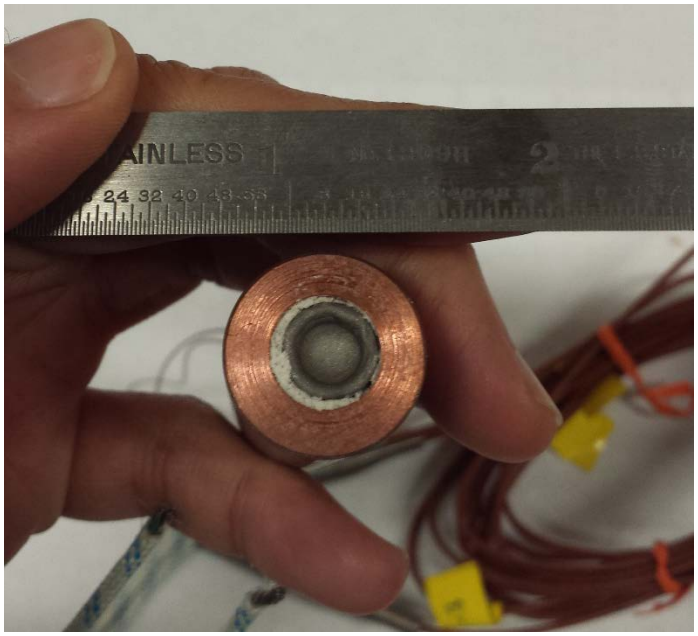

Figure 2-17: Bottom surface of the heated rod assembly

Table 2-11: Thermocouple axial locations in the heated rod assembly

Heated Rod Assembly	Position of Top Thermocouple (m)	Position of Middle Thermocouple (m)	Position of Bottom Thermocouple (m)
A-1	0.0635	0.0381	0.0127
A-2	0.0893	0.0537	0.0120
A-3	0.0762	0.0635	0.0381

Biot number

It is important to consider the Biot number in the cylinder. This is because the thermocouples are located between the cartridge heater and the copper sleeve. If the Biot number in the copper sleeve is small, the temperature on the inside of the sleeve and the outside of the sleeve can be assumed to be the same, as shown in Figure 2-18. A low Biot number implies that the temperature distribution in the sleeve is constant. This is the case in the CHEX experiments given the high conductivity of the copper and the thinness of the sleeve itself.

$$Bi = \frac{hL}{k_s} \tag{2.20}$$

In equation (2.20), *Bi* is the Biot number, *h* the convective heat transfer coefficient between the heated rod and the Dowtherm A oil in W m^{-2} K^{-1}, *L* the length dimension, here the thickness of the copper sleeve and k_s the thermal conductivity of the copper in W m^{-1} K^{-1}. Here *h* was estimated using typical conditions from the experiment. The highest value of h for each assembly was used, to get the highest possible Biot number.

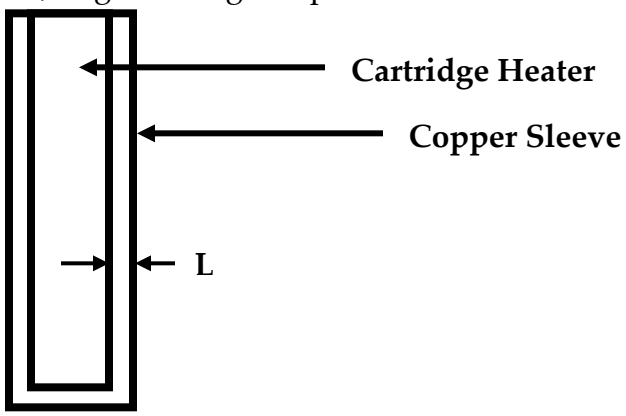

Figure 2-18: Schematic of the heater rod assembly and representation of length scale 'L'

For the three heated rod assemblies, the Biot numbers of the sleeves are shown in Table 2-12.

Table 2-12: Biot number in the copper sleeve for 3 heated rod assemblies

	Sleeve thickness, L (m)	**Heat transfer coefficient, h ($Wm^{-2}K^{-1}$)**	**Copper thermal conductivity, k_s ($Wm^{-1}K^{-1}$)** [38]	**Biot Number**
A-1	0.00476	250	400	0.0030
A-2	0.00318	250	400	0.0020
A-3	0.00476	280	400	0.0033

2.2.4 Data reduction procedure

This section describes the procedure that was used to extract the heat transfer coefficient information from the experimental data, and the predictive correlations used for the comparison between the experiment and the literature.

Flat plate correlations

Flat plate correlations were used to predict the Nusselt number for each of the experimental runs, in order to compare it to the experimentally derived Nusselt number. The correlations used for laminar and turbulent flow are provided in Equations (2.21) and (2.22) respectively [43]. The correlations were specifically for the case of uniform heat flux at the surface. This is the condition seen in the CHEX experiments as the power to the heated rod was kept constant throughout an experimental run. Laminar flow occurs at low Ra numbers, and refers to flows in which there is no significant mixing between layers, and mixing is solely due to molecular diffusion. Turbulent flow occurs at high Ra numbers, and is characterized by random multi-dimensional motion throughout the flow field [44]. In natural convection flows along a vertical flat plate, the transition between laminar and turbulent happens between $10^8 < Ra < 10^9$ [45].

$$Nu_{lam} = 0.56 Ra_x^{1/4} \tag{2.21}$$

$$Nu_{turb} = 0.13 Ra_x^{1/3} \tag{2.22}$$

Note that for Nu_{turb}, the Nusselt number depends upon Rayleigh number to the 1/3 power, meaning that the heat transfer coefficient becomes independent of the position on the vertical surface. Since the heat transfer coefficient was not the same along the length

of the heater, even during the high Rayleigh number cases, it is likely that fully turbulent flow was not attained in these experiments.

In CHEX the flow regime is dependent on the thermocouple position and the temperature difference between the heated rod and Dowtherm A (which is dependent on the power input to the heated rod). Since CHEX explores Rayleigh numbers up to 10^{10}, laminar, transition and turbulent regimes are all studied. The reported transition Rayleigh number was experimentally found for fluids of Prandtl numbers close to 1. In the reported experimental setup, it is not possible to visualize the fluid flow along the heater rod assembly as the experimental run is occurring. Therefore a COMSOL simulation was performed parametrically varying heater power according to the experimental runs. The velocity boundary layer was plotted to see if turbulence was dominant or not. This is shown further in Section 2.2.6.

Extraction of the heat transfer coefficient

Using a simple energy balance expression, the heat transfer coefficient could be extracted from the collected thermocouple data and power data. The following steps were applied for the heat transfer coefficient extraction:

1. The thermocouple data was imported into OriginPro 2016 version 9.3. It was then smoothed using a 20-point window FFT, as described in Section 2.1.3. The temperatures were recorded as a function of time.
2. The film temperature is calculated at all three axial locations at which instrumentation is positioned. The film temperature is needed to evaluate fluid thermophysical properties. This was done at every recorded time point.
3. Using the temperature difference between the heated rod assembly and the fluid in the vicinity, the heated rod assembly surface area and the power supplied to the cartridge heater, the heat transfer coefficient was extracted:

$$Q = hA(T_s - T_f) \Rightarrow h = \frac{Q}{A(T_s - T_f)} \tag{2.23}$$

The heat flux from the heated rod was evaluated by dividing the power by the surface area of the copper sleeve. In Equation (2.23), h is the experimentally-derived heat transfer coefficient in W m^{-2} K^{-1}, Q the power supplied to the heater in W, A the surface area of the curved part of the heated length of the copper sleeve in m^2, T_s the temperature of the cartridge at a particular axial location in K, and T_f the temperature of the Dowtherm A fluid at the same particular axial location in K. Q was evaluated by multiplying the current and voltage supplied to the cartridge heater, which was recorded during every experimental run using the DC power supply. h was also evaluated as a function of time,

even though only the steady state results were used to compare against the flinak data and pre-predictions. h was calculated at all three thermocouple locations.

4. The experimentally-derived Nusselt number was then calculated using h.

$$Nu = \frac{hx}{k_s} \tag{2.24}$$

It is important to note that the length scale in Equation (2.24) is the axial position of the thermocouple, the distance between the bottom and the thermocouple location. Three Nusselt numbers were calculated for each experimental run that was conducted.

5. The Prandtl and Grashof numbers were evaluated for each thermocouple position, as defined in Section 2.2.1, and from them the Rayleigh number was deduced. The Rayleigh number was recorded to discern the fluid flow regime along the heated rod assembly.
6. The Prandtl and Grashof numbers were then used to calculate the predicted Nusselt for laminar and turbulent flow. The ORNL flinak correlations for laminar and turbulent were also evaluated. A discussion of the comparison is provided in Section 2.2.5.
7. The uncertainty on h was calculated. This included uncertainties on instrumentation and geometry of the heated rod assembly.

2.2.5 Comparison of Dowtherm A Experimental Data to Flinak Experimental Data and Predictive Correlations

It was found that there was considerable axial variation in fluid temperature when the heated rod was immersed in Dowtherm A. This fluid axial temperature variation was about 3.5 °C. The fluid temperatures near the top of the heated rod were greater than at the bottom, implying thermal stratification in the beaker. Fluid thermocouples were therefore immersed at varying depths to account for this. They were placed at the same heights as the surface-reading thermocouples on the heated rod.

Flinak experimental data

The data collected with Dowtherm A was compared to data that was collected in an analogous way using flinak at ORNL. The data was collected for Rayleigh numbers up to 10^{10}, overlapping the CHEX experimental range. Three heater rods were used with thermocouples located at different axial positions. Three salt bath temperatures were measured. From the collected data, flinak-specific correlations were developed for laminar and turbulent natural convection heat transfer. These correlations were

subsequently used to compare with the CHEX data. The correlations for laminar and turbulent are shown in Equations (2.25) and (2.26) respectively.

$$Nu_{lam} = 0.665 Ra_x^{2.46} \quad (2.25)$$

$$Nu_{turb} = 0.438 Ra_x^{0.272} \quad (2.26)$$

In the Dowtherm A experiments, the heated rod was enclosed in a copper sleeve, whereas this was not the case in the flinak studies. The copper sleeves are thin enough to have a Biot number less than 1 (Table 2-12), so the temperature at the surface of the copper sleeve can be assumed to be the same as the temperature at the surface of the cartridge inside.

Experimental results and comparisons with predictions and ORNL flinak data

As shown in Figure 2-19, the predictive correlations and ORNL correlations were plotted for a wide range of CHEX conditions. This is because the critical Rayleigh number (the Rayleigh number at which transition occurs) is not accurately known for Prandtl numbers higher than the air-water range. Bejan and Lage [46] postulated based on existing experimental data that for higher Prandtl number fluids, the transitional Rayleigh number was higher than the generally quoted value of 10^9 [13]. However they also state that there is a lack of studies for transition for natural convection in high Prandtl number fluids. This implies that most of the data collected from CHEX and the ORNL experiments were for laminar flow, although this is further discussed in Section 2.2.7. Each data point has an error bar although some are too small to see and are hidden by the shape of the data point itself. The ORNL turbulent correlation and the flat plate turbulent correlation were plotted for $Ra > 10^8$.

It is useful to analyze the graph in Figure 2-19 in 3 parts, as labelled.

At low Rayleigh numbers below 10^8 (Region 1), the majority of the measured Dowtherm A Nusselt numbers are within 8% of the laminar flat plate predictions and the ORNL laminar correlation for flinak. Two data points are outliers, and have discrepancies of up to 35%. Both these points come from the same heated rod assembly, A-1, implying that the cartridge heater or the instrumentation may have been defective.

Most of the data points in Region 2 are within 24% of the ORNL laminar correlation and the laminar flat plate correlation, with about 70% of the data within 10% of the laminar flat plate correlations. Some of the experimental data is lower than the prediction and the ORNL correlation. These data points are mostly from the thermocouple locations at the bottom of the cartridge heater. It is possible that the temperature difference at this

location was overestimated, resulting in lower experimental heat transfer coefficients. The fluid at the bottom of the beaker is colder than the upper region.

It should be noted that for $10^9 < Ra_x < 10^{10}$, most of the data points lie in between the ORNL correlations for laminar and turbulent flows. This implies that the Dowtherm A data may lie within the transitional range. However six data points are higher than the turbulent flat plate correlation by 25%.

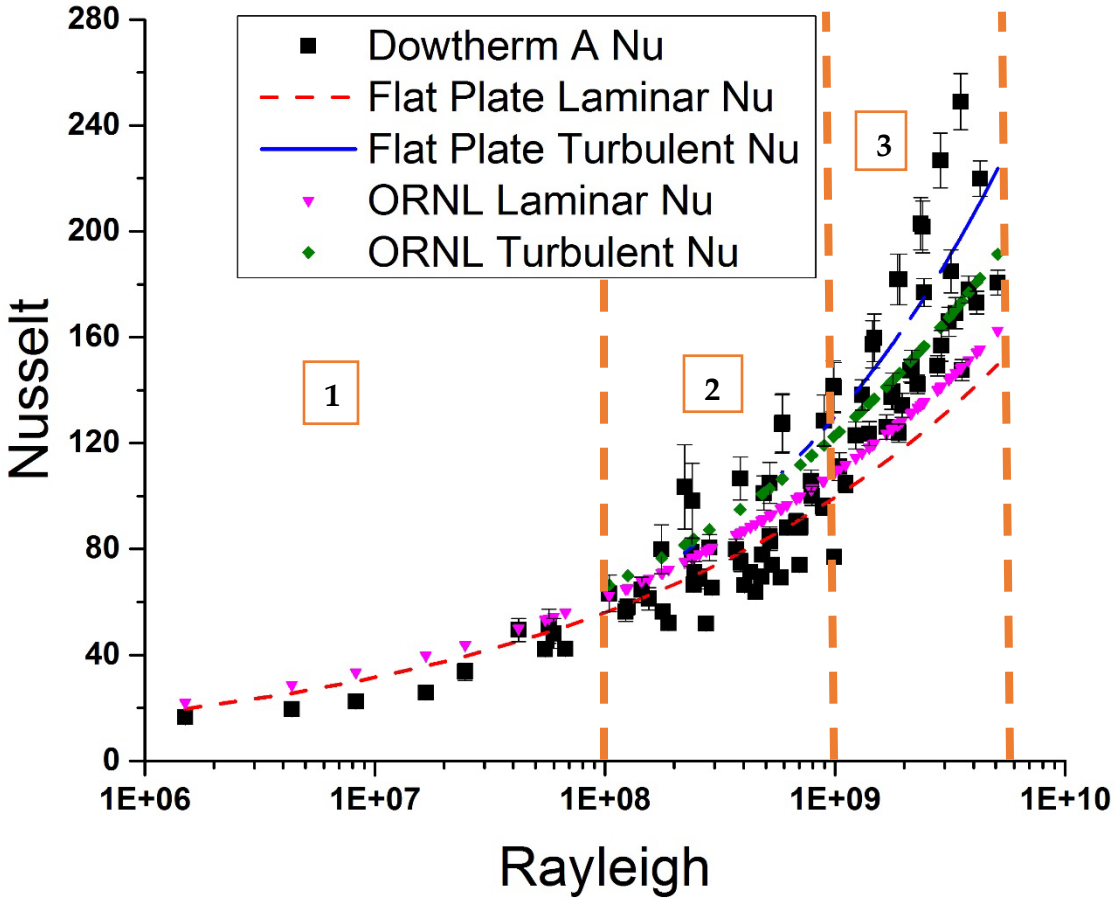

Figure 2-19: Nusselt number against Rayleigh number for CHEX, ORNL flinak experiments and predictions

2.2.6 COMSOL Computational Results

COMSOL was used to model the Dowtherm A and ORNL flinak experiments. The COMSOL models kept the geometry of the heated rod assembly and the container. An axisymmetric 2D model with a 'fine' mesh was developed. Continuity of heat flux was imposed on the boundary of the heated rod assembly touching the fluid. Examples for the inputs of the computational model are shown in Table 2-13.

Table 2-13: COMSOL input parameters for CHEX and ORNL experiments

Input Parameters	Units	Input Values	Comments
Dowtherm A (CHEX)			
Geometry			
Heated rod assembly			
-Radius	m	0.00476	
-Length	m	0.108	
Container	m		
-Radius	m	0.0603	
-Length	m	0.152	
Boundary Conditions			
Temperature continuity at the boundary of the heated rod			
Pressure at outlet (top boundary to the air)	Bar	1.01	
Initial Conditions			
T_f (initial Dowtherm A temperature)	°C	22	
T_s (initial heated rod assembly temperature)	°C	22	
Heat Source	W	94.84	COMSOL simulations were done for the experimental range, from 21 W – 111 W
Flinak (ORNL)			
Geometry			
Heated rod			
-Radius	m	0.00635	
-Length	m	0.271	
Container			
-Radius	m	0.0235	
-Length	m	0.274	
Boundary Conditions			

Temperature continuity at the boundary of the heated rod			
Pressure at outlet (top boundary to the air)	Bar	1.01	
Adiabatic conditions at the boundaries of the flinak cell (container)			
Initial Conditions			
T_f (initial Dowtherm A temperature)	°C		
T_s (initial heated rod assembly temperature)	°C		
Heat Source	W	213	COMSOL simulations were done for the experimental range, from 210 W to 525 W

Heat conduction was modeled in the heater and convection in the surrounding fluid. Buoyancy forces were modeled in the fluid region. Comparisons were made between the two fluids for the same Prandtl number case. The temperature boundary layers and velocity boundary layers are depicted in Figure 2-20 and Figure 2-21. Steady state studies were performed because though the initial part of the experimental run is transient in nature, only the steady state results were used to compare Nusselt numbers with the predictions and ORNL data using flinak. Zero heat loss through the container walls was assumed in the flinak case.

Figure 2-21 shows the natural convection velocity distribution along the heated rod in the flinak-filled cell. Figure 2-20 shows the same for Dowtherm A. It can be seen that while the velocity magnitudes are similar in both cases (as the Grashof numbers ranges in both experiments were designed to overlap) the container has a stronger effect in the flinak case. A prominent natural circulation flow can be seen in Figure 2-21 compared to the much fainter one in Figure 2-20. The narrower the container, the larger the natural circulation effect. This implies that the temperature at the surface of the heater may be

lower than it would be without the additional recirculation. This may contribute to lower experimental heat transfer coefficients in the ORNL data. Figure 2-19 shows that at high Rayleigh numbers, the ORNL data is lower than the turbulent plate correlation. This could be one of the contributing factors, and could possibly be a cause for the distortion between the Dowtherm A and the flinak data.

A more in-depth discussion regarding some of the scaling distortions present in the COMSOL models is provided in Section 2.2.7.

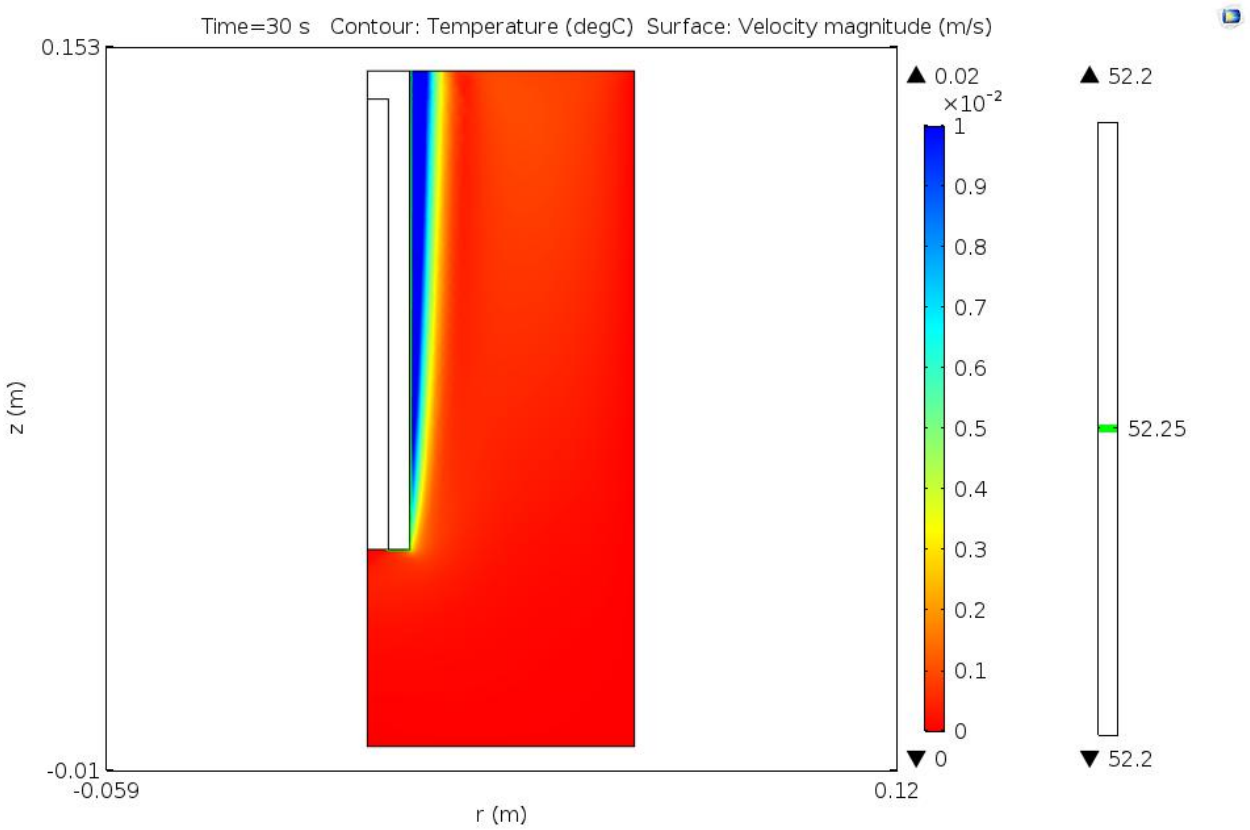

Figure 2-20: Fluid velocity distribution along the heated rod assembly in Dowtherm A

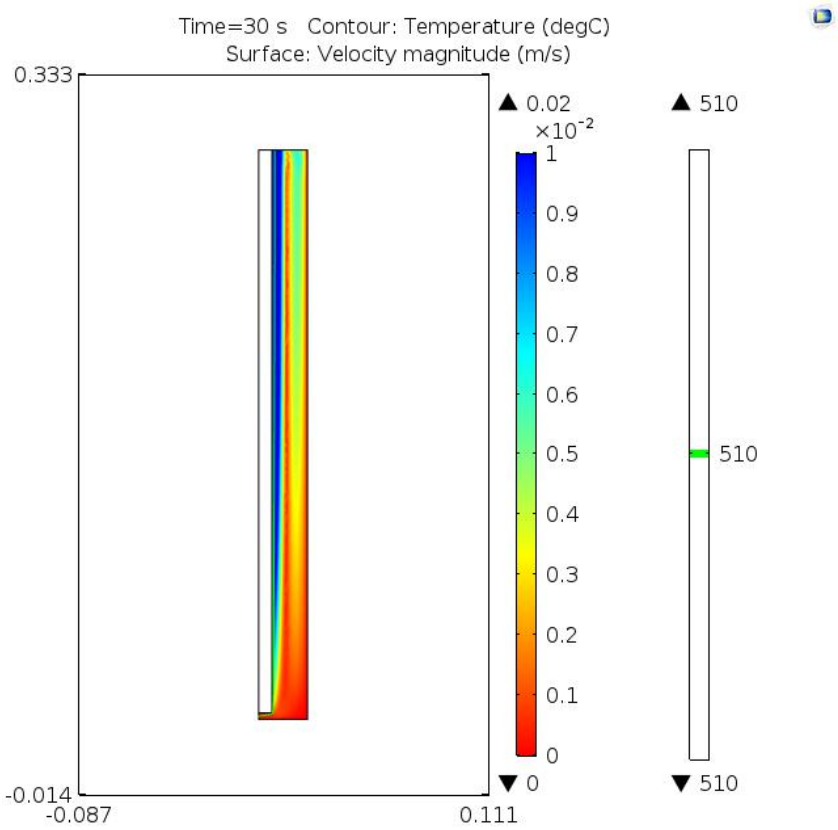

Figure 2-21: Velocity distribution along the heated rod in flinak

2.2.7 Scaling distortions

This section goes through some of the possible contributors to explain distortions between the Dowtherm A and flinak experiments.

Thick cylinder limit

If a cylinder diameter is large enough, the curvature of the boundary layer around it can be neglected. This is known as the 'thick cylinder' limit, as shown in Equations (2.27) ([36], [47]). Within this limit, the simple correlations for vertical plate plates can be used instead of the more complex ones for vertical cylinders.

$$\frac{D}{L} > Ra^{-1/4} \tag{2.27}$$

Table 2-14 shows the ratios of diameter to length for the different cartridges, and compares them to the largest possible value for $Ra^{-1/4}$ and. D is the copper sleeve diameter in m and L is the length of the heated rod assembly in m. The smallest values of Gr and Ra were used.

Table 2-14: Thick-cylinder limit for the three heated rod assemblies

Heated Rod Assembly	D/L	Equation (2.27)
A-1	0.27	0.018
A-2	0.16	0.032
A-3	0.18	0.018

It can be seen that the thick cylinder assumption is valid in all the studied cases according to Equation (2.27). Therefore it is a valid assumption to treat the cylinder as a vertical flat plate and ignore the curvature of the cylinder. This was further checked by using the full-form vertical cylinder Nusselt number correlations which include the curvature terms [48]. It was found that there was less than 1% deviation between this and the flat plate correlations. This is not likely to be a source of distortion between the experimental results in Dowtherm A and the predictive correlations or the flinak results.

The effect of Prandtl number on transition from laminar to turbulent flow

For natural convection flows along flat plates, the critical Rayleigh number (transition from laminar to turbulent) occurs at around Ra ~ 10^9 according to the literature[45]. According to empirical data however, the transition is dependent on the Prandtl number of the fluid [46]. The higher the Prandtl number the higher the critical number. Bejan and Lage state that the transition occurs as follows in Equation (2.28).

$$Gr \sim 10^9 (10^{-3} < \mathrm{Pr} < 10^3) \qquad (2.28)$$

The highest Rayleigh number in the Dowtherm A study was 10^{10}. Given that the maximum Prandtl number in this study was 40, it is possible that the data points at the higher Rayleigh numbers were in a transition regime and not the turbulent regime. Therefore it may be inaccurate to compare the higher Rayleigh numbers data to turbulent flat plate correlations. It is harder to find transition regime Nusselt number correlations for natural convection flows. This might be another cause for the distortions at the higher Rayleigh number data. This could also explain why the ORNL Nusselt numbers for flinak between $10^9 < \mathrm{Ra} < 10^{10}$ is lower than the turbulent predictive correlations – it is likely to be in the transition regime.

Other possible causes for distortion

It is possible that there are distortions at the ends of the heated rods. Though the vertical flat plate Nusselt number correlations are used, distortions are likely at the top and

bottom ends of the heated rod given that it is not infinitely long. The distortions caused can be visualized using COMSOL. During natural convection the flow across the rod is largely laminar in Dowtherm A, but not in flinak.

Radiation heat transfer was found to be non-negligible in the isolated sphere tests immersed in flinak. However, it is not a significant contributor to distortions in CHEX. This is not only because the metal surface of the copper sleeve has low emissivity, but also because the temperature difference between the Dowtherm A and the heater assembly was small. The absolute temperatures in the experiment were overall smaller as well. The radiation heater transfer accounted for less than 3% of the total heat transferred from the heater. The radiation correction was included in the flinak cyclindrical heater tests [40].

Additionally there could be non-uniformities in the heater. It is possible that the axial distribution of power in the cartridge heater is not uniform, due to irregularities in the manufacturing process of the heating element. Furthermore it is possible that the thermocouple near the bottom of the heated rod assembly was located in a region where the boundary layer was still developing. This would imply higher Nusselt number recorded at this location (implying that the lowest Grashof number case for each run may have had a higher Nusselt number than predicted). There were also some difficulties mixing the fluid. In the Dowtherm A case the fluid could not be constantly mixed as that would affect the fluid thermocouple positions. Thus flow stagnation was seen in the beaker with hotter fluid at the top. However, this effect should not play a large role in distortions in the Nusselt number. The fluid temperature was measured at 3 axial locations, and the heated rod assembly temperatures were measured at the same elevation. These are the only two temperatures required to evaluate the heat transfer coefficient at that position.

2.3 Overall Conclusions

The time scale distortion described in Section 2.1.5 leads to lower than expected Nusselt numbers. However, this effect will not be significant during prototypical conditions in the core. During steady state operation the time scale distortion does not exist. Even during accident transients such as loss of forced circulation (LOFC) it is unlikely that there will be a significant effect. This is because the spherical fuel elements cool down very slowly compared to the fluid velocity through the core, despite the fluid being in natural circulation. It could play a role in certain areas outside of the core still in contact with the coolant, especially if active cooling from the pumps is lost.

The key takeaway is that the time distortion is significant enough in fluoride salts with no heating element. This influences the way experiments demonstrating similitude are designed. The experience from the isolated sphere tests were instrumental in designing the heated rod tests.

The heated rods tests showed that there is a good agreement between the Dowtherm A and flinak results for Rayleigh numbers below 10^9. Higher than that there could be distortions related to the natural convection flow being in a transition regime. It is important to investigate and compare the Nusselt numbers at very high Rayleigh numbers above 10^{11}. This would be an unequivocally turbulent flow regime along the heated rod.

3. DETERMINATION OF INTERFACIAL HEAT TRANSFER COEFFICIENTS IN PEBBLE-BED TEST SECTIONS

In this chapter we discuss the importance of the interfacial heat transfer coefficient in a packed bed of spheres in the context of the molten-salt cooled PB-FHR. The interfacial heat transfer coefficient is the convective heat transfer coefficient between the surface of the fuel pebbles and the coolant surrounding it. The term 'solid phase' is used to refer to the pebble fuel, and 'fluid phase' to refer to the coolant. A scaled experiment was designed, fabricated and used to investigate the heat transfer coefficients in the PB-FHR. When discussing the scaled test section, the terms refer to the copper pebbles and the simulant oil respectively. The copper pebbles represent fuel pebbles and the oil the molten fluoride salt coolant. It is crucial to be able to characterize the heat transfer coefficient in the PB-FHR in order to be able to accurately predict the temperature distributions of the solid and fluid phases within the nuclear reactor core. This is required to perform high-fidelity multiphysics simulations of the reactor core. Because the oil experiments are performed at low temperature, thermal radiation effects are reduced compared to the conditions with molten salts, but this scaling distortion can be studied using multiphysics modeling.

As discussed further in Section 3.2, existing convective heat transfer experimental data is severely lacking in the range of Prandtl numbers seen during normal operation and emergency operations of the PB-FHR, although the experimental data used in existing correlations bounds the salt Pr values with lower Pr experiments performed with gases and water, and high Pr experiments performed with mass transfer (where the Schmidt number Sc is large) [49]. Furthermore there is a lack of data at the low Reynolds number regions. It is possible to interpolate to Pr values for molten salts using existing correlations, as detailed in Section 3.2 of this chapter. Data is thus required to verify this at the Pr values for molten salts, and to contribute to the experimental database for FHRs. Here frequency response techniques were used to extract the experimental heat transfer coefficients.

This chapter is split into 4 parts: the objectives and background of the current study, the derivation and assumptions going into the analytical models, the design and construction of the experimental facility, the data reduction methodology, the results and associated discussion, and end the chapter with conclusions from the reported investigation.

3.1 Objectives of Study

This section outlines some of the background theory and describes the problem we aim to investigate. The experimental objectives are defined. We delineate some of the key

assumptions that help in simplifying the governing equations in the scaled experiment. Furthermore, the distortions between the prototypical system and the scaled experiment are also described.

3.1.1 Background and problem definition

In Chapter 1 the governing equations for porous media were introduced and defined. The governing energy equations for the fluid (*f*) and solid (*s*) phases are repeated here Equations (3.1) and (3.2).

$$\varepsilon(\rho c_p)_f \frac{\partial T_f}{\partial t} + \varepsilon(\rho c_p)_f \left[u_r \frac{\partial T_f}{\partial r} + \frac{u_\theta}{r} \frac{\partial T_f}{\partial \theta} + u_z \frac{\partial T_f}{\partial z} \right] = \varepsilon k_f \left[\frac{1}{r} \frac{\partial}{\partial r} \left(r \frac{\partial T_f}{\partial r} \right) + \frac{1}{r^2} \frac{\partial^2 T_f}{\partial \theta^2} + \frac{\partial^2 T_f}{\partial z^2} \right] + \Phi + h_{sf} (T_s - T_f) \tag{3.1}$$

$$(1-\varepsilon)(\rho c_p)_s \frac{\partial T_s}{\partial t} = (1-\varepsilon) k_s \left(\frac{1}{r} \frac{\partial}{\partial r} \left(r \frac{\partial T_s}{\partial r} \right) + \frac{1}{r^2} \frac{\partial^2 T_s}{\partial \theta^2} + \frac{\partial^2 T_s}{\partial z^2} \right) + (1-\varepsilon) q''' + h_{sf} (T_f - T_s) \tag{3.2}$$

The definitions of each of the terms were described in Chapter 1. The interfacial heat transfer coefficient h_{sf} is the local average convective heat transfer coefficient between the solid and fluid phases. In the PB-FHR this would be between the fuel and the salt coolant, in the test section described in Section 3.1.2 it would be between the copper pebbles and the simulant oil. A closure relation for h_{sf} is needed to be able to simultaneously solve Equations (3.1) and (3.2) above. For predicting heat transfer with molten salt and pebble fuel, a correction to h_{sf} to account for thermal radiation augmentation of the heat transfer between the salt and the surface of the fuel pebbles. In this chapter, the convective component of h_{sf} is determined experimentally.

3.1.2 Experimental Objectives

The objectives of the PBHTX facility are outlined in this section. The primary objective is:

- To measure the convective heat transfer coefficient in a pebble bed geometry for a range of Reynolds and Prandtl number that encompass the PB-FHR operating conditions, and compare to correlations in the literature, especially Wakao's correlation [14]. This was done for a heat transfer fluid called Drakesol 260AT, in an experimental facility called the 'Pebble-Bed Heat Transfer Experiment' (PB-HTX). Future work will involve collecting heat transfer data over the same non-dimensional ranges using Dowtherm A. The Handley-Heggs predictive

correlation was considered as well, but rejected as it is included in the Wakao Correlation [50], [51].

The secondary objectives are:

- To measure the friction head loss in the test section geometry
- To measure permeability of the test section and compare to the analytical Carman-Kozeny relationship [15]
- To gain experience designing and developing modular scaled Dowtherm A loops that allow for flexibility in testing
- To use pulsed (binary) and sinusoidal forcing in order to extract thermal inertia information from the collected data (such as time constants)
- To gain experience and understanding in using frequency response techniques to assess fluid-structure interactions in a scaled environment [52]
- To investigate a range of Reynolds and Prandtl numbers outside of the PB-FHR range to add to the experimental database for convective heat transfer with low Reynolds number and high Prandtl number fluids. This is important to further enrich our understanding of convective heat transfer in general packed beds. Some of the previously collected data had large uncertainties associated with them [53] and the experiments here aim to improve on that

3.1.3 Assumptions and key distortions from the prototypical system

It is important to note the distortions between the scaled experiment and the prototypical conditions.

- Radiation heat transfer is neglected in the experiment as it is negligible at the temperatures of scaled oil experiments, and it only accounts for a few percent of the total heat transfer between the pebbles and fluid at the prototypical salt temperatures. Section 3.3.4 discusses the distortions due to thermal radiation in more detail.
- Radial conduction was neglected in the solid phase, and this is a valid assumption as shown experimentally in Section 3.3.2, with a variation of less than one degree centigrade in different radial zones in the test section, as shown in Figure 3-28 and Figure 3-27. The test section was split into 5 axial control volume and temperatures evaluated analytically at the boundaries. In each control volume, the solid phase was assumed to act as a lumped capacitance.
- A uniform temperature was assumed within each individual pebble. This meant that the temperature recorded at the center of the pebble was assumed to be the same at the temperature at the surface. The surface temperature of the pebbles is

needed to extract the heat transfer coefficient. This assumption is valid because the Biot number in individual pebbles is very small (much less than 0.1). This was shown in Chapter 2. There is a distortion with respect to the prototypical conditions, as the PB-FHR fuel pebbles are composed of different layers that have lower thermal conductivities and thus the temperature distribution within each pebble is non-uniform. Section 3.4.5 derives a correction factor that can be implemented in cases of Biot numbers larger than 0.1 in spheres.

- Thermal dispersion and viscous dissipation are neglected as they are small (see Chapter 1 for details on the magnitudes of these terms in the PB-FHR).
- The scaled experiment does not model cross flow, which would be significant in the PB-FHR. As long as the Reynolds number and Prandtl number ranges of the scaled experiment falls within the ranges of prototypical conditions, the experimentally measured heat transfer coefficients will be applicable to prototypical conditions.
- Conduction in the fluid is neglected, thereby simplifying the energy governing equations for the test section.
- Only the axial direction is considered in the test section. For example, the incoming oil temperature is assumed to be uniform as it is expected to be well mixed entering the test section.

3.2 Literature review

Wakao's review paper lists all the experimental data that was collected for heat transfer coefficients in packed beds as a function of Reynolds and Prandtl numbers [14]. The majority of the data was collected for air or water. The range of Reynolds for their proposed correlation was from 15-8500. The experimental data that this correlation was based on were all done with air or other gases, with Prandtl numbers ranging from 0.7 to 1. The correlation proposed by Wakao and Funazkri is widely used in packed bed heat transfer predictions, and is cognate with the correlation they derived using mass transfer data, applying the heat and mass transfer analogy, as well [49]. The mass transfer correlation in a packed bed of spheres was derived using data with a Reynolds number range from 3 to 10,000 (below 3 natural convection may play a significant role) and a Schmidt number range from 0.6 to 70,600. It should be noted that the effect of porosity of the packed bed is not considered in these correlations, although it is unlikely that all the experimental data had the same porosity.

Carillo finds the heat transfer coefficient between oil and a bed of steel spheres, and also studied the effect of porosity on the Nusselt number. They propose correlations for five different porosities for ranges of Reynolds numbers that go from 0.53 up to 412 [54]. Geb et al. flow air through a randomly packed test section of steel pebbles heated via

induction for a range of Reynolds numbers from 20 to 500 [55]. This was done for a non-infinite bed so wall effects played a role in the lower than expected measured Nusselt numbers. Handley and Heggs develop a correlation for heat transfer in fixed packed beds for Reynolds numbers higher than 100 [56]. In the current work, heat transfer coefficient is measured for higher Prandtl numbers, in the range important for heat transfer to molten salts, and a range of Reynolds numbers in an 'infinite' randomly packed pebble bed using oil as the heat transfer fluid.

Most of the work that has been done using frequency response techniques to capture heat transfer data in porous media was carried out in the field of chemical engineering during the 1960s and 1970s, in support of developing packed bed technologies. Littman et al. performed experiments for Reynolds numbers between 2 to 100 to extract gas-particle heat transfer coefficients, for particle sizes ranging from 0.503mm to 2.03mm [57]. For these low Reynolds number tests the effect of thermal dispersion is included, as well as thermal conduction in the axial direction.

Gunn and De Souza looked at Reynolds numbers from 0.05 to 330, also including thermal dispersion effects in to their interpretation models [58]. It is interesting to note that Wakao and Kaguei did not include their data because of the scatter in their original data and the large errors at low Reynolds numbers [23].

Lindauer studied packed and fluidized beds to determine the interfacial heat transfer coefficient between gas (air and helium) and steel, lead and tungsten spheres of diameters ranging from 1mm to 3.175mm [5]. This study differs from the others because they investigated heat transfer coefficients at high Reynolds numbers, up to 18200.

Littman and Barile also studied packed and fluidized beds to determine interfacial heat transfer coefficients between gas and steel spheres of diameters ranging from 0.16mm to 0.72mm. This study was done for Reynolds numbers below 26.

Our study varies from the previous efforts and expands upon them, as well as improving upon them in several key ways:

- PBHTX runs with oil as the heat transfer fluid. Thus we are able to determine heat transfer coefficients at higher Prandtl numbers than previous studies using frequency response techniques. The Prandtl number range in PBHTX is from 10 to 60, whereas previous heat transfer studies were limited to ~0.7 as they all employed gas as the heat transfer fluid.
- Some of the pebbles in the PBHTX test section are instrumented with thermocouples, which means that the temperature of these pebbles can be

monitored and recorded throughout the transient. In previous studies only the fluid temperatures at the inlet and outlet were recorded, and physical models were used to extract what the corresponding heat transfer coefficient was, which means that the accuracy of the experimental heat transfer coefficient was dependent on the accuracy of the model used. We obtain direct temperature measurements of pebbles in PBHTX, which means that we can extract the experimental interfacial heat transfer coefficient directly.

- PBHTX has the capability to study relatively high Reynolds number flows, higher than most of the previous heat transfer studies, of up to 500 in the pebble-bed test section. It should be noted that at the higher Reynolds number flows, thermal dispersion can be neglected.

Given the Reynolds and Prandtl number ranges of the PB-FHR and the PBHTX experiment, the measured Nusselt numbers in PBHTX are expected to follow the Wakao correlation. Discrepancies are discussed in the Results and Discussion section (Section 3.7).

3.3 Frequency Response Tests in Nuclear Reactors

Frequency response tests have been performed in the past to determine stability of a reactor system and to validate theoretical models of it, so their use in nuclear applications is not novel. Tests were done at the Oconee PWR, and reactor power, temperatures and pressures were monitored throughout the test. The fuel temperature coefficient and the heat transfer coefficient from fuel to coolant were determined through these tests [59]. Similar tests were conducted on the MSRE [60]. Chapter 8 of the textbook 'Frequency Response Testing in Nuclear Reactors' provides a summary of early frequency response tests performed on a wide variety of nuclear reactor designs [61]. However, apart from the MSRE no dynamic testing has been done to investigate FHRs, to the knowledge of the author. Showing a successful frequency response test using simulant oils will greatly expand the types of investigations that can be performed in a laboratory. This is one of the goals of the work presented in this chapter. This methodology can be used in the future to better characterize the dynamic response of coolant-boundary structures in the PB-FHR.

3.4 Governing Equations in the Test Section and Analytical Solution

This section outlines the simplified governing energy equations in the test section, shown in Equations (3.3) and (3.7) An analytical solution for the fluid and solid temperatures is determined for the entirety of the test section (as a function of position and time), as well as for the packed-bed entrance.

$$\frac{\partial T_f}{\partial \tau} + u_z \frac{\partial T_f}{\partial z} = \frac{h_{sf} a_v}{\varepsilon(\rho c_p)_f}(T_s - T_f) \tag{3.3}$$

$$\frac{\partial T_s}{\partial \tau} = \frac{h_{sf} a_v}{(1-\varepsilon)(\rho c_p)_s}(T_f - T_s) \tag{3.4}$$

$$T_f(\tau = 0) = T_{f0} \tag{3.5}$$

$$T_s(\tau = 0) = T_{s0} = T_{f0} \tag{3.6}$$

$$T_f(z = 0) = T_{f0} + \Delta T_{f0} \sin(\omega \tau) \tag{3.7}$$

$$a_v = \frac{6(1-\varepsilon)}{d} \tag{3.8}$$

so $a_v = \frac{6(1-0.45)}{0.00635m} = 512 m^{-1}$ in the test section.

$$u_{pore} = \frac{u_z}{\varepsilon}$$

$$u_z = \frac{\mathrm{Re}\,\mu}{\rho D_p} = \frac{500 \times 0.00148 kg m^{-1} s^{-1}}{765 kg m^{-3} \times 0.00635 m} = 0.15 m s^{-1} \tag{3.9}$$

T_f is the fluid temperature, τ the dimensional time, u_z the superficial velocity (the velocity through the test section assuming it is empty), u_{pore} the pore velocity (the fluid velocity in the voids in a filled pebble bed, z the dimensional height of the test section, h_{sf} the interfacial heat transfer coefficient (heat transfer coefficient between the fluid and the solid phases), a_v the specific surface area of the test section calculated in Equation (3.8), ε the porosity, ρc_p the volumetric heat capacity, T_s the solid temperature, which is the temperature of the copper spheres. The subscripts f and s refer to 'fluid' and 'solid' respectively. T_{s0} is the initial temperature of the solid phase, T_{f0} the initial temperature of the fluid phase, ΔT_{f0} the amplitude of the sinusoidal fluctuation of the inlet fluid temperature and ω the frequency of the fluctuation.

The superficial velocity u_z is the nominal velocity at which Reynolds number takes a typical PB-FHR value of 500. u_z was varied in the experiment around this value to study a range of Reynolds numbers.

The porosity is usually assumed to be 0.39, as is the case for tightly packed randomly packed spheres. However the porosity was measured for the test section and that value used, which was 0.45.

In order to make Equations (3.3)-(3.7) non-dimensional, the following substitutions were proposed as shown in Equations (3.12) to (3.18). The non-dimensional fluid and solid temperatures were calculated using the parameters in Table 3-1.

Table 3-1: Typical values of fluid phase and solid phase properties at 80 degC

Property	**Nomenclature**	**Units**	**Value**
Pebble diameter	D_p	m	0.00635
Drakesol 260AT thermal conductivity	k_f	$Wm^{-1}K^{-1}$	0.098
Drakesol 260AT density	ρ_f	kgm^{-3}	765
Drakesol 260AT dynamic viscosity	μ_f	$kg(ms)^{-1}$	0.00148
Drakesol 260AT specific heat capacity	$(c_p)_f$	$J(kgK)^{-1}$	2000
Copper density	ρ_s	kgm^{-3}	8960
Copper specific heat capacity	$(c_p)_s$	$J(kgK)^{-1}$	385
Porosity	ε	dimensionless	0.45
Typical frequency	ω	Hz	0.1

The lower the frequency, the smaller the phase lag between the oil and pebble temperatures, and therefore the smaller the temperature difference between the two. However, the larger the frequency, the less time the fluid has to change temperature, and thus the temperature change would be imperceptible. Additionally, there is a limit to how high the frequency of oscillations is due to the response of apparatus in the experimental facility such as the power supply and the oil heater and due to axial mixing and dispersion of the flow between the heater and the test section. The analytical models developed later in this section are idealistic and assume instantaneous changes in the oil temperature and thus cannot capture this response.

The predictive Wakao correlation is given in Equation (3.10), and a typical interfacial heat transfer coefficient is calculated from it in Equation (3.11), using PBHTX conditions.

$$Nu_{sf} = \frac{h_{sf} D_p}{k_f} = 2 + 1.1 \mathrm{Pr}^{1/3} \mathrm{Re}^{0.6} \tag{3.10}$$

$$h_{sf} = \frac{0.098}{0.00635}(2 + 1.1 \times 27^{1/3} \times 500^{0.6}) = 2200 \, \mathrm{Wm}^2 \, K^{-1} \tag{3.11}$$

Table 3-2: Typical values for the non-dimensional parameters during an experimental run

Non-dimensional Parameter	Typical value	Comments	Equation number
$x = \frac{z}{L}$	Ranges from 0 - 1	Non-dimensionalized to the length of the test section, 0.0889m	(3.12)
$t = \frac{h_{sf} a_v}{(1-\varepsilon)(\rho c_p)_s} \tau$	0.78τ	Non-dimensional time, non-dimensionalized w.r.t. the 'decay constant' of the pebbles	(3.13)
$F = \frac{T_f - T_{f0}}{\Delta T_{f0}}$	Ranges from -1 to 1	Non-dimensional fluid temperature, w.r.t. the temperature difference between the max/min and the mean	(3.14)
$S = \frac{T_s - T_{f0}}{\Delta T_{f0}}$	Ranges from -1 to 1	Non-dimensional fluid temperature, w.r.t. the temperature difference between the max/min and the mean	(3.15)
$\phi = \frac{h_{sf} a_v L}{\varepsilon u_z (\rho c_p)_f}$	0.63	Energy transferred to the fluid phase per unit surface area per unit temperature change	(3.16)
$\sigma = \frac{h_{sf} a_v L}{u_z (1-\varepsilon)(\rho c_p)_s}$	0.24	Energy transferred to the solid phase per unit surface area per unit temperature change	(3.17)
$\eta = \omega \frac{(1-\varepsilon)(\rho c_p)_s}{h_{sf} a_v}$	1.03	Non-dimensional frequency, the inverse of the non-dimensional time term	(3.18)

In equations (3.12) to (3.18), *L* is the height of the packed bed. Typical values of some of the non-dimensional parameters are given in Table 3-2. The values are taken for a Reynolds of 500 through the test section (which is typical for normal operation in the PB-

FHR core) and a Prandtl of 27. This was based on values that were achieved in the PBHTX test section. The interfacial convection heat transfer coefficient was estimated using Wakao's correlation [14]. The fluid properties are taken at 80°C for the Drakesol 260AT simulant oil.

Thus, Equations (3.3) to (3.7) can be written non-dimensionally:

$$\sigma \frac{\partial F}{\partial t} + \frac{\partial F}{\partial x} = \phi(S - F) \tag{3.19}$$

$$\frac{\partial S}{\partial t} = \pi(F - S) \tag{3.20}$$

$$\pi = \frac{1}{(1-\varepsilon)} \tag{3.21}$$

$$F(t = 0) = 0 \tag{3.22}$$

$$S(t = 0) = 0 \tag{3.23}$$

$$F(x = 0) = \sin(\eta t) \tag{3.24}$$

F and *S* are both functions of non-dimensional time and non-dimensional space:

$F(t, x)$

$S(t, x)$

Equations (3.19) to (3.24) can be solved as a function of *t* at *x* = 0, i.e. at the entrance region of the test section. This will allow us to better guess the initial condition for S. Equation (3.24) is substituted into Equation (3.20). Equation (3.25) can then be solved for *S* at *x = 0*, as *S* is only a function of *t*.

$$S_t = \pi(\sin \eta \, t - S) \tag{3.25}$$

To solve for the constant of integration, the initial condition *S* is 0, i.e. Equation (3.23) is used. The integrating factor method was used to solve the ensuing equation, which is shown in Equation (3.26). The general solution at the entrance section is shown in Equation (3.27).

$$\frac{\partial S}{\partial t} + \pi S = \pi \sin \eta t \tag{3.26}$$

$$S = \frac{\pi^2 \sin \eta t - \pi \eta \cos \eta t}{\pi^2 + \eta^2} + \frac{\eta \pi e^{-\pi t}}{\pi^2 + \eta^2} \tag{3.27}$$

As t goes to infinity, the second term of Equation (3.27) drops out and the steady periodic solution remains. This also serves as a boundary condition for S at the entrance of the test section for the full solutions in x and t.

Equations (3.19) and (3.20) can be rewritten in terms of S, the non-dimensional solid temperature. This makes it into the form of a second order PDE with two variables – non-dimensional position x and non-dimensional time t. This is shown in Equation (3.28).

$$\sigma F_t + F_x = \phi(S - F)$$
$$S_t = \pi(F - S)$$
$$F = \frac{1}{\pi} S_t + S$$
$$F_t = \frac{1}{\pi} S_{tt} + S_t$$
$$F_x = \frac{1}{\pi} S_{tx} + S_x$$
$$\frac{\sigma}{\pi} S_{tt} + \frac{1}{\pi} S_{tx} + \left(\sigma + \frac{\phi}{\pi}\right) S_t + S_x = 0 \tag{3.28}$$

This is a wave equation.

$$S(x,t) = X(x)T(t)$$
$$S_x = X'T$$
$$S_t = XT'$$
$$S_{xt} = X'T'$$
$$S_{tt} = XT''$$

$$\frac{\sigma}{\pi} XT'' + \frac{1}{\pi} X'T' + \left(\sigma + \frac{\phi}{\pi}\right) XT' + X'T = 0$$
$$X\left(\frac{\sigma}{\pi} T'' + \left(\sigma + \frac{\phi}{\pi}\right) T'\right) + X'\left(\frac{1}{\pi} T' + T\right) = 0$$
$$\frac{\left(\frac{\sigma}{\pi} T'' + \left(\sigma + \frac{\phi}{\pi}\right) T'\right)}{\frac{1}{\pi} T' + T} = \frac{-X'}{X} = \lambda \tag{3.29}$$

λ is a constant, since both sides of Equation (3.29) are independent of x and t. Thus we are left with two ODEs that can be solved easily.

$$\frac{-X'}{X} = \lambda$$

$$\frac{X'}{X} = -\lambda$$

$$X(x) = C_1 e^{-\lambda x}$$

C_1 is a constant of integration. The left hand side can be solved similarly.

$$\frac{\left(\frac{\sigma}{\pi}T'' + \left(\sigma + \frac{\phi}{\pi}\right)T'\right)}{\frac{1}{\pi}T' + T} = \lambda$$

$$\frac{\sigma}{\pi}T'' + \left(\left(\sigma + \frac{\phi}{\pi}\right) - \frac{\lambda}{\pi}\right)T' + \lambda T = 0$$

To find the roots, assume solutions of the form $T(t) = e^{mt}$.

$$\frac{\sigma}{\pi}m^2 + \left(\left(\sigma + \frac{\phi}{\pi}\right) - \frac{\lambda}{\pi}\right)m + \lambda = 0 \tag{3.30}$$

$$m_1 = \frac{-\left(\left(\sigma + \frac{\phi}{\pi}\right) - \frac{\lambda}{\pi}\right) + \sqrt{\left(\left(\sigma + \frac{\phi}{\pi}\right) - \frac{\lambda}{\pi}\right)^2 - 4\frac{\sigma}{\pi}\lambda}}{2\frac{\sigma}{\pi}}$$

$$m_2 = \frac{-\left(\left(\sigma + \frac{\phi}{\pi}\right) - \frac{\lambda}{\pi}\right) - \sqrt{\left(\left(\sigma + \frac{\phi}{\pi}\right) - \frac{\lambda}{\pi}\right)^2 - 4\frac{\sigma}{\pi}\lambda}}{2\frac{\sigma}{\pi}}$$

$$T(t) = C_2 e^{m_1 t} + C_3 e^{m_2 t}$$

Thus we can determine the form of S, the temperature of the solid phase.

$$S(x,t) = X(x)T(t) = C_1 e^{-\lambda x}(C_2 e^{m_1 t} + C_3 e^{m_2 t})$$

We can consolidate the constants of integration as shown in Equation (3.31).

$$S(x,t) = e^{-\lambda x}(C_4 e^{m_1 t} + C_5 e^{m_2 t}) \tag{3.31}$$

To solve for the constants of integration, the initial conditions are required.

$$S(\mathrm{x} = 0, t = 0) = C_4 + C_5 = 0$$

$$\Rightarrow C_4 = -C_5$$

$$S(x,t) = C_4 e^{-\lambda x}(e^{m_1 t} - e^{m_2 t}) \tag{3.32}$$

At $x = 0,\ S = \frac{\pi^2 \sin \eta t - \pi\eta \cos \eta t}{\pi^2 + \eta^2}$. Substituting this in Equation (3.32) gives the function C_4 as a function of t as shown in Equation (3.33).

$$C_4 = \frac{\pi^2 \sin \eta t - \pi\eta \cos \eta t}{\pi^2 + \eta^2} \frac{1}{(e^{m_1 t} - e^{m_2 t})} \tag{3.33}$$

Therefore it follows that $S(x,t)$ is of the form shown in Equation (3.34).

$$S(x,t) = e^{-\lambda x} \frac{\pi^2 \sin \eta t - \pi\eta \cos \eta t}{\pi^2 + \eta^2} \tag{3.34}$$

Using the solution for S, the solution of F can also be derived using Equation (3.20). This was done using Mathematica version 10.3 and the solution is given in Equation (3.35).

$$F(x,t) = \frac{1}{\pi} \frac{\eta\pi(\pi \cos \eta t + \eta \sin \eta \,\mathrm{t})}{\pi^2 + \eta^2} + e^{-\lambda x} \frac{\pi^2 \sin \eta t - \pi\eta \cos \eta t}{\pi^2 + \eta^2}$$

$$F(x,t) = \frac{\eta\pi \cos \eta t + \eta^2 \sin \eta \,\mathrm{t}}{\pi^2 + \eta^2} + e^{-\lambda x} \frac{\pi^2 \sin \eta t - \pi\eta \cos \eta t}{\pi^2 + \eta^2} \tag{3.35}$$

At $x=0$, $F(x,t)$ reduces to $\sin \eta t$ which is the boundary condition at the entrance. The solutions for F and S were input into Equation (3.19) to check their correctness. This was done using Wolfram Mathematica version 10.3.

Equation (3.34) can be rewritten in terms of a phase shift term, as shown in Equation (3.36) below. $\tan^{-1}\frac{\eta}{\pi}$ is the phase lag.

$$S(x,t) = e^{-\lambda x} \frac{\pi^2}{\pi^2 + \eta^2} \left[\sqrt{\left(\pi^2 + \eta^2\right)} \sin\left(\eta t - \tan^{-1} \frac{\eta}{\pi} \right) \right] \tag{3.36}$$

3.4.1 The constant λ

It is important to understand the significance of the constant λ that was introduced in Equation (3.29) to solve the PDE. Equation (3.30) shows m in terms of non-dimensional parameters and the integration constant λ. In order to have real solutions (which is necessary given that the PDEs describe an experimental setup), the determinant must be greater than or equal to 0. This condition provides bounds for the value of λ. The determinant is repeated in Equation (3.37).

$$\left(\left(\sigma + \frac{\phi}{\pi} \right) - \frac{\lambda}{\pi} \right)^2 - 4\frac{\sigma}{\pi}\lambda \geq 0$$

$$\Rightarrow \left(\sigma+\frac{\phi}{\pi}\right)^2-2\left(\sigma+\frac{\phi}{\pi}\right)\frac{\lambda}{\pi}+\left(\frac{\lambda}{\pi}\right)^2-4\frac{\sigma}{\pi}\lambda\geq 0$$

$$\Rightarrow \frac{\lambda^2}{\pi^2}-\lambda\left(\frac{2}{\pi}\left(\sigma+\frac{\phi}{\pi}\right)+4\frac{\sigma}{\pi}\right)+\left(\sigma+\frac{\phi}{\pi}\right)^2\geq 0 \tag{3.37}$$

Solve for λ using the quadratic equation:

$$\lambda=\frac{\left(\frac{2}{\pi}\left(\sigma+\frac{\phi}{\pi}\right)+4\frac{\sigma}{\pi}\right)\pm\sqrt{\left(\frac{2}{\pi}\left(\sigma+\frac{\phi}{\pi}\right)+4\frac{\sigma}{\pi}\right)^2-\frac{4}{\pi^2}\left(\sigma+\frac{\phi}{\pi}\right)^2}}{\frac{2}{\pi^2}} \tag{3.38}$$

It is apparent that λ has real solutions when the determinant D in Equation (3.38) is 0 or positive. By expanding the determinant, it can be shown that the determinant has to be positive, and therefore λ and m are both real.

$$\left(\frac{2}{\pi}\left(\sigma+\frac{\phi}{\pi}\right)+4\frac{\sigma}{\pi}\right)^2-\frac{4}{\pi^2}\left(\sigma+\frac{\phi}{\pi}\right)^2$$

$$\Rightarrow \left(\frac{2}{\pi}\right)^2\left(\sigma+\frac{\phi}{\pi}\right)^2+16\left(\frac{\sigma}{\pi}\right)^2+\frac{16\sigma}{\pi^2}\left(\sigma+\frac{\phi}{\pi}\right)-\frac{4}{\pi^2}\left(\sigma+\frac{\phi}{\pi}\right)^2 \tag{3.39}$$

$$\Rightarrow \frac{16\sigma}{\pi^2}(2\sigma+\phi)$$

Equation (3.39) is always positive because the non-dimensional parameters are positive.

Based on the typical values of the non-dimensional parameters given in Table 3-2, there are two possibilities for the value of λ as shown in Table 3-3. It is apparent that λ needs to be positive because of the exponential term in S and F, which has a negative sign in front of the λ. The exponential term implies that the amplitude of the temperature fluctuations of the solid and fluid phase decrease along the x axis (up through the test section). A λ of 2.4 would suggest a steeper temperature drop in the test section compared to a λ of 0.15. The correct value for λ is made clearer with experimental data. The experimental data currently shows that the amplitudes of the temperature fluctuations of the solid phase do not change much in the x axis, but that the fluid temperature fluctuation drops quite a bit between the entrance and exit (this discrepancy is shown and explained more in Section 3.3.1). Therefore it is more likely that λ is in between the two values, and closer to 2.4. The lower the λ, the less the temperatures vary in the x axis. The graphs show a constant temperature difference between the fluid and solid phases throughout the test section, and this is explained further in 3.3.1.

Table 3-3: Two possibilities for λ according to the quadratic equation in Equation (3.38)

Λ	2.4	0.15

3.4.2 Non-dimensional pre-predictions

Graphs of the non-dimensional solid and fluid phase temperature variations are shown in Figure 3-1 and Figure 3-2. The first set of graphs is for λ = 2.4 and the second for λ = 0.15. It can be seen that in Figure 3-1 the magnitudes of F and S vary with axial position, implying smaller amplitudes nearer the exit of the test section. In Figure 3-2 there is a very slight decrease in magnitude as a function of axial direction. This is because the 'damping factor' λ is larger in Figure 3-1 than in Figure 3-2 In all cases, the blue line signifies the non-dimensional fluid temperature F and the gold line the non-dimensional solid temperature S. The abscissa is non-dimensional time and the ordinate non-dimensional temperature.

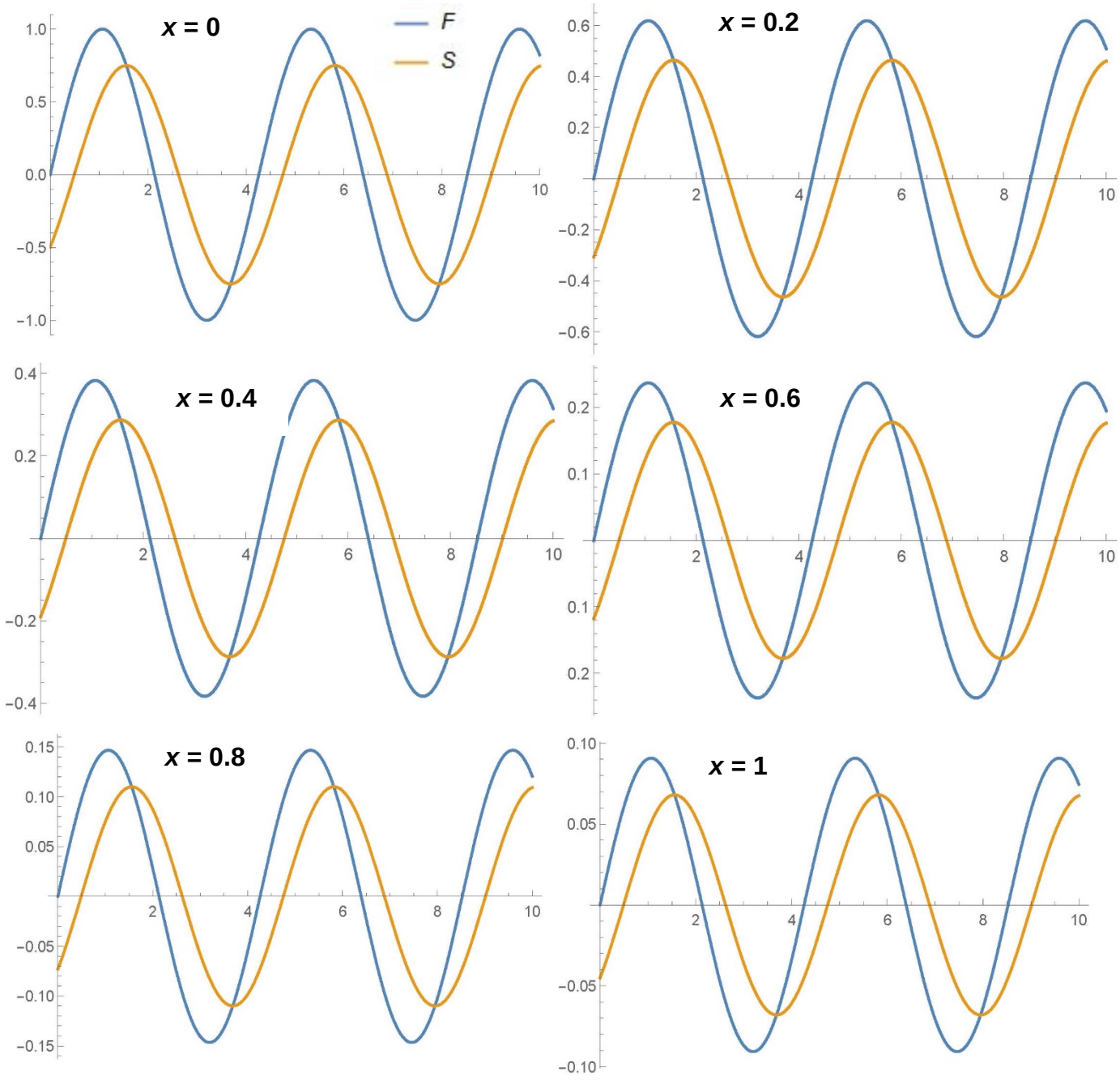

Figure 3-1: Non-dimensional solid and fluid phase temperatures against non-dimensional time for lambda = 2.4. The graphs are for varying x positions. From left to right, x=0, x=0.2, x=0.4, x=0.6, x=0.8 and x=1

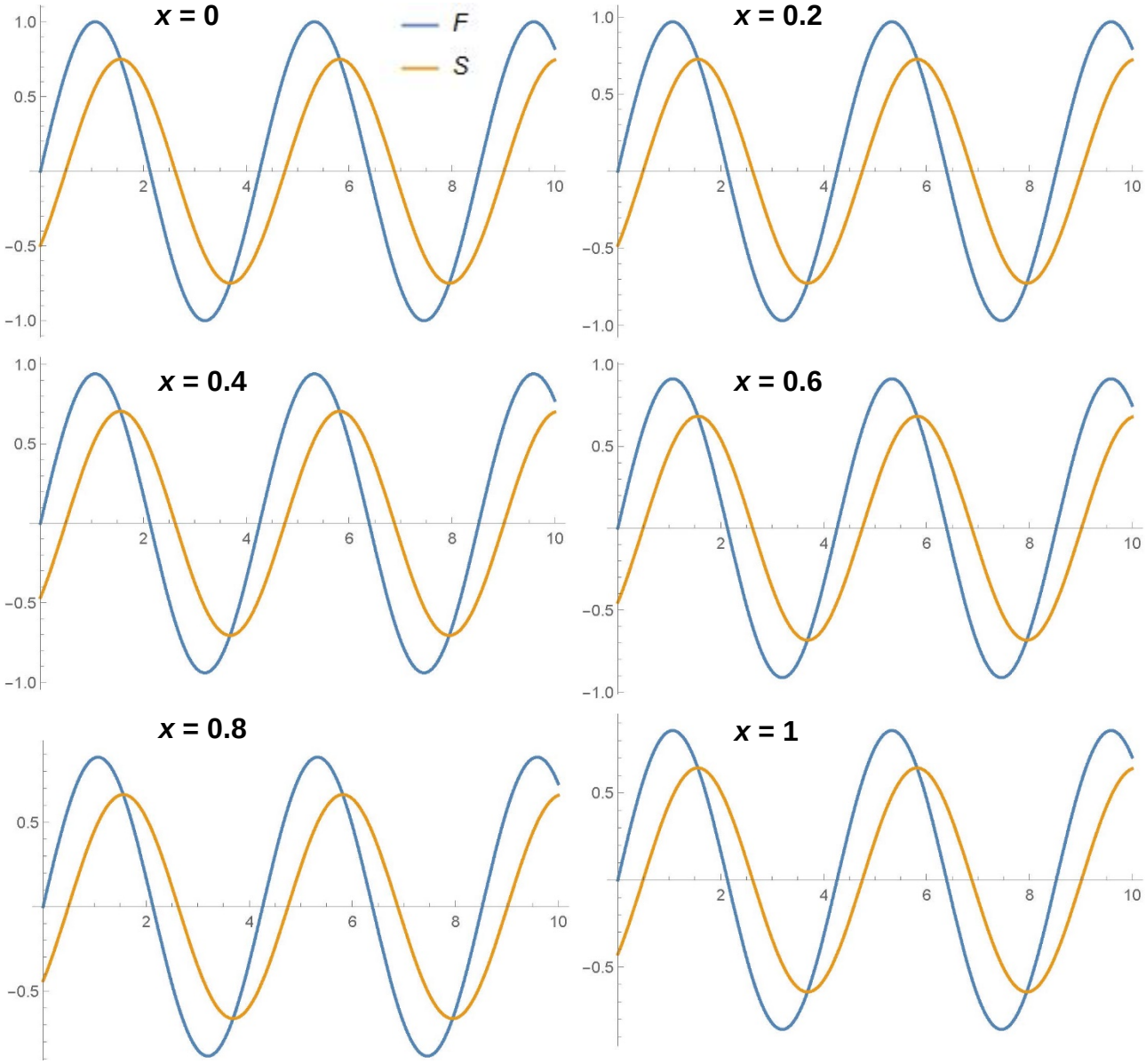

Figure 3-2: Non-dimensional solid and fluid phase temperatures against non-dimensional time for lambda = 0.15. The graphs are for varying x positions. From left to right, x=0, x=0.2, x=0.4, x=0.6, x=0.8 and x=1

3.4.3 Fully developed flow in the test section

As the temperature of the spheres in the pebble bed is never constant (due to the oscillating heater power), the thickness of the thermal boundary layer is continually changing. The question becomes whether we can assume that at a single point in time we have quasi-steady state conditions or not. Therefore the time it takes for the boundary

layer thickness to change should be much larger than the other time scale of interest, which is the fluid transit time in the test section. This way it can be assumed that the thermal boundary layer forming around the pebbles is 'stationary' with respect to time in comparison to the time it takes for the fluid temperature to change.

Under typical operating conditions in PBHTX the residence time of the oil within the test section is much smaller than the period of oscillation of the oil temperature. This means that the oil temperature at the outlet is not affected by the heater power oscillations and any variations in the oil outlet temperature are due to heat transfer between the pebbles and the fluid. Additionally, even though the heater power (heating the oil) is sinusoidally oscillating, the oil going into the heater will be at the cold temperature.

Estimates for the period and the residence time are given in Equations (3.40) to (3.42). These were based on typical values that would be seen during an experimental run. The residence time was based on the flow rate necessary for a Reynolds number of 500 in the test section. The period is an experimental variable, and the smaller it is the larger the temperature difference between the pebbles and the oil.

$$\tau_{period} = \frac{1}{\omega} = \frac{1}{0.1 s^{-1}} = 10 s \tag{3.40}$$

$$\tau_{residence} = \frac{V}{Q} = \frac{1.39 \times 10^{-4} m^3}{2.32 \times 10^{-4} m^3 / s} = 0.6 s \tag{3.41}$$

$$\tau_{residence} = \frac{L}{u_z} = \frac{0.0889 m}{0.15 s} = 0.6 s \tag{3.42}$$

In Equations (3.40) and (3.41), ω is the frequency of oscillations in rad/s, V is the volume of pore space in the test section in m^3 and Q is the flow rate through the test section in m^3/s assuming a Reynolds number of about 500.

3.4.4 The assumption of quasi-steady state conditions in the test section

Although this experiment is a transient study, quasi-steady state conditions can be assumed. The ratio of the volumetric heat capacity between the fluid and solid phases is an indicator for whether quasi-steady conditions may be assumed. Figure 2-14 shows the volumetric heat capacities of the copper pebbles and the Drakesol 260AT oil. The ratio of $(\rho c_p)_f / (\rho c_p)_s$ is 0.44 (Table 3-4) which implies that the temperature of the solid changes more slowly than the fluid temperature. This suggests that distortions due to transient effects are unlikely. It should be noted that the measured heat transfer coefficients are

being compared to the Wakao correlation that included data from step response, pulse response and frequency response tests. The mass transfer correlation included data from evaporation and sublimation tests, which implies steady state conditions.

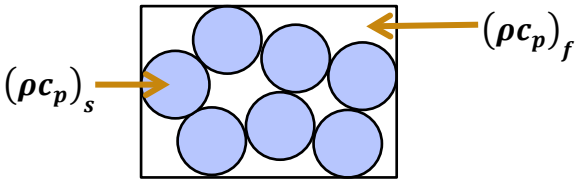

Figure 3-3: Diagram of pebbles and oil (solid and fluid phases)

Table 3-4: Volumetric heat capacity ratio between Drakesol 260AT, heat transfer fluid in PBHTX, and copper, the material of the pebbles in the test section.

	Fluid temperature (°C)	$(\rho c_p)_f / (\rho c_p)_s$	**Reference for material properties**
Drakesol 260AT to copper	80	$1.53 \times 10^6 / 3.5 \times 10^6 = 0.44$	Drakesol 260AT: [62] Copper: [38]

3.4.5 Biot Number Approximation

Analysis from Chapter 2 shows that an isolated copper sphere in Dowtherm A has a small enough Biot number that it can be treated as a lumped capacitance mass. The thermocouples are glued with high thermal conductivity epoxy into holes drilled into the center of selected copper spheres. The small Biot number implies a uniform temperature distribution within a single pebble, meaning that the temperature at the surface is about the same as the recorded temperature in the center. This would be the case with the Drakesol 260AT oil as well.

The Biot number in a graphite pebble is on the order of unity (as shown in Chapter 2). In the PB-FHR core, there are inert graphite pebbles along its edges. To quantify the effects of non-uniform temperature distribution in the sphere a correction can be calculated by assuming a parabolic temperature distribution in the sphere, and applying the integral method to calculate a correction for non-uniform temperature.

The non-dimensionalization of the radius, temperatures and time is as shown in Equations (3.43) to (3.47). r' is the non-dimensional radius, r the radial co-ordinate of the sphere, R the actual radius of the sphere, T_i the initial sphere temperature, θ the non-dimensional temperature, t' the non-dimensional time, non-dimensionalized using the

temperature decay constant of an isolated sphere. The subscripts *s* and *f* refer to 'solid' and 'fluid' as before.

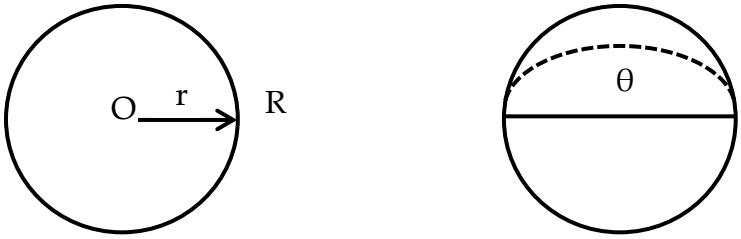

Figure 3-4: Diagram of the assumed temperature distribution in an isolated sphere in which the Biot number is larger than 0.1

$$r' = \frac{r}{R} \tag{3.43}$$

$$\theta = \frac{T - T_f}{T_i - T_f} \tag{3.44}$$

$$\theta_{av} = \frac{T_{av} - T_f}{T_i - T_f} \tag{3.45}$$

$$Bi = \frac{h_{sf} R}{k_f} \tag{3.46}$$

$$t' = \frac{t}{\left(\rho c_p\right)_s R \Big/ 3h_{sf}} \tag{3.47}$$

The shape of non-dimensional temperature was assumed to be a parabola as shown in Figure 3-4:

$$\theta = C - Dr'^2 \tag{3.48}$$

C and *D* are functions of time. The integral method solves to find functions for *C*(*t*) and *D*(*t*) that satisfy an integral energy balance for the sphere, and the conduction boundary condition at the surface of the sphere.

Transient lumped capacitance solution is given in (3.51), solved using (3.50) which was non-dimensionalized using (3.49).

$$\rho c_p \frac{4}{3}\pi R^3 \frac{dT_{av}}{dt} = -4\pi R^2 h(T_{av} - T_\infty)\Big|_{r=R} \tag{3.49}$$

$$\frac{d\theta_{av}}{dt'} = \theta_{av} \tag{3.50}$$

$$\theta_{av} = A\exp(-t') \tag{3.51}$$

At the surface of the pebble, the heat transfer is given by Equation (3.52) and non-dimensionalized before being solved.

$$-k_f \left.\frac{\partial T}{\partial r}\right|_{r=R} = h_{sf}\,(T - T_\infty)\Big|_{r=R} \tag{3.52}$$

$$-\frac{k_f}{R}\left.\frac{\partial \theta}{\partial r'}\right|_{r'=1} = h_{sf}\,\theta\big|_{r'=1}$$

$$-\left.\frac{\partial \theta}{\partial r'}\right|_{r'=1} = \left.\frac{h_{sf}R}{k_f}\theta\right|_{r'=1}$$

$$-\left.\frac{\partial \theta}{\partial r'}\right|_{r'=1} = Bi\theta\big|_{r'=1}$$

$$\Rightarrow 2D = Bi(C - D)$$

$$\Rightarrow \frac{2D}{Bi} = (C - D)$$

$$\Rightarrow C = D\left(\frac{2}{Bi} + 1\right)$$

$$\theta = D\left(\frac{2}{Bi} + 1\right) - Dr'^2$$

$$\theta = D\left(\frac{2}{Bi} + 1 - r'^2\right)$$

where $D(t')$ is a function of time

$$\theta_{av} = \frac{\int_0^1 r'^2\,\theta\,dr'}{\int_0^1 r'^2\,dr'}$$

$$\theta_{av} = \frac{\int_0^1 r'^2\,D\left(\frac{2}{Bi} + 1 - r'^2\right)dr'}{\int_0^1 r'^2\,dr'}$$

$$\theta_{av} = \frac{D\left[\frac{2}{Bi}\frac{r'^3}{3} + \frac{r'^3}{3} - \frac{r'^5}{5}\right]_0^1}{\left[\frac{r'^3}{3}\right]_0^1}$$

$$\theta_{av} = D\left(\frac{2}{Bi}+\frac{2}{5}\right)$$

The energy balance between the convection heat transfer and the internal heat generation in a sphere is used to solve for the non-dimensional time.

$$\frac{\rho c_p R}{3h}\frac{\partial T_{av}}{\partial t} = -(T - T_\infty)\Big|_{r'=1}$$

$$\frac{d\theta_{av}}{dt'} = -\theta\Big|_{r'=1}$$

$$t' = \frac{t}{\rho c_p R / 3h}$$

$$\left(\frac{2}{Bi}+\frac{2}{5}\right)\frac{dD}{dt'} = -\frac{2D}{Bi}$$

$$\frac{dD}{dt'} = -\frac{5D}{5+Bi}$$

$$D = A\exp\left(\frac{-5}{5+Bi}t'\right)$$

$$\theta_{av} = D\left(\frac{2}{Bi}+\frac{2}{5}\right)$$

$$\theta_{av} = \left[A\exp\left(\frac{-5}{5+Bi}t'\right)\right]\left(\frac{2}{Bi}+\frac{2}{5}\right)$$

$$t' = 0 \Rightarrow \theta_{av} = 1$$

$$A = \left(\frac{2}{Bi}+\frac{2}{5}\right)^{-1}$$

$$\theta_{av} = \exp\left(\frac{-t'}{1+Bi/5}\right) \qquad (3.53)$$

Equation (3.53) is compared to Equation (3.51), which assumes that the temperature is constant inside the sphere.

$$\theta_{av} = \exp(-t')$$

Equation (3.53) shows that for Bi<<1 the correction factor is approaches zero. As Biot approaches unity the average non-dimensional temperature in the sphere is overestimated if the correction factor is ignored.

3.5 Experimental Methodology

The first set of experiments that were conducted at UCB to measure heat transfer coefficients for PB-FHR operating conditions used step change response in the pebble-bed test section. The pebbles were heated to the required temperature and then cold fluid was routed into the test section, causing a rapid response from the pebbles, and this

transient was recorded. The results from these experiments suggested that further data was required in order to confirm or refute that existing correlations such as the Wakao correlation could be used for the PB-FHR [63]. With the step change methodology data could only be collected for as long as the transient lasted, which was on the order of 1 second. This work was the precursor to the design and construction of PBHTX.

There are several advantages to using pulsed or sinusoidal forcing to measure heat transfer coefficients, as opposed to step change responses.

- In the data reduction procedure, the interfacial heat transfer coefficient is a function of the derivative of the pebble temperature T_s. With an oscillatory temperature variation in the pebble temperatures, the derivative can be easily obtained to a higher accuracy than could be done for the step change responses.
- With an oscillatory forcing function it is possible to achieve a higher temperature difference between the pebbles and the fluid in the test section.
- More data can be collected over a longer interval of time when periodic steady state conditions are achieved. This would help reduce any potential distortions due to transient effects.
- Accurate measurements of thermal inertia of the test section can be made with frequency response data.

With PBHTX we can exercise more control over the minimum and maximum temperatures of the fluid. This is because a larger power to the heater can be achieved. A larger temperature difference between the pebbles and oil can be obtained than was possible during the step change response tests. In this way data can be collected for a larger range of non-dimensional numbers. In the following set of tests, sinusoidal oscillations in the inlet fluid temperature were achieved by controlling the power supply to the heater using LabView. The lessons learned from this experience will be vital to performing similar experiments on larger integrated effects test (IET) facilities such as CIET [64].

Periodic pulsed power tests are also equally powerful in terms of extracting data to measure heat transfer coefficients. The results presented in this chapter were all collected from pulsed tests. The heater is manually turned off and on at regular intervals via the DC power supply. This directly affects the temperature of the fluid exiting the heater. With period pulsing, the minimum heat input is 0 and the maximum is as specified. The higher the maximum heater power, the larger the potential temperature difference between the pebbles and the fluid (for a given frequency of pulsing). With a pure sinusoidal forcing function the overall difference between the maximum and minimum

power levels will be less than it is for the periodic pulsed function. With the pulsed function however, the heater is more susceptible to damage due to the rapid transients.

A periodic pulsed function will generally be composed of a sum of sinusoidal waves. Their frequencies and amplitudes can be extracted using fast Fourier transforms (FFT), as is shown in Section 3.3.1. Therefore several frequency responses could potentially be extracted from one periodic pulsed test. For the purpose of measuring convective heat transfer coefficients however, only the amplitudes of the temperature fluctuation of the oil and pebbles are needed. Periodic pulsed tests could be a simple way to extract thermal inertia (such as time constants) data from an experimental system, given that the programming the input is very straightforward compared to for a sinusoidal input.

In Chapter 3 of Kerlin's textbook on *Frequency Response Testing in Nuclear Reactors* [61], the different types of input signals are described in the context of reactor inputs (i.e. through reactivity perturbations using the control rods). It is important to note that what Kerlin describes as a 'pulsed test' is different to the input signal described in this chapter. Kerlin's 'pulsed test' is a non-periodic input in which the system is pulsed once and the response monitored. We differentiate from those tests by referring to 'periodic pulsed' tests, which are similar to 'square waves' as Kerlin describes them, with a 50% duty cycle. This means that the time for which the signal is 'on' (high power) is equal to time for which the signal is 'off' (zero power).

3.5.1 Description of the PBHTX facility

The Pebble-Bed Heat Transfer Experiment (PBHTX) is a separate effects test facility designed to measure convective heat transfer coefficients in a randomly packed pebble-bed test section. This can be done for a range of Reynolds and Prandtl numbers, which encompass the values expected in PB-FHR reactor cores. Typical values for the non-dimensional numbers ranges in the PB-FHR are given in Table 3-5, and as shown in Chapter 1 and repeated here.

Table 3-5: Typical non-dimensional numbers in the PB-FHR pebble-bed core

	Reynolds in the core	**Prandtl in the core**
Forced circulation (full power)	500-1000	12-19
Natural circulation	10-20	12-19

A diagram of the flow schematic in the loop is given in Figure 3-5, with the direction of flow following the arrows depicted. The labels beginning with T refer to thermocouple locations in the tank and the test section. The labels beginning with BT refer to bulk temperature thermocouples located throughout the loop. WT refers to 'wall' temperature locations, which means the temperature of the fluid near the wall. It is important to measure both at a particular location to ensure that the fluid is well mixed. The label M refers to the location of a manometer line, used to measure head at that location. Figure 3-6 and Figure 3-7 show the as-built facility.

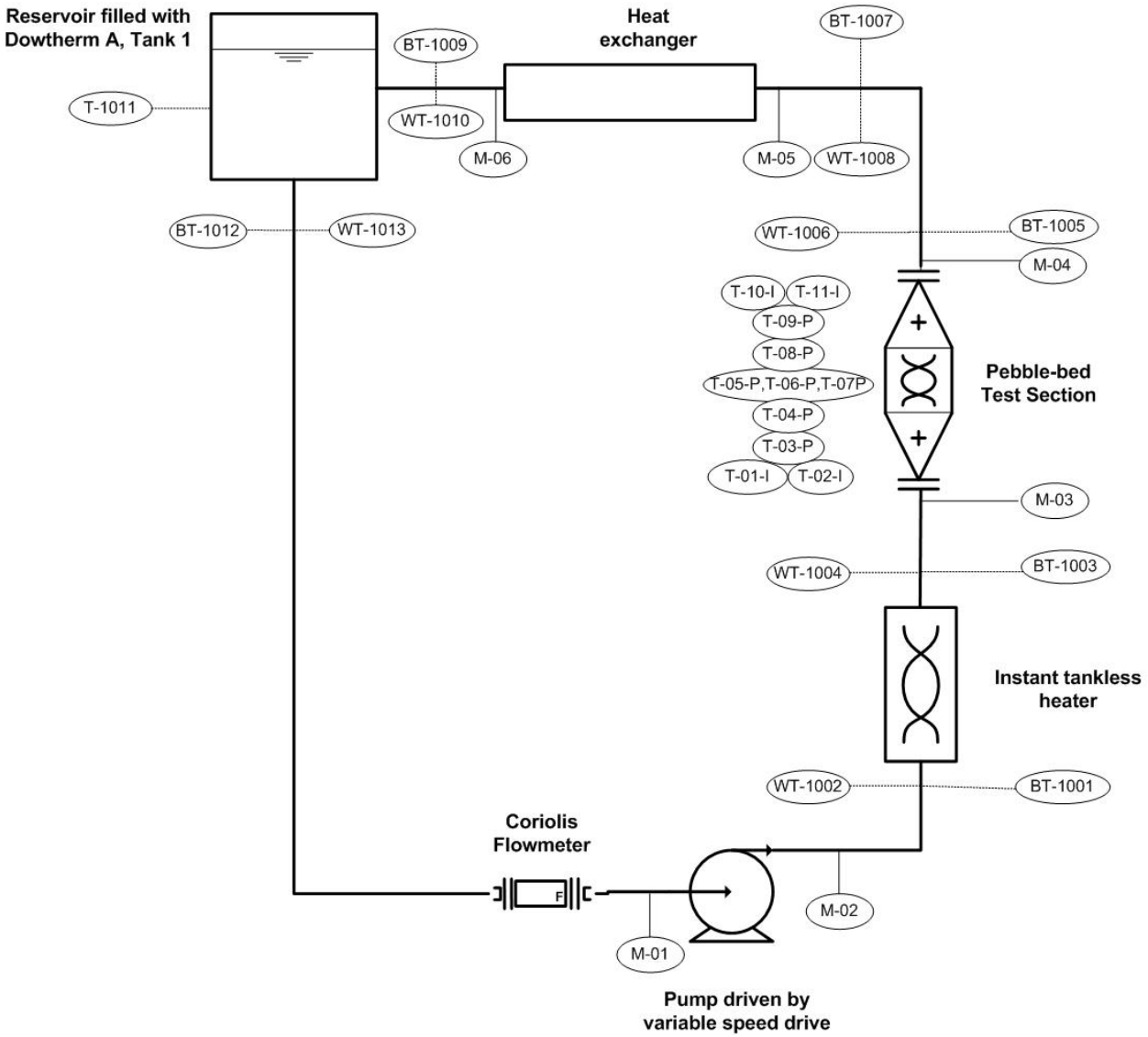

Figure 3-5: Flow schematic of PBHTX, with unidirectional flow in the direction of the arrow

The Reynolds and Prandtl numbers as defined for PBHTX are given in Equations (3.54) and (3.55).

$$\mathrm{Re} = \frac{u_z D_p}{\nu} \tag{3.54}$$

$$\mathrm{Pr} = \frac{\nu}{\alpha} \tag{3.55}$$

The superficial velocity u_z is defined as the velocity through an empty pebble-bed in m/s, the diameter D_p refers to the pebble diameter in m, and the fluid properties ν and α refer to the kinematic viscosity (in units of m^2/s) and thermal diffusivity (in units of m^2/s) taken at film temperatures, which is defined in Equation (3.56),

$$T_{film} = \frac{T_s + T_f}{2} \tag{3.56}$$

T_s is the temperature of the pebble ('solid' phase) and T_f the oil temperature ('fluid' phase).

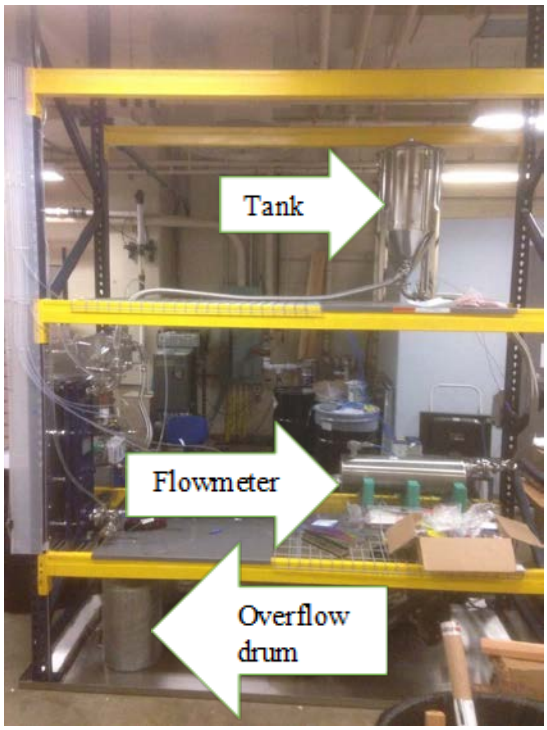

Figure 3-6: PBHTX view from the North showing the tank, flowmeter and overflow drum

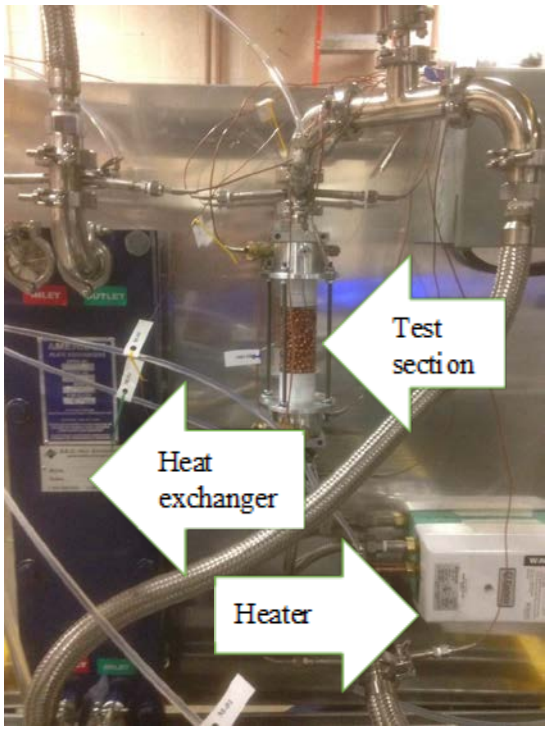

Figure 3-7: View from the West showing the heater, test section and heat exchanger

3.5.2 Apparatus and Components

This section describes the components that were used to build the PBHTX flow loop and explains why they were chosen.

Pump

A 0.25 kW (0.33 horsepower) centrifugal pump is used to force flow through the loop. At a flow rate of 38 liters per minute (10 gpm), the pump can provide 10 meters of head. With Drakesol 260AT as the working fluid, a flow rate of 23.6 lpm is needed to get a Reynolds number of 1000 in the test section. The pump is connected to a variable speed drive (VFD) to control the pump speed and thus the flow rate.

Heater and Power Supply

An instantaneous water heater (EEMAX EX95DL) [65] is used to heat the incoming oil. The heater is controlled via a 10 kW DC power supply (TDK Lambda Genesys). The power supplied to the heater can be varied using current or voltage. The maximum current is 40A and the maximum voltage is 250V. This particular heater was chosen because of its compactness and small thermal inertia. The design of this heater is such that the heating element can be easily inspected and replaced if necessary (for example, due to fouling). Given that the volumetric heat capacity of the Drakesol 260AT oil is about one-third that of water, it is possible to increase the temperature of the incoming oil to much higher than specified.

Figure 3-8 shows the plastic insert that goes into the heater, and the coiled wire heating element that wraps around it. The heating element was directly connected to the DC power supply using electrodes and cables. The heating element is easily replaceable.

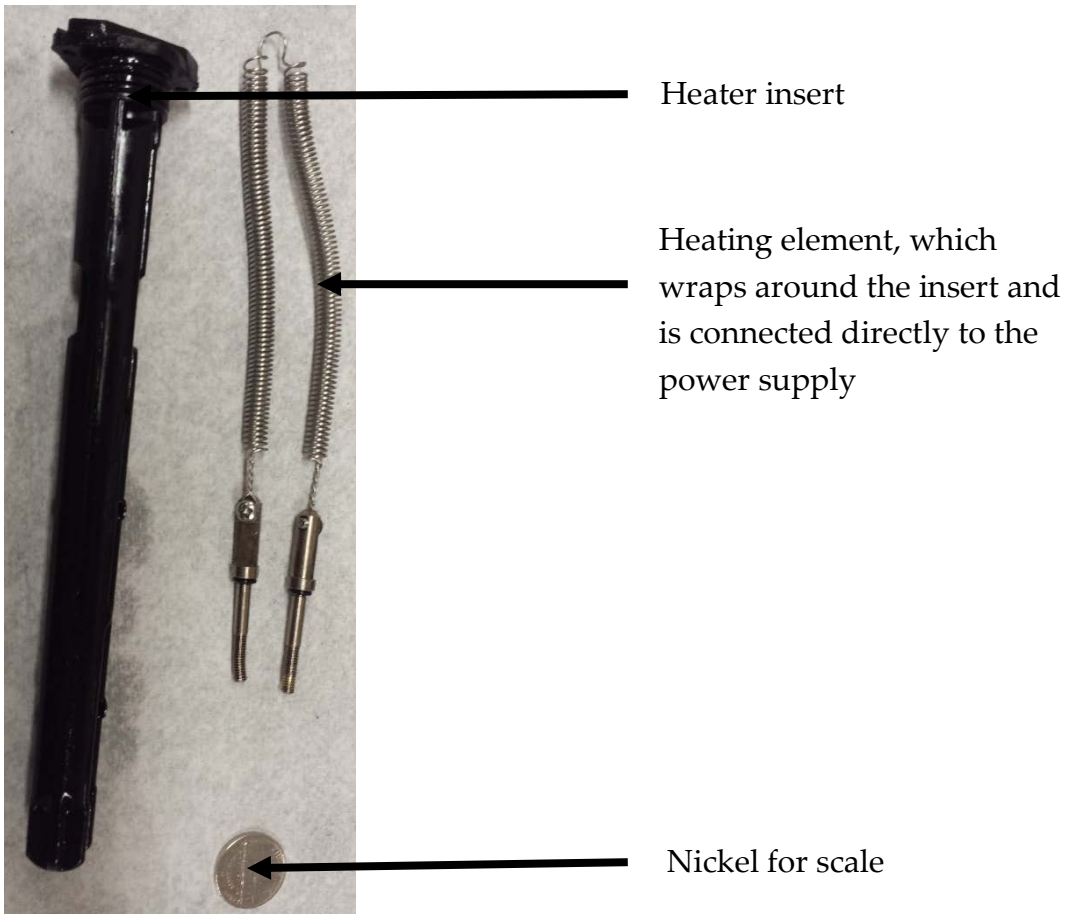

Figure 3-8: Heating element with the heater insert. The heating element is made of nichrome wire.

If the Drakesol 260AT oil is kept in prolonged contact with the heater however, it corrodes the casing around the heating element as show in Figure 3-9 and Figure 3-10. The heater insert from Figure 3-8 is shown in Figure 3-9 and Figure 3-10. The corrosion issue was curbed by draining the loop after each experimental run. The casing is made of Udel, a fiberglass reinforced thermoplastic polymer. If Dowtherm A is to be used in future experiments it is important to fabricate an alternative housing out of Teflon to reduce plastic/oil compatibility issues.

Figure 3-9: Heater internals, cut open to show after degradation in caused by contact with the oil Drakesol 260AT

Figure 3-10: Close-up of material degradation from contact with medium-temperature oil

Heat Exchanger

An Ameridex plate-and-frame heat exchanger (AMDX-10-8) is used to cool the hot oil to the lower temperature. The secondary fluid is water. The water supply through the heat exchanger is controlled using a ball valve. The heat exchanger is rated to transfer a maximum of 10kW of heat. Viton gaskets are used between the heat exchanger plates due to their compatibility with Dowtherm A. A plate-and-frame heat exchanger was chosen for this application because of its compactness given the amount of heat it can transfer, and because of the ease with which they can be taken apart for inspection or cleaning. This is especially useful when Drakesol 260AT is the heat transfer fluid, as it has a tendency to cause fouling at continued high temperatures operating.

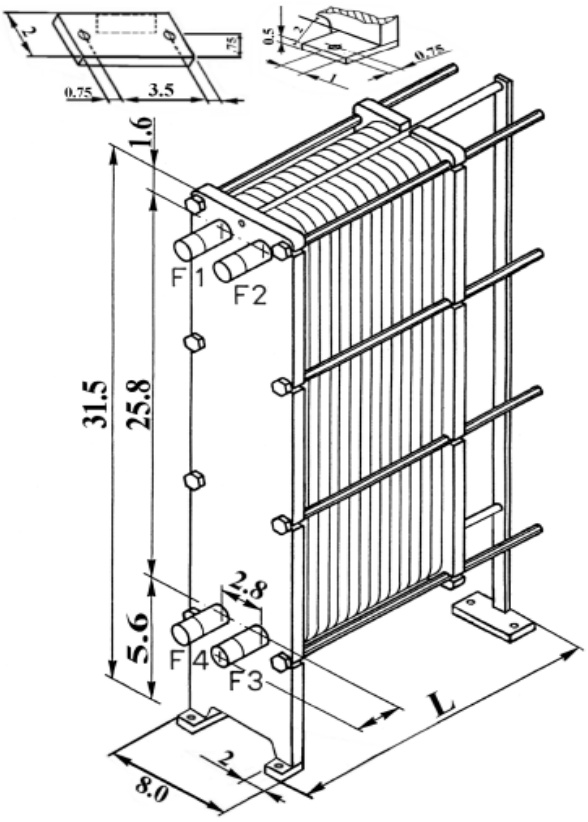

Figure 3-11: Schematic of plate-and-frame heat exchanger, with dimensions in inches
[79]

Tank

The purpose of the tank is to store a large quantity of the oil at the cold fluid temperature. A pipe was welded to the inlet of the tank as shown in Figure 3-12. This was done to ensure that the incoming fluid is well mixed when it re-enters the tank. The tank is a stainless steel conical fermenter that can hold up to 53 liters (14 gallons).

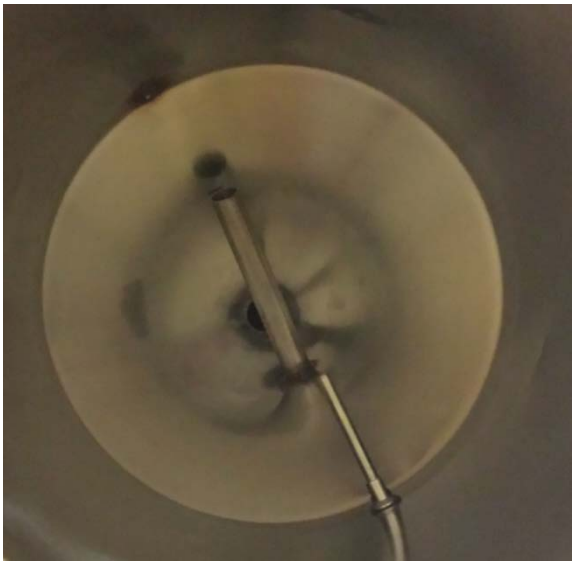

Figure 3-12: Inside of the tank, with an incoming pipe

Piping

In most parts of the experimental facility, flexible stainless steel tubing of 1.5" diameter was used to connect the apparatus together as shown in Figure 3-13. Stainless steel tri-clamp fittings were used to connect pipes to each other. Teflon gaskets were used between the tubing, as Teflon has good chemical compatibility with Dowtherm A [66]. It was found that these tri-clamp fittings were extremely leak resistant, and so far no leaks have been reported in PBHTX from these types of fittings. Pipes carrying heated oil were not insulated as the only the test section portion is of interest. The pipes were not hot enough to be a personnel safety hazard.

It was found that using triclamp fittings reduced the amount of leakage and air entrainment in the loop significantly compared to previously constructed flow loops that had brazed copper joints. Additionally, using this type of fitting makes it easier to alter or upgrade the loop.

Figure 3-13: Tri-clamp fittings from the pump discharge to the flexible stainless steel tubing going to the heater

Heat transfer fluid

Two fluids have been identified for this experiment: Drakesol 260AT and Dowtherm A. Both these fluids match the Prandtl number of flibe at temperatures lower than the PB-FHR operational temperatures, as shown in Figure 3-14 and Figure 3-15. With Drakesol 260AT, a Prandtl number of 15 is achieved at a temperature of around 120 °C. Dowtherm A has a Prandtl number of 15 at around 70°C.

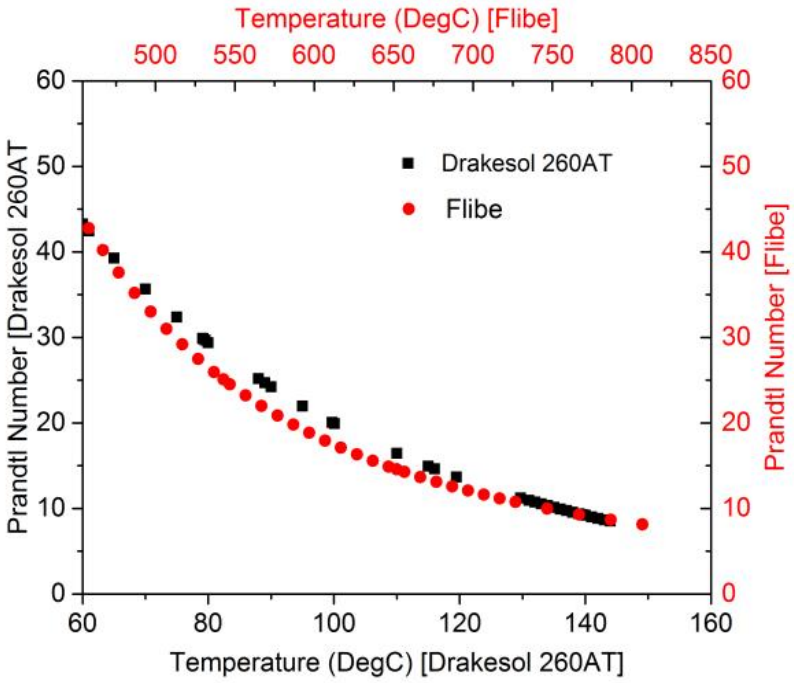

Figure 3-14: Prandtl number comparison of the simulant oil Drakesol 260AT and Flibe

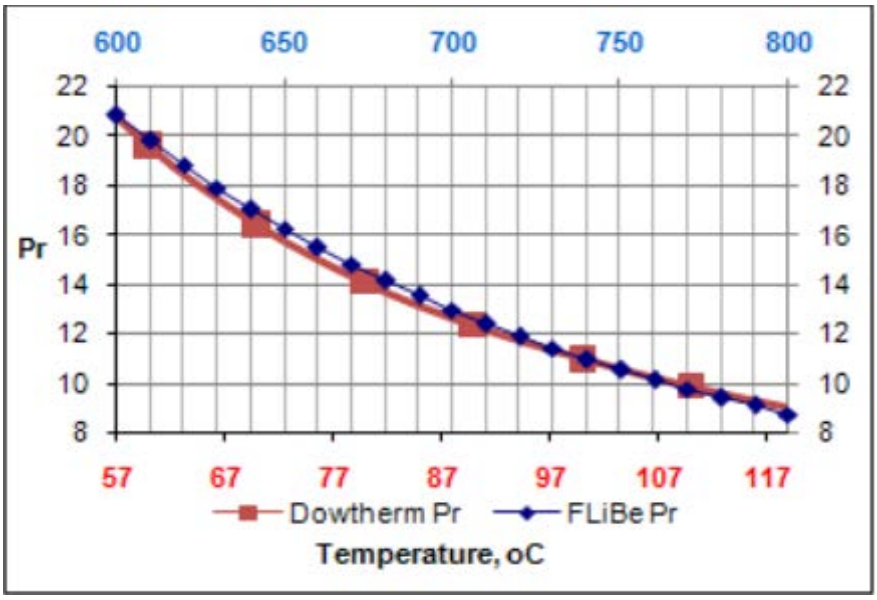

Figure 3-15: Prandtl number comparison between Dowtherm A and Flibe

Test Section Design

A dimple-walled test section was filled with 0.00635m diameter copper pebbles that were randomly and loosely packed. 7 of these pebbles are instrumented with 30.48 cm (12″) long Type T thermocouples, and were routed through two Conax fittings which were mounted on the test section. The diameter of the thermocouples was 0.0508 cm (0.02 inches). The dimpled part of the test section is 0.0889m in length and 0.04445m in diameter.

The test section is cylindrical, with a length of 88.9 mm (3.5 inches) and a diameter of 44.5 mm (1.75 inches) and is filled with 0.00635 mm (1/4 inch) diameter copper pebbles. The wall of the test section is dimpled to break up ordered packing of the pebbles at the wall in order to better simulate an infinite bed. A picture of the test section is shown in Figure 3-16. Some of these pebbles were instrumented with thermocouples. Thermocouples were also used to measure the bulk fluid temperature at the inlet and outlet of the test section. Pebble temperatures in various axial and radial locations in the test section were recorded. The instrumented pebbles had holes drilled to their centers where thermocouples were cemented. Because of the high thermal conductivity of copper, the pebble surface temperature can be assumed to be the same as the center temperature. The Biot number ranges in an individual copper sphere was from 0.005 to 0.024, which is smaller than 1. Thus, this approximation is justified [63], and further details are shown in Chapter 2.

A stainless steel screen was placed at the bottom of the test section before the filling procedure began. The test section was filled with two pebbles at a time, and a photo was taken at every interval until the dimpled section was filled. In this way, individual co-ordinates for each pebble are recorded. This is necessary if the test section is to be analyzed through Discrete Element Modeling (DEM) in the future. Figure 3-16 and Figure 3-17 show the test section when empty and filled with pebbles. Figure 3-18 shows how a drill press was used to obtain a press fit between the glass test section tube and the O-rings in the aluminum flange. Once the test section was filled, another metal gauze was placed on top of the pebbles to ensure that they stay in their configuration when oil flows through it. Test Section #1 was loosely shaken and had a porosity of 0.48. Test Section #2 was shaken more as the pebbles were being loaded, resulting in a loosely packed geometry with a porosity of 0.45. By using different size pebbles and different techniques for loading the pebbles into the same test section, different porosities can be studied in PBHTX in the future.

Figure 3-16: Left - empty test section. Right - Test section filled with copper pebbles

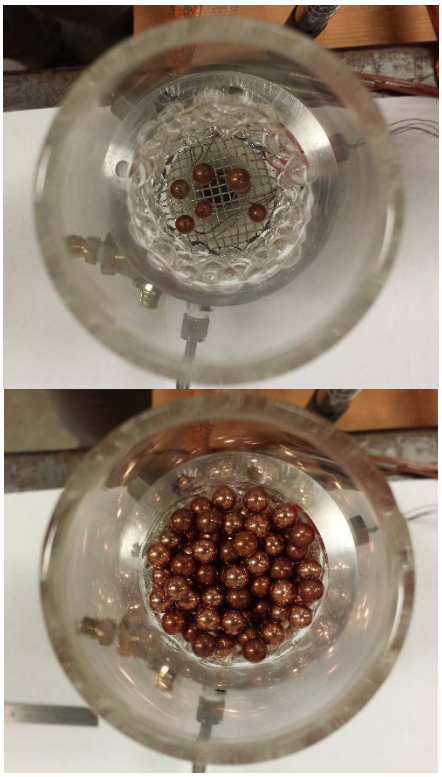

Figure 3-17: Top view of the empty and filled test section with the 6 instrumented pebbles (7 pictured but one of them broke)

Figure 3-18: Left – Drill press used to get a press fit between the glass tube and the aluminum flanges. Right - Test section filled with copper pebbles for heat transfer coefficient measurement experiments

Figure 3-19 and Figure 3-20 show the axial positions of the pebble and fluid thermocouples. There were two instrumentation arrangements with which data was recorded, labeled Test section #1 and Test section #2. Test Section #2 was developed to add more instrumented pebbles in different axial positions. The most noteworthy improvement was instrumenting two pebbles at x = 0, on the entrance screen. Two instrumented pebbles provided redundant measurements. Additionally, the location of T08P and T09P was the same as the bulk fluid temperature thermocouples T10I and T11I, facilitating data reduction.

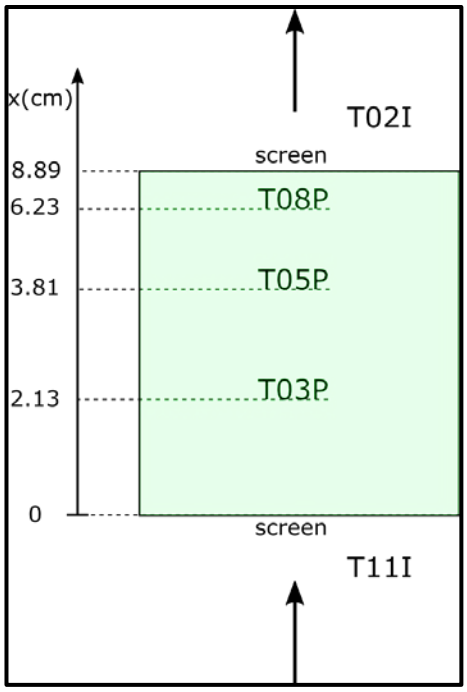

Figure 3-20: Test section #1 is divided in 3 axial regions. Instrumentation locations for pebbles (labelled with 'P') and bulk fluid temperatures (labelled with 'I') are shown.

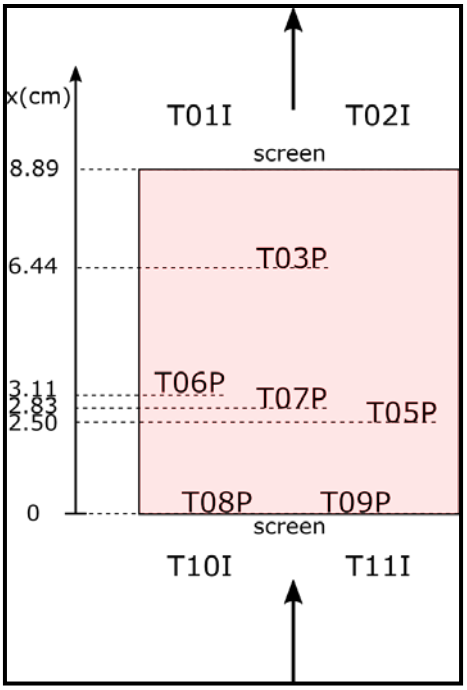

Figure 3-19: Test section #2 is divided into 5 axial regions. Labels are the same as in Test Section #1

3.5.2 Instrumentation and Data Acquisition

In this section, the instrumentation and the data acquisition system used to collect data from PBHTX is outlined.

Temperature measurements

PBHTX is instrumented with Type-T ungrounded, sheathed thermocouples. The diameter chosen was 0.0508 cm (0.02″) given the fast response of the small diameter thermocouple beads. Sheathes of 7.62 cm (3″) and 10.16 cm (4″) lengths are instrumented in the pipes, measuring the fluid temperature near the wall and at the center. 30.48 cm (12″) length thermocouples were used to instrument the test section, through Conax fittings at the bottom of it.

Flow rate measurements

A Coriolis flowmeter is used to directly measure the flow rate of the oil through the loop. This was a Siemens SITRANS FC430. This flowmeter replaced an older installed Siemens Coriolis flowmeter.

Pressure measurements

Transparent Teflon manometer lines are used to directly measure head at six points in the loop. These lines are routed to a vertical manometer board, where the fluid levels can be read off. It is possible to de-bubble the system using these manometer lines. An extra manometer line M-7 was installed at the highest point in the flow loop, right above the test section, specifically for debubbling purposes.

Data acquisition system

A National Instruments data acquisition system (DAQ) is used to relay readings from the instrumentation to the control computer. The DAQ collects readings from 24 thermocouples and 1 flowmeter. A LabView interface is used to communicate between the DAQ, the pump's variable speed drive, the heater's power supply and the computer. The data is recorded as an lvm file (a LabView measurement file).

3.5.3 Experimental Methodology

For temperature frequency response test, a methodology was followed to collect data to determine the heat transfer coefficient within the test section. A test matrix was adhered to so that the Reynolds and Prandtl numbers of interest were investigated. Table 3-6 shows the achievable ranges of various experimental parameters. The ranges presented are for Drakesol 260AT, and a similar table should be developed for Dowtherm A. The density of Drakesol 260AT is smaller compared to Dowtherm A, so a larger flowrate would be needed to achieve the same Reynolds number in the test section. To estimate

the required flow rate, an average temperature of 80 °C was assumed, which corresponds to a Prandtl number of 28. The ranges of Prandtl numbers studied in PBHTX will encompass the PB-FHR conditions, although data at high Prandtl numbers (corresponding to lower oil temperatures) will also be collected. This is for three reasons. There is a lack of experimental data for high Prandtl number heat transfer coefficients, so this work will add to the existing literature. Additionally, collecting data at high Prandtl numbers will also allow for a more comprehensive empirical correlation to be developed. Furthermore, this data will contribute to understanding heat transfer during overcooling transients, when the coolant salt temperature is significantly lower than during normal operation.

Table 3-6: Range of experimental parameters to vary

Experimental Parameter	Range in PBHTX	Comments
Range of flowrates (kg/h)	0 – 500	Corresponds to Reynolds of 0-430
Baseline power to heater (kW)	0-9	
Oil temperature range (°C)	20-90	At prolonged high temperatures the properties of Drakesol 260AT may degrade. Viscosity tests are done before and after each experimental run to ensure that the properties are consistent
Amplitude of heater power oscillation (kW)	0-4.6	The restriction is that the amplitude cannot be higher than the baseline power. The max power should not exceed 9.6kW (as this is the maximum rating of the water heater) and the minimum power cannot be less than 0kW. 0 amplitude implies no oscillations, steady power to the heater
Frequency of oscillation (Hz)	0.01-0.1	If the frequency is not high enough, there will be no noticeable temperature difference in the pebbles. Conversely, if the frequency is too high the pebble temperature will not have time to change, but the temperature difference will be higher than if a lower frequency were used

The experimental methodology is as outlined below:

1. The pump speed is controlled with the variable speed drive, so the required flow rate is achieved
2. The heater baseline power, amplitude and frequency are input into LabView and the power supply turned on.
3. The water line that supplies the heat exchanger is turned on, ensuring that the heated oil comes back down to the cold temperature.
4. The data collection duration will depend on the frequency of the heater power oscillation, and on when a steady periodic oscillation of oil and pebble temperature is obtained
5. The temperature and flowrate data is recorded using LabView. Head loss data is recorded manually.
6. By following a data reduction procedure, the heat transfer coefficients can be extracted from the temperature data. By developing a transfer function on the test section using the oil inlet and outlet temperatures, the thermal inertia of the test section can also be determined.
7. Once sufficient data is collected, a correlation for the pebble-bed Nusselt number (which is the non-dimensional ratio between the convective and conductive heat transfer in the fluid) for PB-FHR conditions can be developed.

3.6 Data Analysis Procedure and Uncertainty Analysis Procedure

This section covers how the interfacial heat transfer coefficient was determined from the raw experimental data and when parameters went into the uncertainty analysis procedure. There is also a discussion about the assuming quasi-steady state conditions during the experiment.

3.6.1 Deriving Experimental Interfacial Heat Transfer Coefficient

The heat transfer coefficient is extracted from the temperature data by equating the rate of change of internal energy of the pebbles and the convective heat transfer between the pebbles and the surrounding fluid, as shown in Equation (3.57). Fluid temperatures from the middle sections were estimated using the fluid energy conservation equation using finite differences, as shown in Equation (3.58). Equation (3.57) and (3.58) can then be used for each control volume section. Thus the heat transfer coefficient extracted from the data is a function of axial position and time. There is not much variation of temperature in the radial direction in the test section. The variation that is present falls within the error in reading of the Type T thermocouples from Omega Engineering, which is 1°C. Temperature data was collected as a function of time, with twenty readings taken every second. The experimental Nusselt number was extracted for each time step.

The data reduction was done at the entrance section, between the pebbles at the entrance at the fluid inlet temperature. This is because data was directly collected from this control

volume section. Direct data is also collected at the exit section, but this was not used in the data reduction because the outlet fluid and the pebble temperature at the exit reach equilibrium and there is no longer a detectable temperature difference between the two.

$$(1-\varepsilon)(\rho c_p)_s\left(\frac{\partial T_s}{\partial t}\right)_{section1} = h_{sf}(t)a_v(T_f - T_s(t))_{section1}$$

$$h_{sf}(t) = \frac{(1-\varepsilon)(\rho c_p)_s\left(\frac{\partial T_s}{\partial t}\right)_{section1}}{a_v(T_f - T_s(t))_{section1}} \tag{3.57}$$

$$\varepsilon(\rho c_p)_f\left(\frac{\partial T_{f1}}{\partial t}\right)_{section1} + \varepsilon(\rho c_p)_f\left(u_z\frac{\partial T_f}{\partial z}\right)_{section1\,to\,section2} = h_{sf}(T_{s1} - T_{f1})_{section1}$$

$$\varepsilon(\rho c_p)_f\left(\frac{\partial T_{f1}}{\partial t}\right)_{section1} + \varepsilon(\rho c_p)_f\left(u_z\frac{\Delta T_f}{\Delta z}\right)_{section1\,to\,section2} = h_{sf}(T_{s1} - T_{f1})_{section1} \tag{3.58}$$

The definitions of the terms in Equations (3.57) and (3.58) are as follows: ε is the porosity, $(\rho c_p)_s$ the volumetric heat capacity of the pebble (copper in the test section), T_s the temperature of the pebble ('solid' phase), t time, h_{sf} the heat transfer coefficient, a_v the specific surface area of the test section, defined in Equation (3.8), T_f the oil temperature ('fluid' phase), $(\rho c_p)_f$ the volumetric heat capacity of the oil, u_z the axial superficial velocity of the fluid in the test section and z the axial position co-ordinate. The subscript *section 1* refers to control volume section 1. The subscript *1* refers to properties in control volume section 1. The subscript *section 1 to section 2* refers specifically to the advection term, and refers to the axial distance between the entrance to section 1 and the entrance to section 2. An example of this is shown in Figure 3-21, which is from Test Section #2.

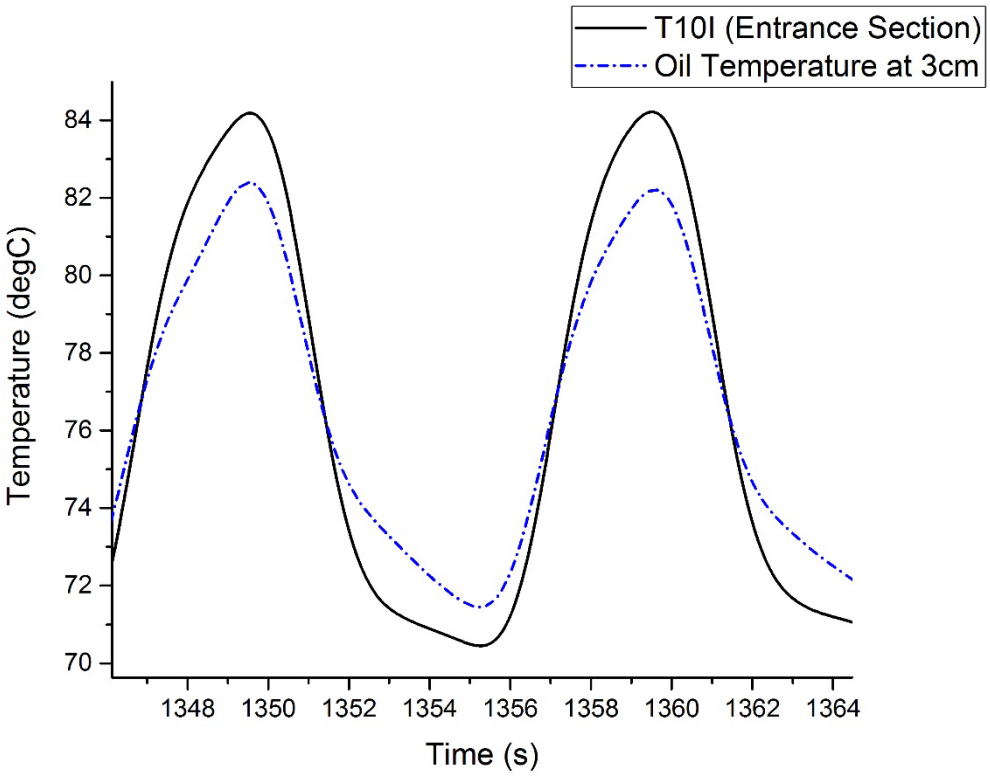

Figure 3-21: Experimental entrance oil temperature and calculated oil temperature at 3cm into the test section

The porosity ε was measured and found to be 0.48 for Test Section #1 and 0.45 for Test Section #2. In both cases the test section configuration was a loosely-packed randomly packed pebble bed test section. The Nusselt number was predicted at every time step using the measured temperatures to evaluate the relevant non-dimensional numbers. The correlation for Nusselt number is given in Equation (3.10), with Reynolds and Prandtl previously defined. The KTA correlation [67] was developed for gas cooled pebble-bed reactors and was considered, but was not expected to accurately depict the interfacial heat transfer coefficient of the test section. This is because the Prandtl number range for helium, the coolant of the gas cooled reactors, is about 0.65, much lower than flibe at the PB-FHR operating temperature which ranges from 10-15. The film temperatures were used to evaluate the Reynolds and Prandtl numbers, which were in turn used to evaluate the Nusselt number. The experimental h_{sf} was used to find the experimental Nu_{sf} so it could be compared to the correlations. This was done using Equation (3.59), which takes into account the particle conductivity [68]. The film temperature is defined in Equation (3.56). The film temperature is used because it is the average temperature across the thermal boundary layer over each pebble.

$$T_{film} = \frac{T_s + T_f}{2}$$

$$Nu_{sf} = 2 + 1.1 \mathrm{Pr}^{1/3} \mathrm{Re}^{0.6}$$

$$\frac{1}{h_{sf}} = \frac{D_p}{Nu_{sf} k_f} + \frac{D_p}{\beta k_s} \qquad (3.59)$$

k_f is the thermal conductivity of the oil in $Wm^{-2}K^{-1}$, k_s is the thermal conductivity of the copper in $Wm^{-2}K^{-1}$, D_p the particle diameter in m, β a geometrical constant depending on the shape of the particle (for spheres it is 10) [15].

The relevant data was chosen on the basis of the temperature difference achieved between the oil and the pebbles. If the temperature difference was below 2.5°C, it was rejected. This is because the error in the thermocouples is 1°C. With two thermocouples, the absolute error is doubled. A 2.5°C difference has enough margin to take this error into account. Additionally, with a smaller temperature difference (for example if the oil and pebble temperatures are similar, as they are during thermal equilibrium), the extracted heat transfer coefficient is an arbitrarily large value. The derivative of the pebble temperature was also considered. As the oscillations were periodically pulsed, portions of the pebble temperature response have steep slopes. These slopes are prone to large errors. In the current study the heat transfer coefficients from the central regions of the test section have not been evaluated. This is because the difference between the fluid temperatures in the central sections and the pebbles at that location was less than 2.5°C.

3.6.2 Experimental Runs

The attained ranges of Reynolds and Prandtl numbers are shown in Table 3-7.

Table 3-7: Summary of the PBHTX experimental runs and corresponding non-dimensional number ranges

Date	Prandtl	Reynolds	Test Section	Heater power (kW)	Max ΔT (°C)
2016-02-25 RUN 1	49-75	54-82	Test section #1	1.991	10
2016-02-25 RUN 2	49-72	49-72	Test section #1	2.958	13
2016-02-25 RUN 3	48-60	68-85	Test section #1	2.969	17
2016-03-15	27-36	230-289	Test section #1	3.522	6
2016-10-26 RUN 1	26-33	240-303	Test section #2	3.476	6
2016-10-26 RUN 2	27-30	360-412	Test section #2	1.016	2.5
2016-10-26 RUN 3	30-35	312-369	Test section #2	3.005	4

3.6.3 Uncertainty Analysis Procedure

The biggest contributions to uncertainty in the experimentally derived h^* are from dT_s/dt, T_s and T_f. The porosity ε also has an associated uncertainty with it since it was measured manually prior to the tests. It is important to note that the uncertainty analysis is approximate because the uncertainties associated with the material properties of the operating fluid Drakesol 260AT are unknown. The thermal conductivity and specific heat capacity of Drakesol 260AT were assumed to be constants, which may not be the case because these properties are temperature dependent in other similar oils. It was assumed that the uncertainty in the Drakesol 260AT properties were about 10%. The uncertainties associated with the properties of copper were assumed to be small enough to neglect. Uncertainty is also associated with the predicted Nusselt numbers, as the non-dimensional numbers used to calculate them were based on fluid temperatures. Thermocouple errors are associated with them. Table 3-8 shows the uncertainties associated with the instrumentation readings. The uncertainty associated with the thermocouple temperatures was 1°C or 0.75% of the reading as reported by Omega Engineering [69].

Table 3-8: Uncertainties associated with instrumentation readings

Instrumentation	Error
Type T Thermocouple	Whichever is greater, 1°C or 0.75% of reading
Coriolis Flowmeter	1% of reading

3.7 Results and Discussion

This section presents the temperature response, experimental Nusselt number, and the pressure drops measured in the test section.

3.7.1 Temperature variation in the test section

Figure 3-22 and show the temperatures of two pebbles and the bulk fluid at the entrance of the pebble-bed test section as a function of time. These results were for the Test Section #2 configuration, and all the runs showed similar response. The locations of the thermocouples are shown in Figure 3-20. Thermocouples T08P and T09P are located on the screen at the entrance to the test section, and T10I is the fluid temperature at the entrance. Figure 3-22 shows the response for periodic pulsed forcing at a frequency of 0.1Hz (implying a period of 10 seconds) while a frequency of 0.05 Hz (a 20 second period). The lower the frequency, the closer the fluid and solid phase temperatures and the less the lag between the two. This is because the pebbles have time to heat up to the fluid temperature. With the higher frequency the temperature amplitude difference and time lag are much more pronounced, and this can be seen more clearly in Figure 3-22 for Test Section #2. The higher the convective heat transfer coefficient the smaller the resulting temperature difference.

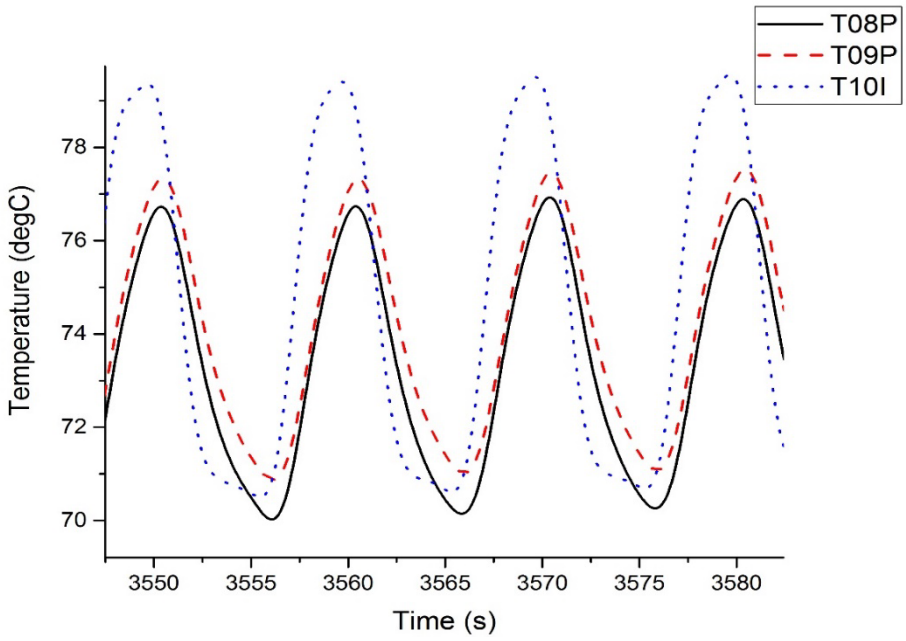

Figure 3-22: Temperature of pebbles at the inlet (T08P and T09P) and the inlet fluid (T10I) at the entrance of Test Section #2. The frequency of oscillations is 0.1Hz (10 second periods)

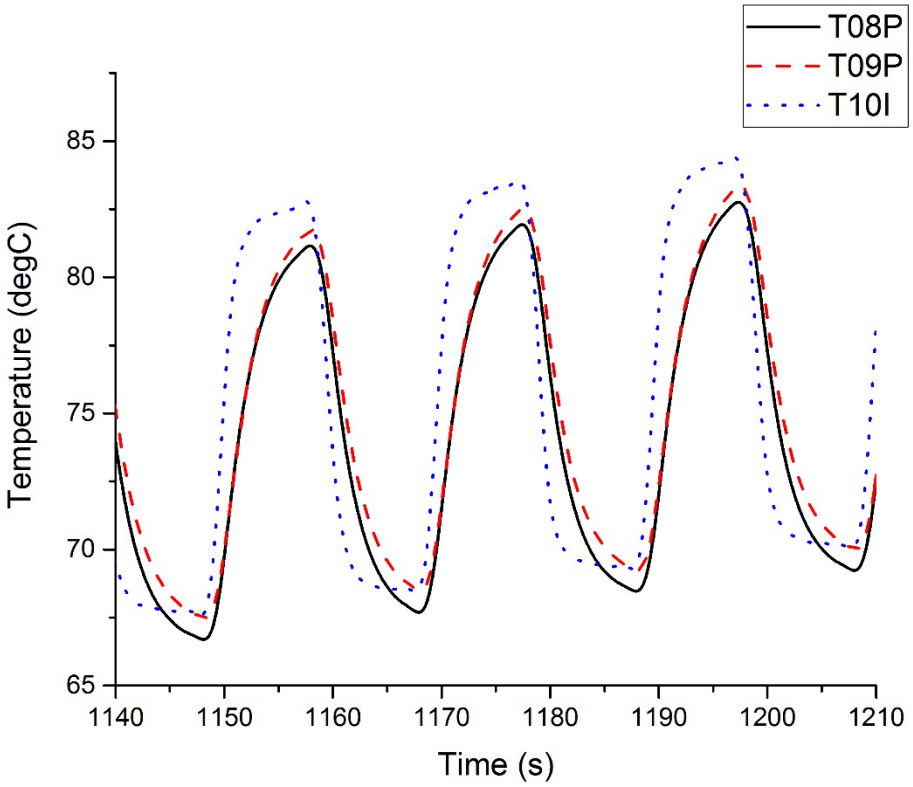

Figure 3-23: Temperature of pebbles at the inlet (T08P and T09P) and the inlet fluid (T10I) at the entrance of Test Section #2. The frequency of oscillations is 0.05Hz (20 second periods)

Figure 3-24 shows the temperatures of a pebble near the exit section and the outlet fluid temperature as a function of time for Test Section #2. T01I is the bulk fluid temperature at the exit and T03P is located near the top of the test section. It can be seen that by the time the fluid exits the test section, it is around the same temperature as the pebbles (the graph shows a 1°C difference between the two readings, which is within the margin of error for a Type T thermocouple). Additionally, it can be seen that there is very little phase lag between the pebble and the fluid temperatures as well. This indicates that there is negligible convection heat transfer occurring at the exit section. Therefore the best data to use for the heat transfer coefficient extraction are at the entrance section.

The transient in Figure 3-24 starts off with steady state readings, and it can be seen that there is a constant difference in temperature in Region I. This is most likely a systematic bias due to a calibration error in those two thermocouples. A similar 1°C bias was found between the entrance fluid and thermocouple readings in Test Section #2, and this was included in the data analysis by subtracting it out.

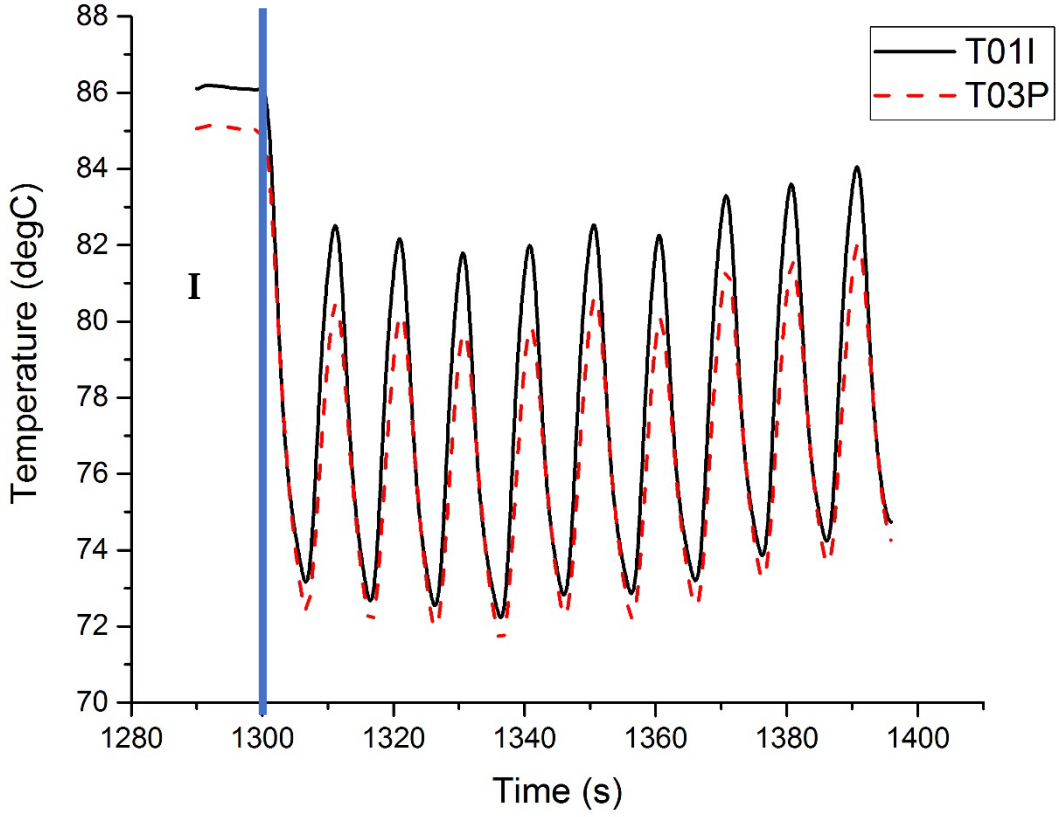

Figure 3-24: Temperature of pebbles near the outlet (T03P) and the outlet fluid (T01I) at the exit of Test Section #1. The frequency of oscillations is 0.1Hz (10 second period)

Figure 3-25 shows the temperatures of the fluid and the three instrumented pebbles for a couple of cycles during a 0.1Hz run in the Test section #1 arrangement. It can be seen that the exit fluid temperature has a phase lag of about $\pi/2$ compared to the entrance fluid temperature. Additionally, we can see that there is not a large variation in the three pebble temperatures though they are axially in different positions in the test section. This further reinforces the lumped capacitance assumption of the test section. However to properly characterize the thermal inertia of the copper pebbles, the heat transfer coefficient needs to be known.

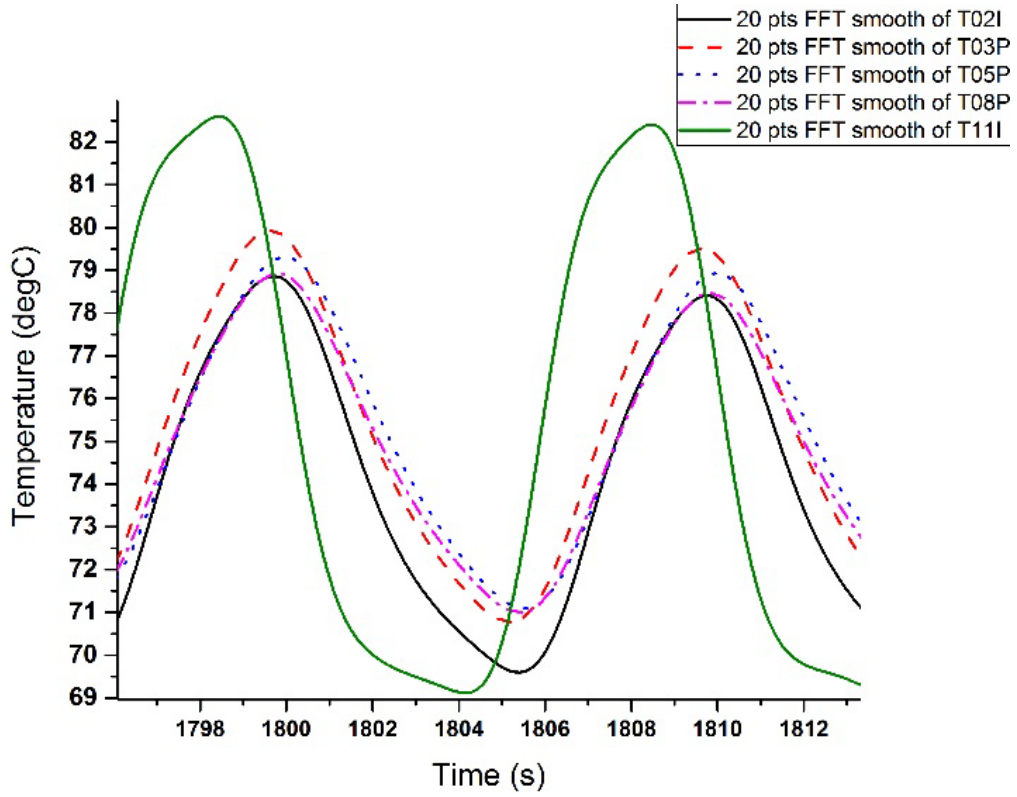

Figure 3-25: Temperature of three pebbles and different axial locations and the bulk fluid near the inlet and outlet of Test Section #1. The heater is pulsed with a frequency of 0.1Hz

Figure 3-26 shows the Fast Fourier Transform (FFT) decomposition of the periodic pulsed forcing function shown in Figure 3-25. The FFT was performed on T11I in Test Section #1, which was the oil inlet temperature in Test Section #1. It can be seen that the majority of the signal is at 0.1Hz, with smaller peaks at 0.2Hz and 0.3 Hz. Therefore, using a pulsed periodic function is likely to be a valid alternative to a clean sinusoidal input.

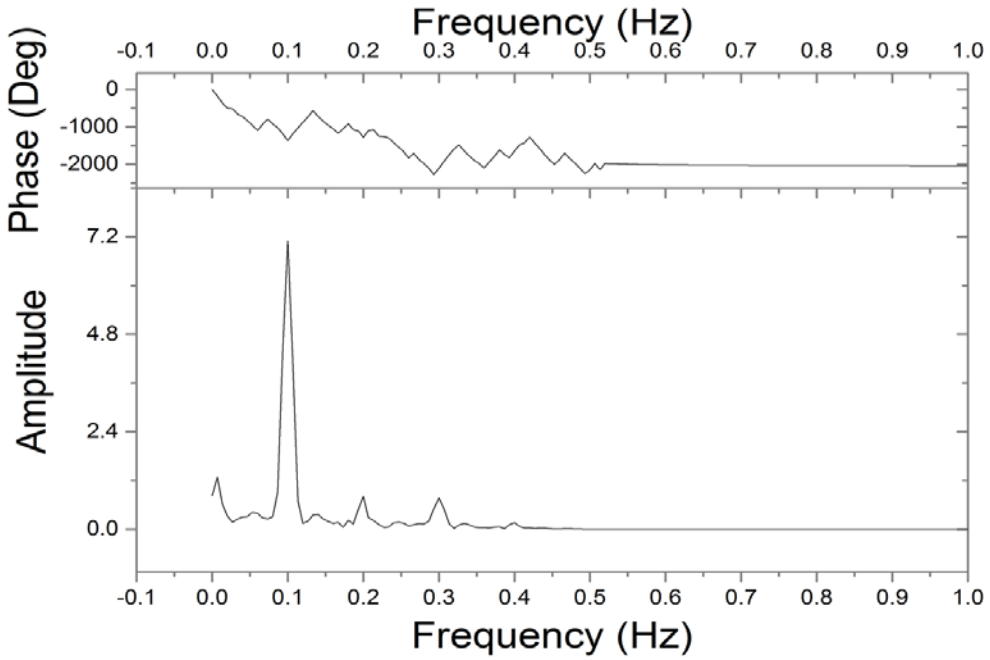

Figure 3-26: FFT of T11I done in Origin for the 0.1Hz pulsed tests, corresponding to Figure 3-25 (Test Section #1)

There is a discrepancy between the experimental temperature responses shown here and those predicted by the analytical model. Figure 3-24 shows that the temperatures of both the oil and the pebbles eventually reach equilibrium at the exit. However the predictions in Figure 3-1 and Figure 3-2 show a constant temperature difference between the oil and pebbles even at the exit section. This is likely due to the heat losses from the fluid to the glass and metal flanges of the test section, which should be included in future improvements to the analytical model. Although calibration biases may be a small contributing factor, it is unlikely to explain everything as they are within 1°C.

3.7.2 Radial temperature variation in the test section

There is not much variation of temperature in the radial direction in the test section, as shown in Figure 3-27. Three pebble thermocouples were situated at different radial positions at the same axial height, halfway up the test section. This set up was for an older instrumentation configuration of the test section. The variation that is present falls within the error in reading of the Type T thermocouples from Omega Engineering, which is 1°C.

Figure 3-28 shows the radial temperature variation during heater oscillations, with the new Test Section #2. Again, it can be seen that the temperature variation even at high temperatures is within 1°C. The temperatures shown are for T08P and T09P, which are situated on the screen at the entrance of the test section. Therefore it can be shown experimentally that the temperature distribution radially is uniform albeit with a calibration bias, and that the fluid temperature through the test section must also be uniform radially. Thus, having the analytical solution be a function of the axial dimension only is justified. The variation is likely to be due to calibration biases in the individual thermocouples, as it is sustained with respect to time.

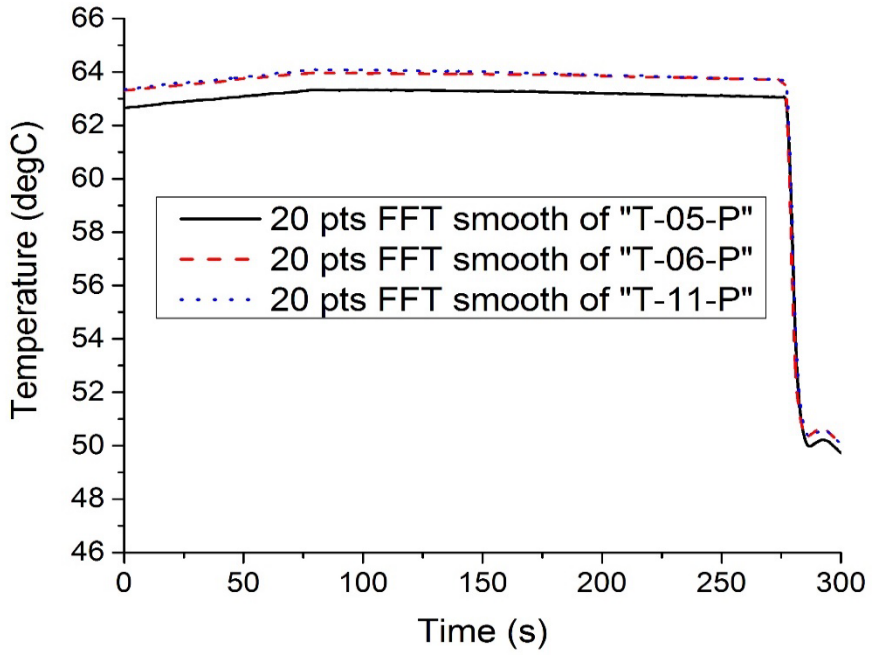

Figure 3-27: Radial temperature distribution between three pebbles at the same axial position. This instrumentation was from an older test section set up

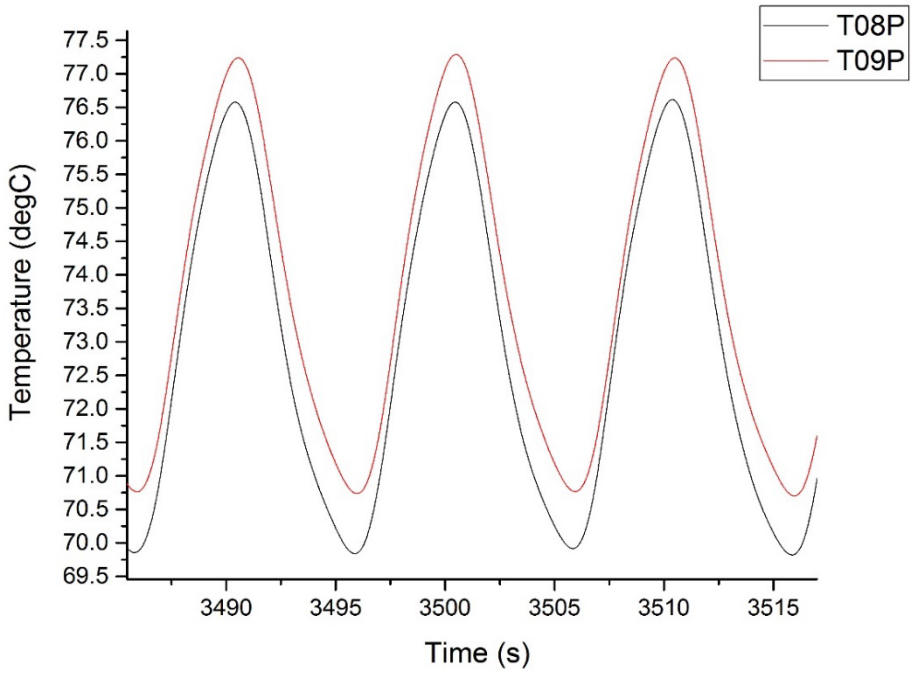

Figure 3-28: Radial temperature variation in Test Section #2, at the entrance (axial elevation = 0), during oscillations

3.7.3 Experimental Nusselt number

Figure 3-29 to Figure 3-33 show the disagreement between the predictive Wakao correlation and the experimental Nusselt number as a function of Prandtl and Reynolds. Figure 3-29 shows all the data collected, and the subsequent figures are close-ups of the four main regions. The navy blue region represents null data. The red regions represent the prediction being larger than the experimental value. The blue regions represent the ranges in which the experimental Nusselt number was larger than the prediction, implying that the Nusselt number was being under-predicted. Figure 3-30 and Figure 3-31 show results for low Reynolds number flows in the laminar regime. These results suggest that for high Prandtl numbers (between 50 and 85) and laminar Reynolds numbers, the Wakao correlation overpredicts the experimental values. However the discrepancy is at most 15.4%, which is within the 20% margin that is usually used for heat transfer experiments. Nonetheless it should be noted that the correlation consistently overpredicts the heat transfer in that region, compared to the other three regions in which the experimental values exceed the predictions by up to 32%. This can be seen from Figure 3-32 and Figure 3-33 which show the experimental data collected for high Reynolds numbers in the transition/turbulent regime. The Wakao correlation does not take into account porosity. The porosity in the PBHTX test section is likely to be lower than the porosity in the PB-FHR, although the PB-FHR reactor core will have porosity variations due to the wall of the core. A higher porosity means that more fluid can flow through, which implies better heat transfer. This may be an explanation for the higher

experimental Nusselt numbers compared to the predictions. But overall, the Wakao correlation seems to predict the heat transfer in PBHTX for PB-FHR conditions fairly well.

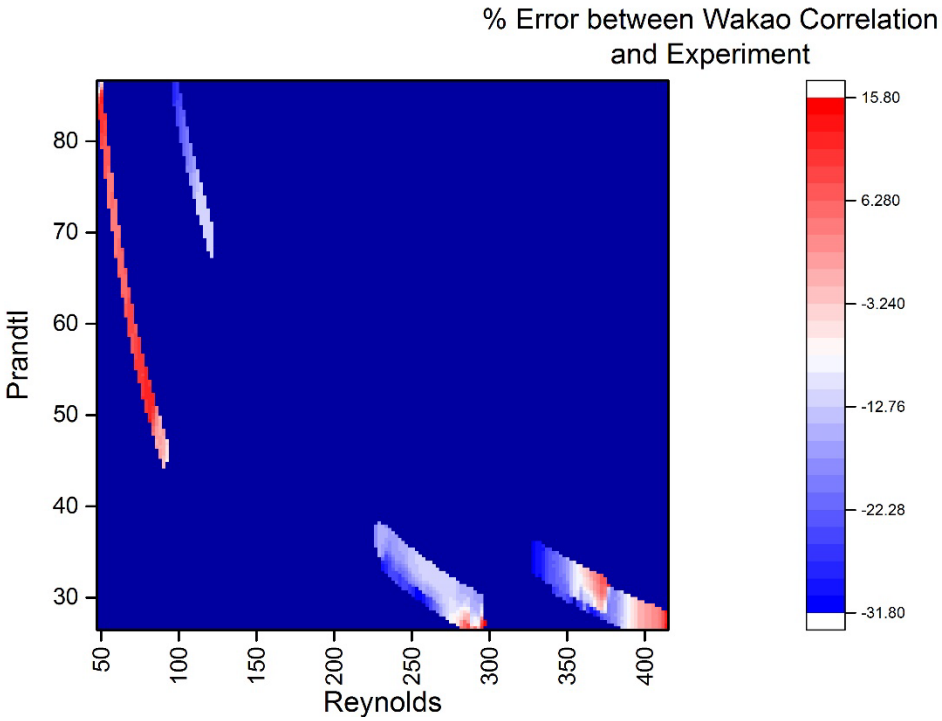

Figure 3-29: % Error between the predictive Wakao correlation and experimental values plotted as a contour plot against Prandtl and Reynolds. This graph represents all the data collected.

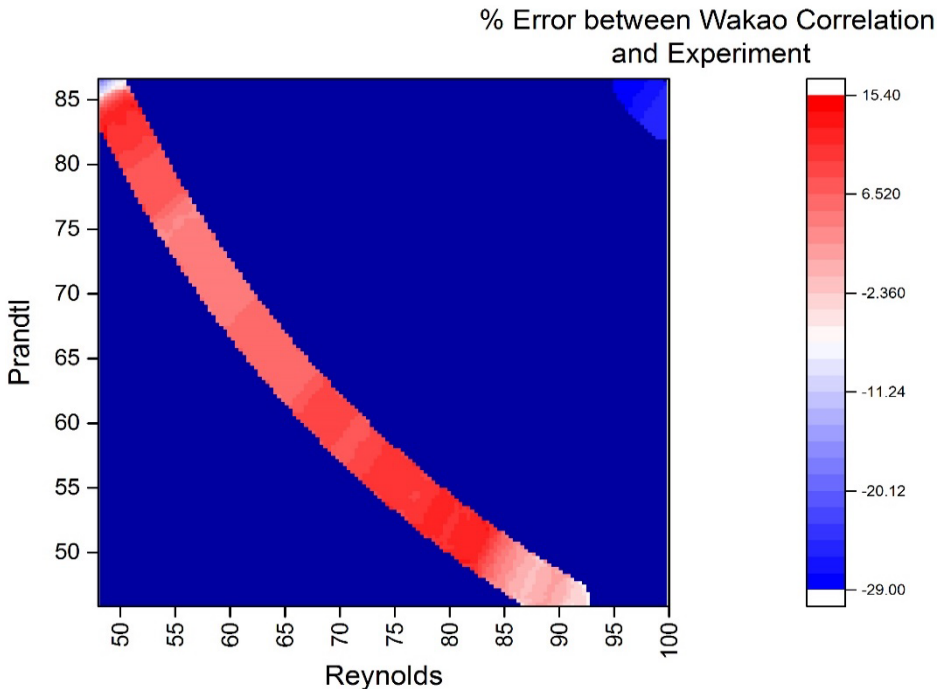

Figure 3-30: % Error between the predictive Wakao correlation and experimental values plotted as a contour plot against Prandtl numbers from 50 - 80 and Reynolds from 50 - 99. This is a laminar flow regime through the test section.

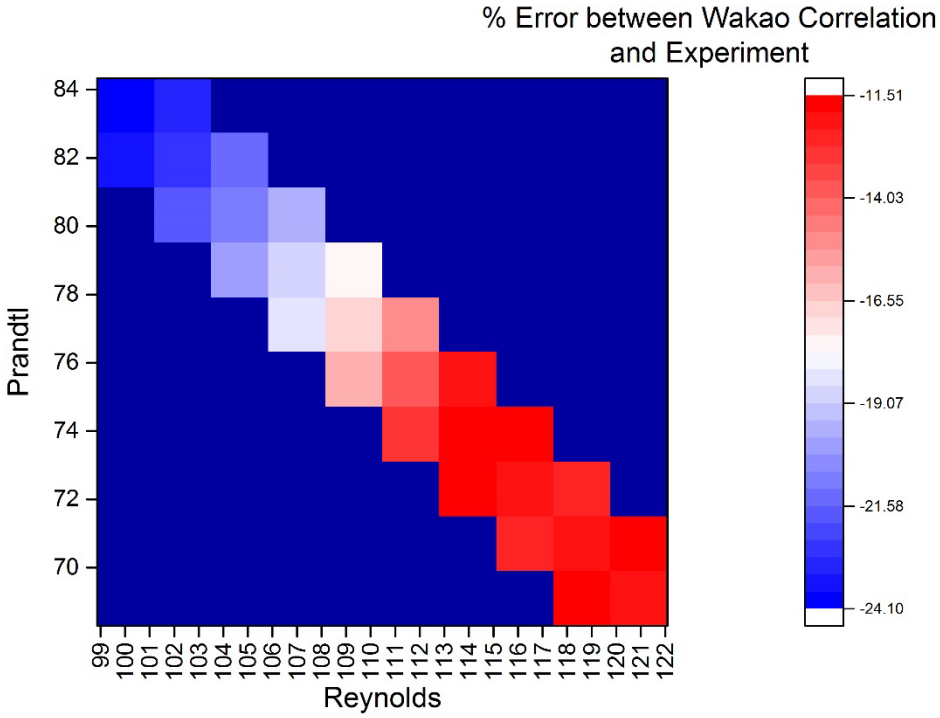

Figure 3-31: % Error between the predictive Wakao correlation and experimental values plotted as a contour plot against Prandtl from 68-84 and Reynolds from 99 to 122, which is still laminar.

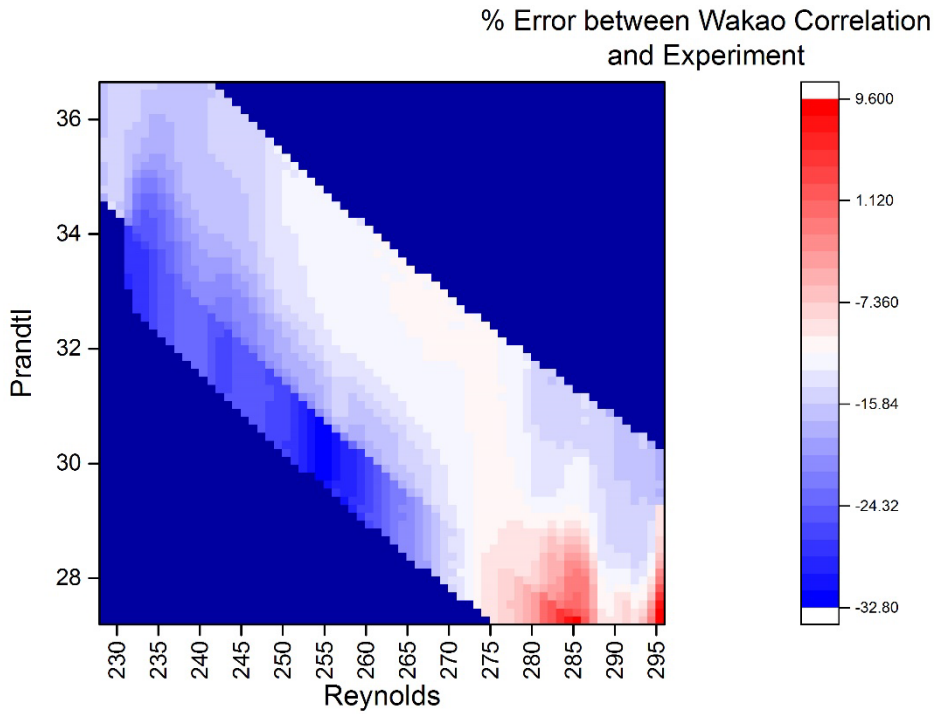

Figure 3-32: % Error between the predictive Wakao correlation and experimental values plotted as a contour plot against Prandtl from 27-37 and Reynolds from 200 to 300, which is transition/ turbulent.

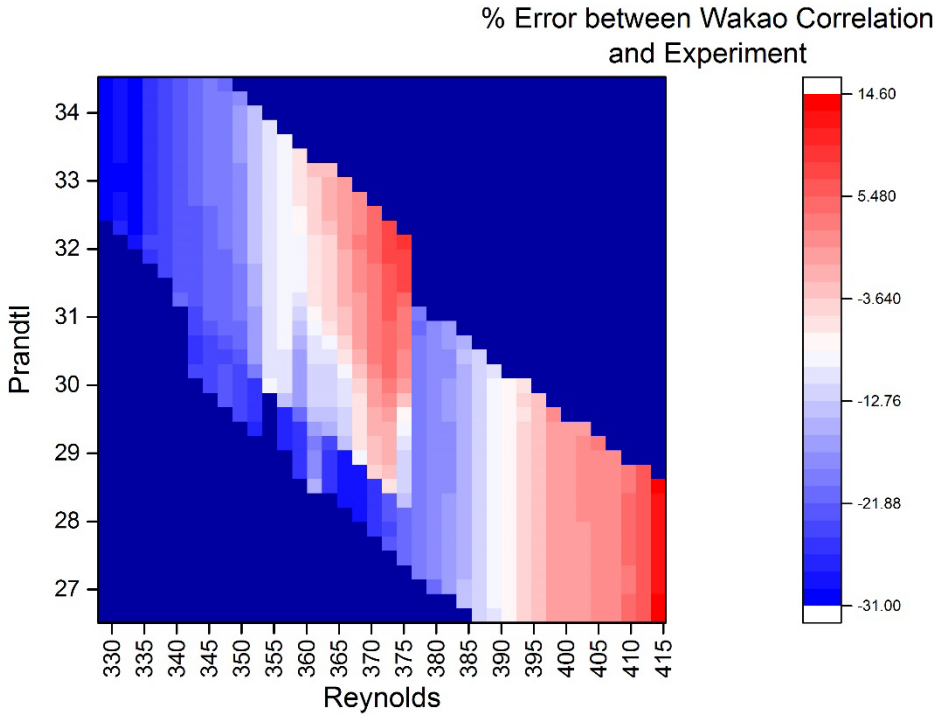

Figure 3-33: % Error between the predictive Wakao correlation and experimental values plotted as a contour plot against Prandtl from 26-35 and Reynolds from 330 to 412, which is turbulent.

3.7.4 Radiation heat transfer distortions

Thermal radiation heat transfer in the PBHTX test section is negligible during all the experimental runs that were performed, with the radiation heat transfer accounting for less than 1% of the total energy transferred between the pebbles and the fluid. Figure 3-34 shows this for 2016-10-26 RUN 1. It was assumed that the oil was transparent to thermal radiation, giving an overestimate for the thermal radiation transferred by the oil.

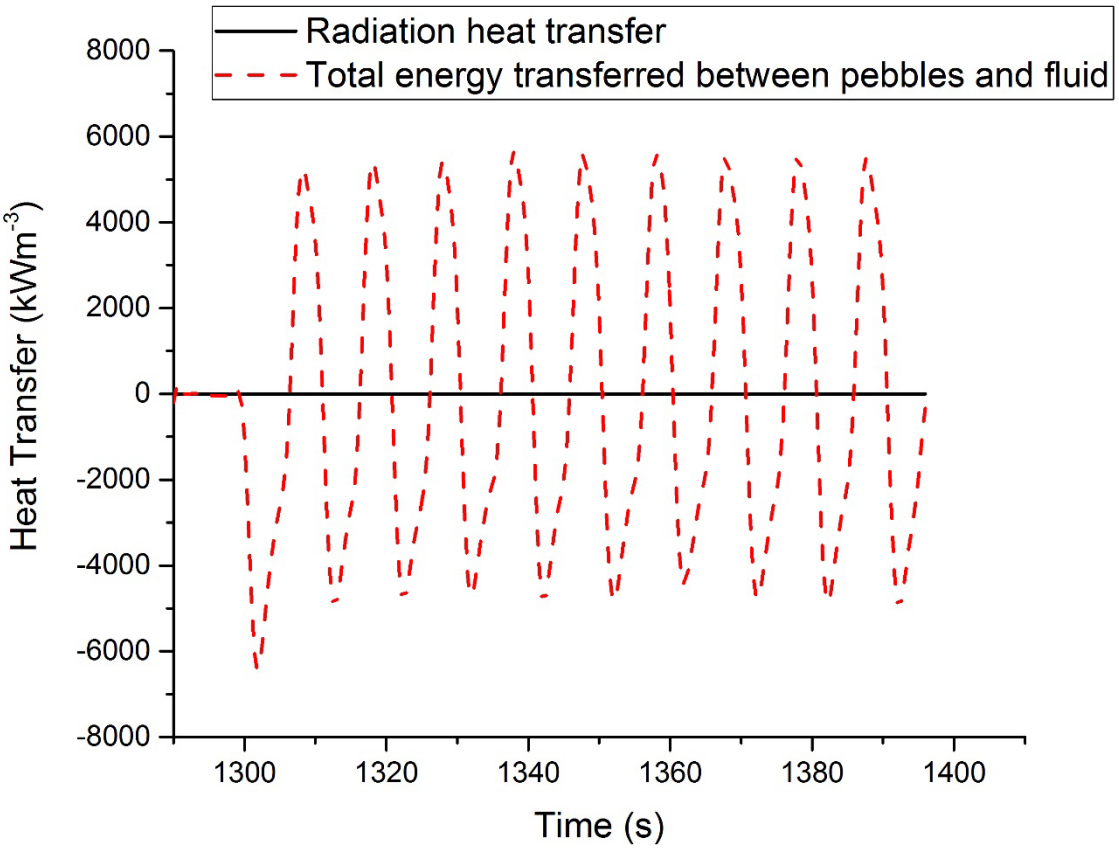

Figure 3-34: Magnitudes of heat transfer via radiation and total heat transferred in the PBHTX test section.

Recent studies have shown that thermal radiation heat transfer in fluoride salts could be a significant fraction of the convective heat transfer, especially during laminar flows [70][9]. In turbulent flow, the Nusselt number is much higher which means the convective heat transfer is large compared to other forms of heat transfer. Chaleff et. al. [70] state that for the fluoride salt flinak flowing in a pipe under laminar conditions thermal radiation could account for up to 10% of the total heat transferred depending on the impurities in the flinak. The cleaner the salt, the lower its opacity and the higher its

transparency to thermal radiation. Thus, if only convective heat transfer is assumed it may be an underestimate.

It is possible to do a high-level order of magnitude estimate for the convective and radiative heat transfer in the PB-FHR core.

$$a_v = \frac{6(1-\varepsilon)}{D_p} = \frac{6(1-0.39)}{0.03} = 120m^{-1} \tag{3.60}$$

The porosity ε is 0.39 for a tightly packed randomly packed bed of spheres. The diameter of each fuel pebble is 0.03m.

Assuming a Reynolds number of 500 and a Prandtl of 14, the Wakao correlation can be used to estimate the Nusselt number and thus the convective heat transfer coefficient as shown in Equation (3.61).

$$\begin{aligned} Nu &= 2 + 1.1\mathrm{Re}^{0.6}\,\mathrm{Pr}^{1/3} \\ Nu &= 112 \\ h_{sf} &= \frac{Nuk_f}{D_p} = \frac{112 \times 1.096}{0.03} = 4100 Wm^{-2}K^{-1} \end{aligned} \tag{3.61}$$

The flibe properties were taken at 650°C. Therefore the Q_{conv}, the convective heat transfer in the PB-FHR core is given by Equation (3.62):

$$Q_{conv} = ha_v(T_s - T_f) = 4100 \times 120 \times 100 = 49.2 MWm^{-3} \tag{3.62}$$

The heat transfer due to radiation can be estimated as shown in Equation (3.63), assuming the salt is fully transparent. The value estimated is thus the maximum heat that could be transferred via thermal radiation by the salt. In the prototypical system impurities in the salt may lead to absorption. In Equation, Q_{rad} is the radiation heat transfer in $Wm^{-3,}$ σ the Stefan-Boltzmann constant in $Wm^{-2}K^{-4}$ and φ the emissivity of graphite [71].

$$Q_{rad} = \sigma\varphi a_v(T_s^4 - T_f^4) = 5.67 \times 10^{-8} \times 0.8 \times 120(1073^4 - 973^4) = 2.4 MWm^{-3} \tag{3.63}$$

In the PB-FHR the flow regime within the pebble-bed is expected to be in the laminar/transitional range. Further analysis is required depending on the spectral absorptivity of the salt with impurities and under transition flow conditions. It is unclear how significant thermal radiation would be in this case. There are likely to be impurities in the flibe, such as graphite and chromium, which could affect the absorption coefficient. The impurities would decrease the optical depth in the salt coolant, and thus the radiation

heat transfer would be diminished. Scaled experiments using simulant oils at low temperatures cannot accurately capture the ratio of radiative to convective heat transfer seen in the fluoride systems, but it is possible that thermal radiation is small in the pebble-bed reactor core as estimated in Equations (3.62) and (3.63). Additionally, thermal radiation may be important during overcooling transients where the temperature differences are much larger than during normal operation.

3.7.5 Pressure drop tests

The results from ambient isothermal pressure drop tests in the test section are presented. The permeability and form coefficient of the test section were determined from the results as shown in Table 3-10. The HDD model was used (which was previously detailed in Chapter 1) as it accounts for the quadratic velocity term. The equation is repeated in (3.64) below.

$$\frac{\Delta P}{L} = \frac{\mu}{K}U + C\rho U^2 \tag{3.64}$$

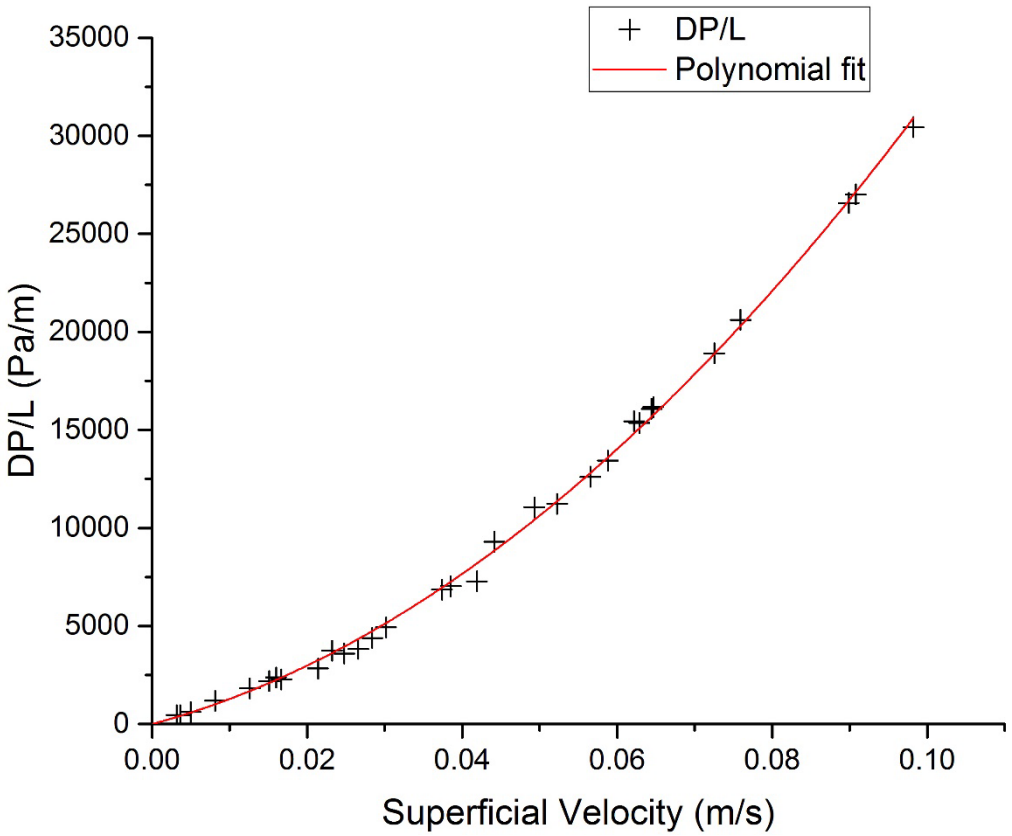

Figure 3-35: Linear pressure drop in Test Section #1 against superficial velocity in test section

It can be seen that the max Reynolds number achieved in the ambient isothermal experimental runs was about 3.5. The Reynolds number Re_K was calculated using the permeability *K* as shown in Equation (3.65). The permeability was determined from Figure 3-35. The friction factor fk was determined using the permeability and was plotted against Re_K in Figure 3-36 and compared to the literature shown in Figure 3-37. It is clear from Figure 3-36 that the higher Reynolds number data points are outside of the Darcy range (in which the flow is laminar and the pressure drop is linearly proportional to the flow velocity). Reynolds numbers above 2 are in the transition to turbulent regime, and follow the HDD model. It is likely that the flows in the PB-FHR will be in this regime as well, and further validates the heat transfer data collected using PBHTX.

$$\mathrm{Re}_K = \frac{\rho u_z K^{1/2}}{\mu} \tag{3.65}$$

$$fk = \frac{K^{1/2}}{\rho u_z^{\,2}}\left(-\frac{dP}{dx}\right) \tag{3.66}$$

Table 3-9: Best fit polynomial line of pressure drop in test section against superficial velocity

Equation	$y = \text{intercept} + \text{B1}x + B2x^2$
Intercept	0 ± --
B1	106900 ± 4240
B2	2.11E6 ± 58500
Adj. R-Square	0.99925

Table 3-10: Permeability and Form Coefficient of Test Section #1

	Expression	**Value**	**Error**
Permeability, K	$\frac{\mu}{B1}$	4.30 x 10^{-8}	+/- 11%
Form Coefficient, C	$\frac{B2}{\rho}$	266	+/- 10%

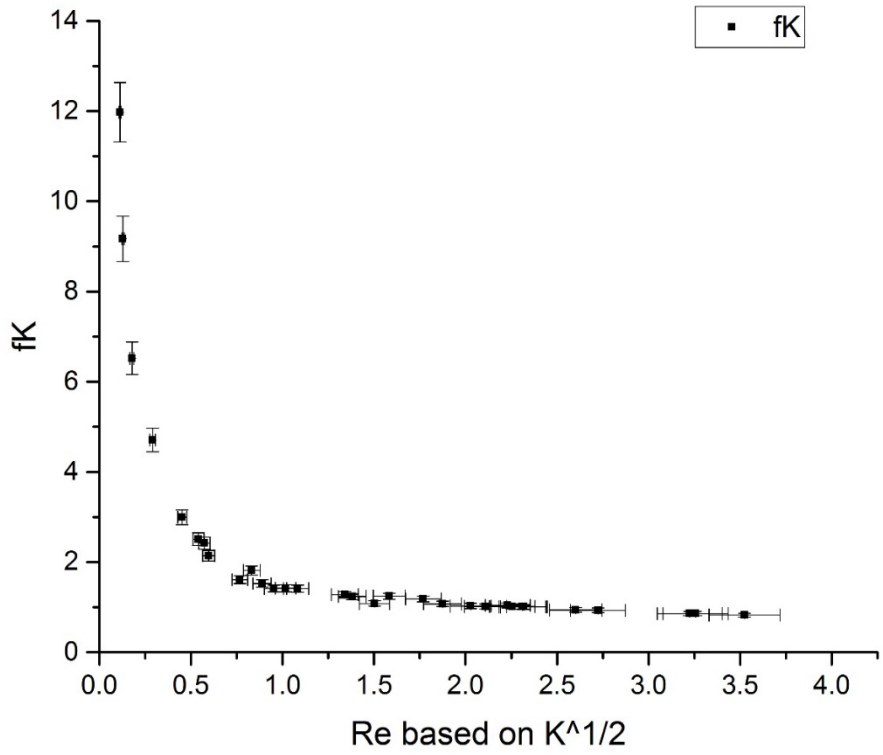

Figure 3-36: Friction factor in the isothermal ambient test section against Reynolds number based on the test section permeability

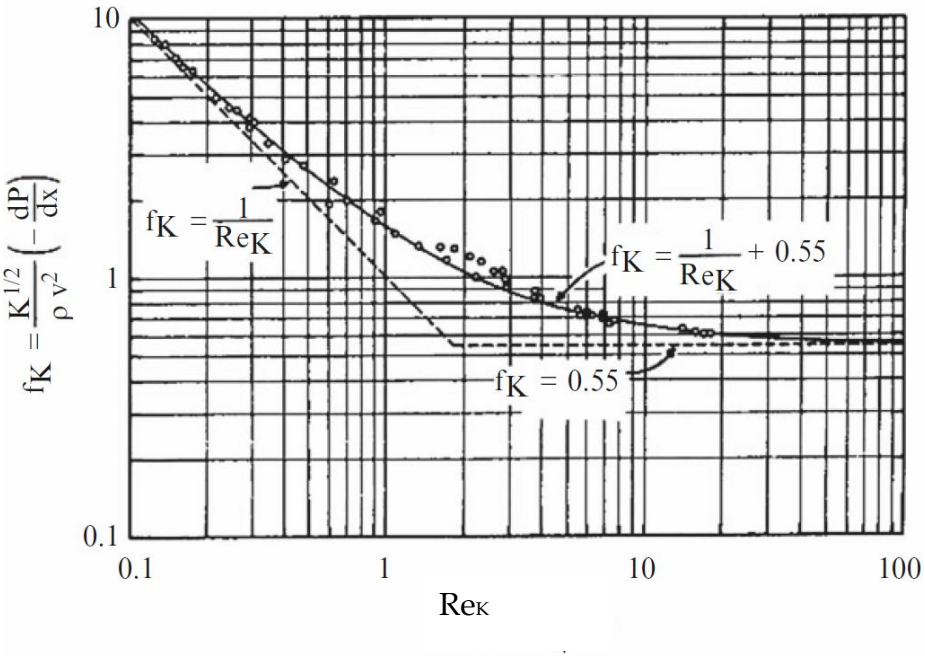

Figure 3-37: Friction factor fk against Re_K, from [15]

3.8 Conclusions and Future Work

The design and construction of the PBHTX experimental facility was outlined, and its role in determining interfacial heat transfer coefficients under PB-FHR conditions explained. A scaled experiment was performed using copper pebbles as the surrogate fuel and a heat transfer oil as the coolant. Reynolds and Prandtl numbers were matched between the scaled experiment and the prototypical conditions. Periodic pulsed tests were conducted to maximize the temperature difference between the copper pebbles and the Drakesol 260AT in the PBHTX test section. An analytical solution for the test section geometry was derived and its role in designing the experiment was shown. The experimental Nusselt numbers show that the Wakao correlation is a good estimate of the heat transfer in the PB-FHR.

The ratio of volumetric heat capacities between graphite and salt (as is the case in the PB-FHR core) does not allow for transient testing to measure heat transfer coefficients during typical reactor operation. Steady state conditions have to be achieved to study prototypical conditions. This is why scaled quasi-steady experiments hold so much potential to gain a deeper understanding of FHRs, short of building a demonstration plant. Additionally, the distortions between the experiment and the prototype should be well understood.

The same experimental setup can eventually be used to study other heat structures or variations in the pebble-bed test sections. If the fluid-to-solid ratios can be matched between the prototypical and scaled models, then the temperature response measured by the thermocouples in experiments will aid in directly identifying the response of the heat structures in the reactor system.

4. INTEGRAL RESPONSE OF THE REACTOR CORE

Chapters 2 and 3 discussed the importance of separate effects tests and their role in illuminating the thermal hydraulics behavior of flibe. One of the aims of those chapters was to demonstrate that similitude can be successfully achieved using heat transfer oils such as Dowtherm A and Drakesol 260AT. Naturally the next step would be to perform Integral Effects Tests (IET) using simulant oils. A ~50% geometrically scaled facility was constructed, with one of its primary objectives being the verification and validation (V&V) of simulation codes. Oberkampf and Trucano [72] outline the importance of the V&V process for nuclear systems. This chapter presents a model of the experimental facility using a code called Flownex, and comparisons are presented between the model and the experimental data.

4.1 Objectives of Study

One of the advantages of the FHR design is the emergency decay heat removal system, known as the Direct Reactor Auxiliary Cooling System (DRACS). It is designed to extract decay heat from the core when AC power is unavailable to operate the pumps. Two coupled natural circulation loops transport the decay heat to an ultimate heat sink – atmospheric air. A brief background on the DRACS operation was presented in Chapter 1. The Compact Integral Effects Test (CIET) 1.0 is a reduced-area scaled integral effects test (IET) designed to collect experimental data during steady state and transient forced and natural circulation in coupled loops, but at much lower temperatures than the operational conditions in the FHR. The heat transfer fluid in CIET 1.0 is Dowtherm A. The scaling of Dowtherm A to reproduce the convective heat transfer of flibe has been discussed in Chapters 2 and 3. The design of CIET 1.0 has been detailed by Zweibaum et al. [73]. Natural circulation flow occurs in the main loop when the heater is turned on without the pumps, and flows down the shell side of the DRACS Heat Exchanger (DHX) (as labeled in Figure 4-3). The heat addition to the DRACS loop induces flow in the tube side of the DHX and down the Thermosyphon-Cooled Heat Exchanger (TCHX). The CIET loops were instrumented with Coriolis flow meters and Type T thermocouples. Figure 4-1 and Figure 4-2 show photos of the as-built experimental facility.

For the Flownex model, only steady state, coupled natural circulation was considered, which means that some of the available flow paths in CIET were not modeled. The modeled portion is shown in Figure 4-3.

The aim of this chapter is to show that Flownex can be used alongside more established thermal hydraulics systems codes such as RELAP5-3D. Flownex has several advantages over RELAP5-3D that make it attractive for modeling not only FHR systems, but many

advanced nuclear reactor design. Custom equations for heat transfer coefficients and friction coefficients can be easily input via scripting elements. Additionally, the thermal hydraulics system model can be coupled with a point kinetics model. The capability to couple Flownex to RELAP and Matlab makes it flexible and powerful. One of the drawbacks of most systems codes is the ability to model freezing phenomenology. The study shown in this chapter is to verify that Flownex can be used to model a coupled natural circulation loop, which is the first step to developing more involved models for the prototypical system.

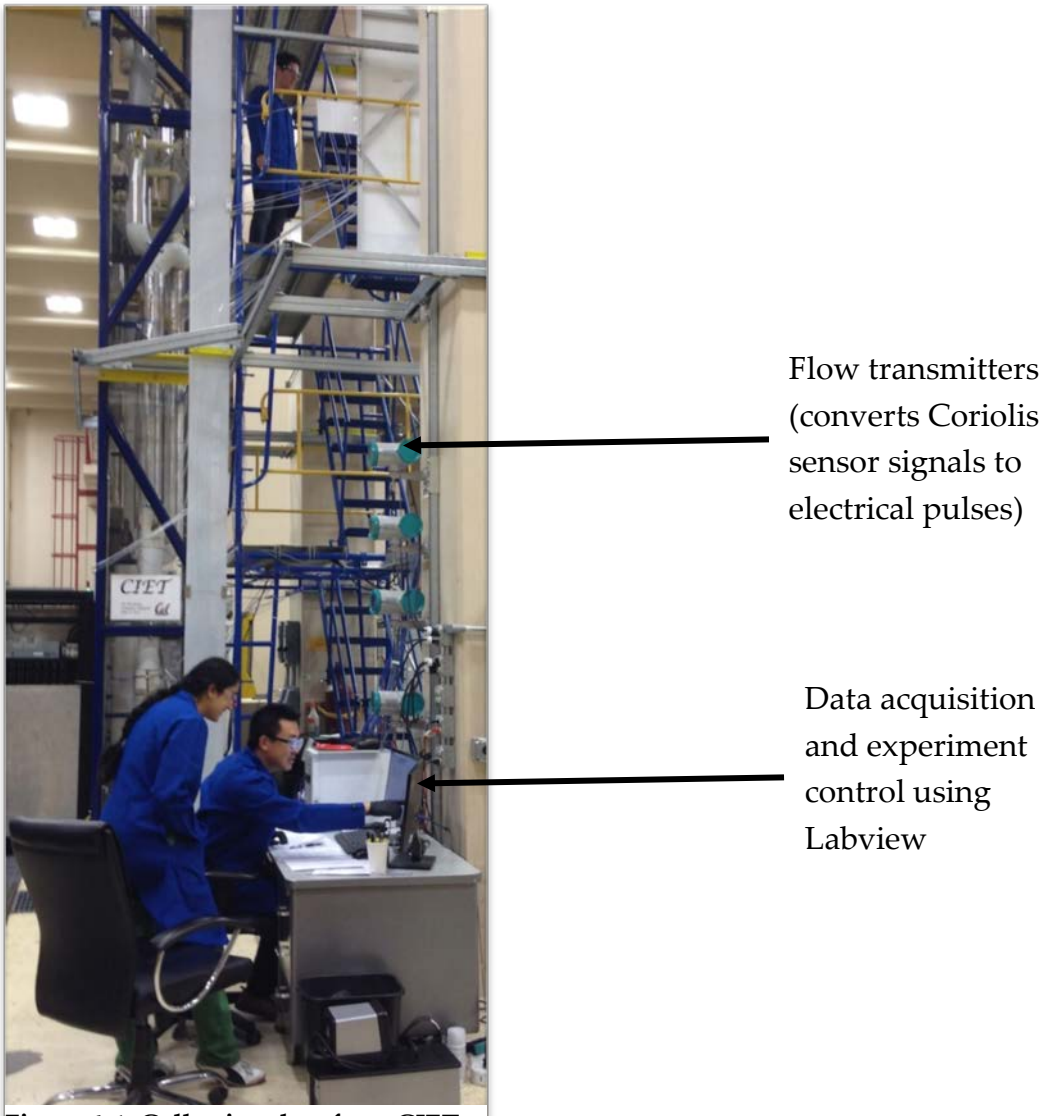

Figure 4-1: Collecting data from CIET. The height of the facility is about 10 m

Flownex has gone through an extensive V&V process, to ensure integrity of the code itself [74]. However it still needs to be validated for FHR and simulant oil systems, and this

chapter represents the initial effort. Flownex was used in the past to model accident transients in the PBMR [75], showing that it is a valid alternative to RELAP5-3D for systems modelling of advanced reactor systems.

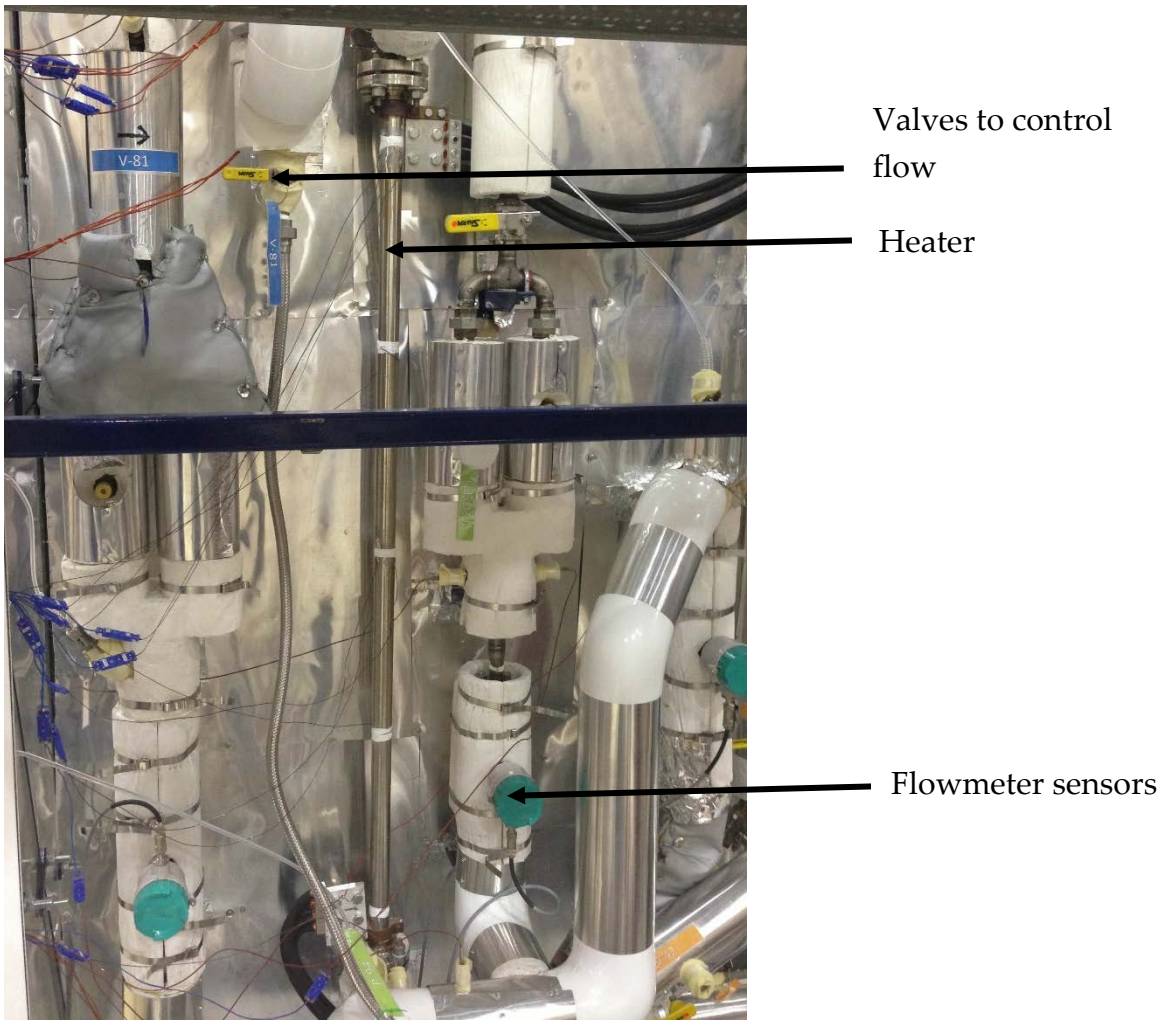

Figure 4-2: Close-up of the main loop of CIET

4.2 Multiphysics Codes

With increasingly available computing power it becomes possible to perform complex and computationally intense calculations. High fidelity multiphysics simulations can help determine plant behavior and specifically core temperatures during accident scenarios. These models require several closure equations in order to solve the governing equations simultaneously. The closure models are usually determined through experimental means. One example is the interfacial heat transfer coefficient determined in Chapter 3. A typical multiphysics model might involve a neutronics model of the pebble-bed reactor core coupled with thermal hydraulics models for conductive and convective heat transport. Thus, the more accurate the closure models, the better the

overall reactor predictions are using multiphysics codes. Another example might be coupling a thermal hydraulics systems code coupled to a 2D axisymmetric model of the pebble-bed reactor core, which would also require accurate closure models in the core.

4.3 Flownex Model Inputs and Geometric Parameters

In Flownex, each element shown in Figure 4-3 was transcribed into a pipe element made of the correct material (which determined pipe roughness) and the correct dimensions. The geometries of more complex elements such as the TCHX or the DHX were input using the overall flow area and wetted perimeter. The pipe elements were connected using nodes. Each node had an associated height specified. The 'insulated pipe' element was used to simulate the heat loss through the insulation. A heat transfer element was used to model heat exchangers such as the DHX and the TCHX. Internal heat generation was modelled in a pipe to simulate the heater.

Key dimensions and experimental parameters of the CIET loop are given in Table 4-1, including the height difference between the heat structures.

Table 4-1: Geometric and experimental parameters for CIET 1.0

	Units	**Value**
Height difference between midpoints of Heater and the DHX	m	1.81
Height difference between the midpoints of the DHX and the TCHX	m	3.98
Total height of the facility (from pump to highest expansion tank, Element 20 to Element 34 in Figure 4-3)	m	7
Heater power	kW	0.5-3

The boundary conditions modeled in Flownex are as follows:

- The temperature of the oil at the outlet of the TCHX was set to 46°C, as was the case in the experiment. This means that the average temperature in the DRACS loop was generally lower than in the main loop
- All the pipes are modeled with 0.05m of insulation around them, using the 'insulated pipe' element. This is essentially a regular pipe attached to a heat transfer element
- The ambient temperature was taken to be 20°C

- Ambient pressure was modeled at the highest points in each loop (primary and DRACS loops), where expansion tanks are located in the experimental facility

Several assumptions were taken into account in the Flownex model, and are as follows:

- The tubes in the DHX were assumed to solely transfer heat between the two loops, and not lose any heat to the surroundings
- The transition from laminar to turbulent was taken to be 2300 as it is in regular pipe flow

Instead of directly modeling expansion tanks (as one normally would in RELAP5-3D) an atmospheric boundary condition is implemented to mimic a free surface. A scripting was used for the custom friction factors for the flow meters, static mixers and the TCHX fan acting as the heat sink in the DRACS loop. The equations are shown in Table 4-2.

Table 4-2: Friction coefficients for components in CIET 1.0 based on experimental data

Component	Friction Coefficient based on Reynolds
Flowmeter	$f = 18.1 + 93006.9\,\mathrm{Re}^{-1.3476}$
Flow static mixer	$f = 21 + 4000\,\mathrm{Re}^{-1}$
TCHX fan	$f = 442.7 + 48022\,\mathrm{Re}^{-1}$

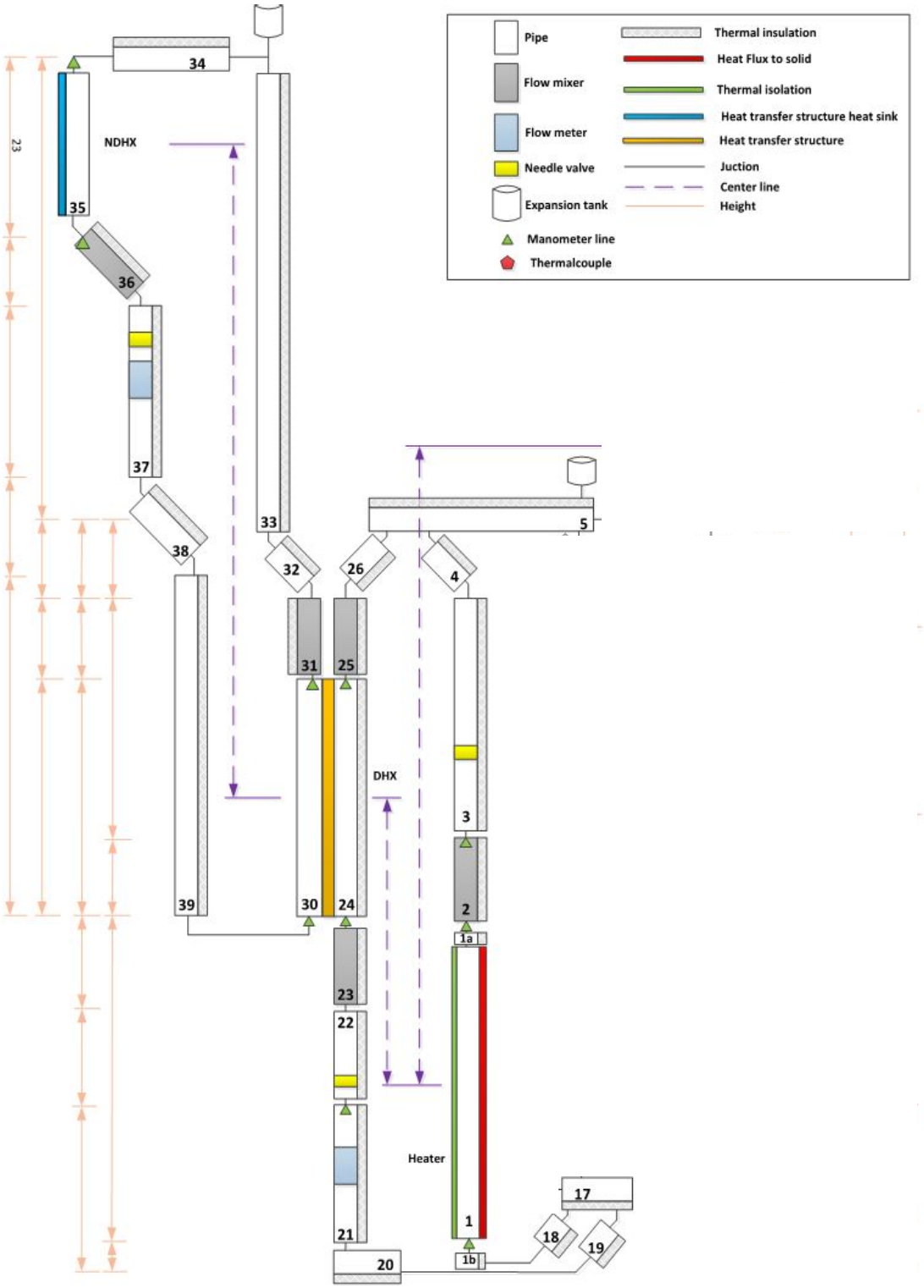

Figure 4-3: CIET flow loop modeling breakdown. The height from element 20 to element 34 (at the expansion tank) is 7m

4.4 Model Results and Discussion

The following sections present comparisons between the Flownex model results and the experiment data from CIET. Comparisons to RELAP5-3D and FANCY – a custom code developed specifically for modelling FHRs – are presented elsewhere [76][73][77].

4.4.1 Steady State Results

The graphs in Figure 4-4 to Figure 4-7 show some of the steady state results obtained from Flownex for the two loops. The error bars on the mass flow rate data from CIET are from the uncertainty in the mass flow rate readings using the Coriolis flowmeters. The heater power varied from 1kW to about 2.8kW. It can be seen that the mass flow rates in the DRACS loop are higher than in the main loop even though the heat addition to the DRACS loop is lower given the heat losses in the primary loop. This is because the height between the heat source and heat sink is larger in the DRACS loop.

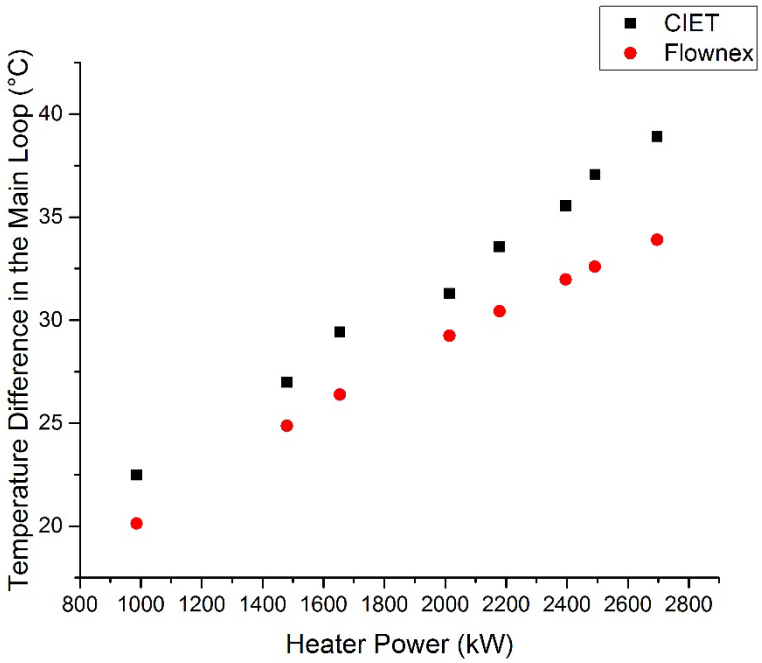

Figure 4-4: Temperature difference in the main loop (primary loop) against heat power

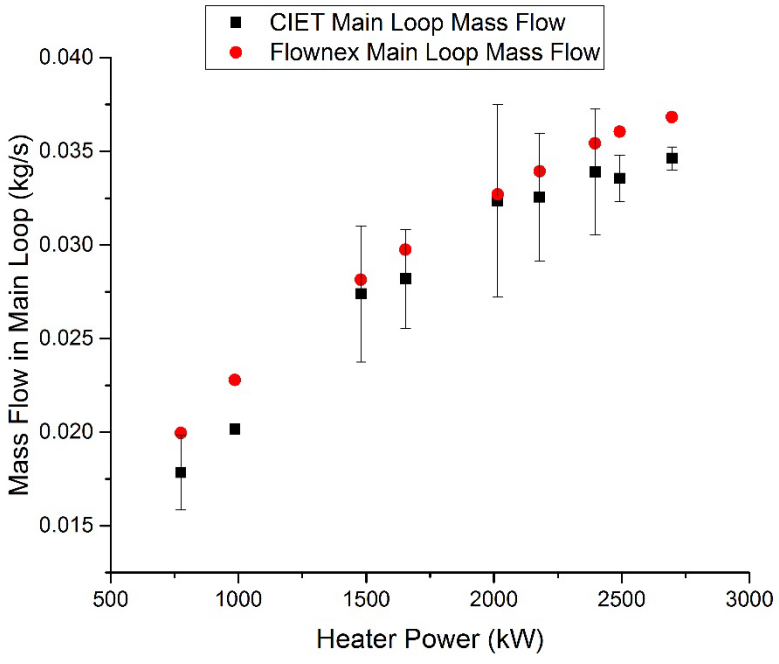

Figure 4-5: Mass flow rate in the main loop (primary loop) against heater power

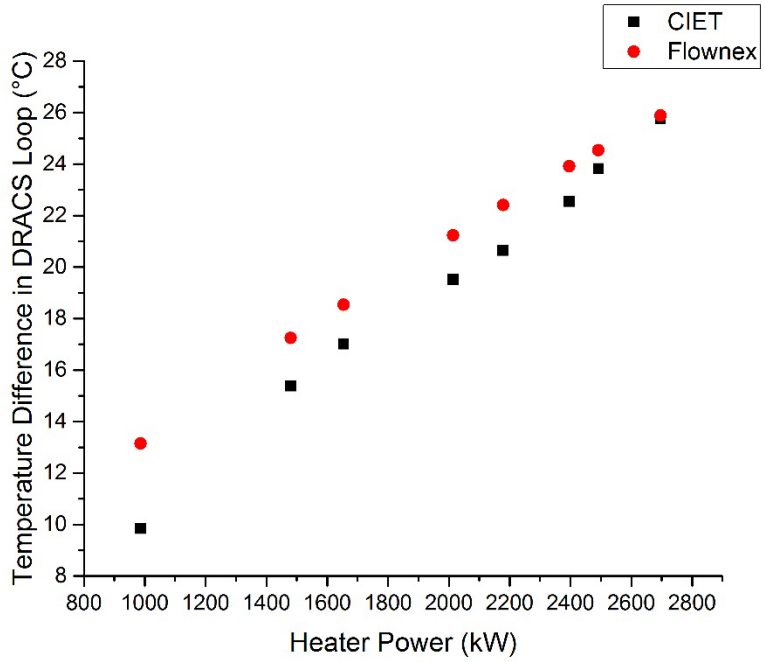

Figure 4-6: Temperature difference in the DRACS loop against heater power

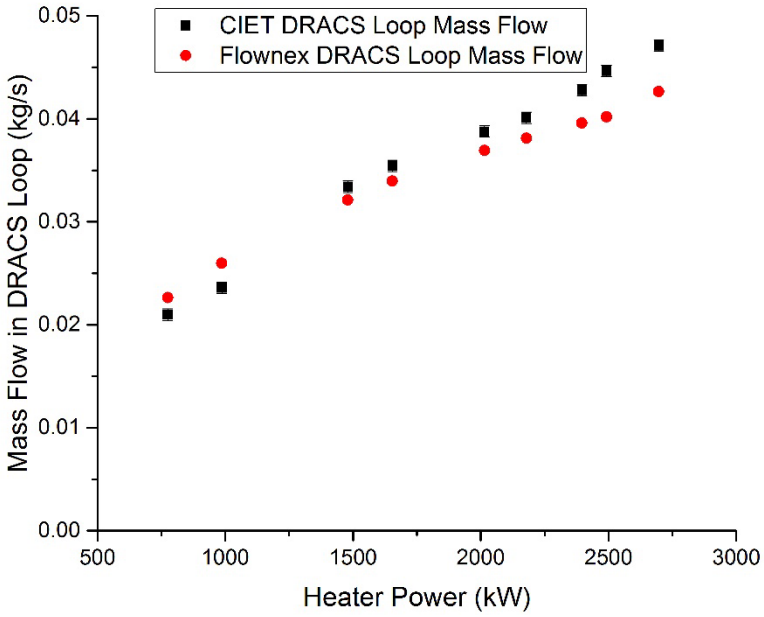

Figure 4-7: Mass flow rate in the DRACS loop against heater power

4.4.2 Effects of number of increments

Each component modeled in Flownex was split into 'increments' or control volumes. The number of increments was kept the same across the Flownex, RELAP and FANCY models initially. The Flownex model showed some sensitivity to the number of increments in the heat structures (i.e. the heater, DHX and TCHX) and the increments in the adjacent elements upstream and downstream of the heat structures. The heat structures and adjacent elements were divided into 85 increments each. The model showed inaccuracies with less than 85 increments. Any higher than 85, and the model computation time slowed down significantly. Changing the number of increments on regular pipe elements had little effect on the simulation results.

4.4.3 Transition Grashof number

In pipe flow, the transition from laminar to transitional flow occurs at a Reynolds number of around 2300. However in a closed loop the transition is expected to occur at a lower Reynolds number [78], given the number of elbows, fittings and short pipe lengths. It is possible that the friction coefficients in the pipes are modeled incorrectly, as the flow may be in the transition regime instead of the assumed laminar, especially at heater powers higher than 2kW. It is possible that inaccurate friction coefficients were used in the piping of the DRACS loop where the flow rates were higher. An incorrect friction factor will result in inaccurate mass flow rate results. The transition Reynolds number needs to be changed in the Flownex model. The friction models of the static mixers, flowmeters and the TCHX fan were assumed to be accurate given that they were experimentally measured.

4.5 Discussion

The results show that the Flownex calculated mass flow rates in the main loop were always higher than the experimental data, and were within 14%. The mass flow rates in the DRACS loop were within 11% of the experimental. The temperature differences in the main loop were within 8%. They were within 13% for the DRACS loop, except for the first point that was at a heater power of around 1000 W. The temperature difference in the main loop was calculated as the difference between the DHX shell-side inlet temperature and the inlet temperature to the heater. In the DRACS loop it was taken to be the difference between the TCHX inlet temperature and the DHX tube-side inlet temperature.

The discrepancy is likely to be because the pipe heat loss models need to be improved. In the main loop, Flownex underpredicts the temperature difference and overpredicts the mass flow rate. In the DRACS loop the mass flow rates are underpredicted while the temperature differences are overpredicted. This could be because the Flownex model is

overestimating the pipe heat losses in the hot leg of the DRACS flow loop. This would lead to lower calculated mass flow rates. Heat losses in the hot leg detract from the natural circulation mass flow rate whereas heat losses in the cold leg increase mass flow rates. In the main loop Flownex likely overestimates the heat losses in the cold leg, leading to higher than expected Flownex calculated mass flow rates. The average temperature in the main loop is higher than in the DRACS loop which would lead to larger pipe heat losses.

To verify the Flownex results, a simple energy balance was done on all the data. All the data satisfied $Q = mc_p \Delta T$, which means that the code was functioning as intended. Q is the heater or DHX power plus the heat losses through the pipes, m the mass flow rate, c_p the specific heat capacity of the Dowtherm A at the average loop temperature and ΔT the temperature difference in the loop.

4.6 Conclusions and Future Work

Flownex was used to model a scaled test facility using Dowtherm A as the simulant fluid. Steady state coupled natural circulation was simulated. It is important to diversify the codes used to simulate reactor system thermal hydraulics, and as such Flownex was found to be a good alternative to the more commonly used RELAP5-3D. More work needs to be done in developing and calibrating the existing models to accurately predict the experimental facility CIET. Once the steady state model is satisfactory (within 10% of the experimental data at all heater powers), transient simulations can be carried out. These include loss of forced circulation (LOFC) and natural circulation start-up whereby the system is initially at rest and the heater is suddenly powered on. If the transient results using the simulant fluid Dowtherm A are satisfactory, FHR systems can be modeled as well. Additionally it is crucial to perform experiments to empirically determine important closure relations for the purpose of doing multiphysics simulations.

5. CONCLUSIONS AND FUTURE WORK

It is clear that advanced nuclear reactors such as the Mk1 PB-FHR must play a significant role in providing reliable baseload electricity to the global population if we want to combat global warming and intermittencies in renewable energies. Designing a complex nuclear system in a heavily regulated environment comes with many intrinsic challenges. If we wish to develop these nuclear reactors at low costs, innovative experimental methodologies are integral to the design process. Nuclear energy is undoubtedly a crucial part of the global energy portfolio, and the work presented in this dissertation will improve the safety of the Mk1 PB-FHR.

The core objective of this dissertation was to develop a more fundamental understanding of heat transfer in fluoride salts. One of the aims of this dissertation was to show how vital experimental work is in understanding heat transfer phenomenology in FHRs. If the underlying phenomena are well characterized, cheaper experiments can be built before commercializing FHRs. The use of simulant fluids in designing and building scaled SETs and IETs was discussed, and emphasis was placed on the distortions that arise between the experiment (the model) and the prototypical system.

The full governing energy equations for the PB-FHR core can be simplified, which results in two important points: (1) If certain terms in the governing equations are negligible, ensuing simulations can be performed faster with little loss of accuracy and (2) scaled experiments using the simulant oil do not need to be designed to replicate phenomena that are negligible in the prototypical system, thereby facilitating experiment design and construction. For example, it was found that viscous dissipation can be neglected in the Mk1 PB-FHR core as it about 10^4 times smaller than the advection term during forced convection and 10^5 times smaller during natural circulation. The fluid thermal conduction term is enhanced by axial dispersion in the pebble-bed core, thereby counteracting the effect of the viscous dissipation. However both viscous dissipation and the thermal dispersion terms are several orders of magnitude smaller compared to the advection term. This is an important distinction to make between the PB-FHR and pebble-bed nuclear reactors cooled by helium.

The use of simulant oils such as Dowtherm A had been proposed but there was a lack of experimental evidence directly correlating simulant oil data with prototypical conditions. Under ideal circumstances, by matching the relevant non-dimensional numbers a perfect equivalence is expected between the two. Two straightforward experiments were designed and performed to show similitude between the simulant fluid and the fluoride salt. These experiments illuminated the importance of understanding distortions in the

expected similitude, and how they should influence experiment design in order to extract the best data to design FHR systems.

There is a dearth of experimental data regarding heat transfer in fluoride salts. Many pipe flow experiments have been performed, but little has been done in measuring external natural convection in fluoride salts. In this study, an isolated brass sphere was immersed in a bath of flinak with a uniform temperature. The temperatures of the sphere and the flinak were recorded throughout the transient until equilibrium conditions were attained. The experimental Nusselt number was extracted from the data, and compared to predictive correlations as well as data from parallel experiments done using Dowtherm A. The flinak Nusselt numbers were about three times smaller than the correlation or the Dowtherm A experiment, even taking radiation heat transfer into account. The cause for this was due to distortions in using a steady state correlation to predict a transient case. An isolated sphere in flinak is not under quasi-steady state conditions. This experiment provided new insight into designing SETs for FHRs. The key takeaway is that the time distortion is significant enough in fluoride salts with no heating element. This demonstrates the power of scaled experiments using simulant fluids – the ratio of volumetric heat capacities using the oil is much smaller than for flinak. It is extremely challenging to perform true steady state experiments with simulant oils as using pebbles as it is difficult to procure self-heating spheres. However, the experiments from this dissertation show that transient experimental runs using Dowtherm A can be approximated as quasi-steady, and can simulate steady-state conditions in fluoride salts.

The insights from the isolated sphere experiments lead to the design of another SET in which a cylindrical cartridge heater was immersed in Dowtherm A. A certain power was input into the heater and temperatures at three axial locations were measured as a function of time. This was a steady state natural convection experiment with heat transfer between the heater and the oil bath. The results were compared to data that was taken at ORNL for a parallel experiment with a cylindrical heater immersed in flinak. Since the time scale distortion was not present, a good match between the model and the prototypical conditions was expected. Most of the experimental data was within 10% of the flat plate correlations. The results from this study add to the evidence that by matching the relevant non-dimensional numbers similitude can be achieved between Dowtherm A and fluoride salts such as flinak.

The encouraging results from the previous two SETs lead to the design and construction of PBHTX in which an instrumented test section filled with copper pebbles was subject to an oscillatory temperature transient with a simulant oil Drakesol 260AT pumped through it. The aim of this study was to measure heat transfer coefficients (and specifically the Nusselt number) in pebble-beds for a range of Reynolds and Prandtl

numbers applicable to normal operation and natural circulation operation in the PB-FHR. The lessons learnt from previous SETs showed that because of the small ratio of volumetric heat capacity between the oil and copper, transient distortions would not play a significant role. The temperature of the oil entering the test section was pulsed with a constant frequency. This experimental technique resulted in collecting a wider range of data than was possible before, given the large temperature difference that was achieved. An analytical solution to the test section was shown to exist, which provided key insight into experimental parameters such as the optimal frequency to use. The experimental Nusselt numbers were within 32% of the Wakao correlation, with the experimental data generally being higher than the correlation. This showed that it is possible to use the Wakao correlation for core simulations, and that the heat transfer in the prototypical system might be better than predicted using the correlation. Radiation heat transfer was identified as a distortion, but through order of magnitude estimates it was concluded that it is likely to be small in the pebble-bed core during normal operation, and thus did not need to be modelled in the scaled experiment.

The use of frequency response techniques was shown to be successful in scaled experiments, pioneering a new experimental technique to study and simulate FHRs. Due to the modular design of PBHTX using flex piping and tri-clamp fittings, the same experimental setup can be used to study other heat structures or variations in the pebble-bed test sections. If the fluid-to-solid ratios can be matched between the prototypical and scaled models, then this methodology can be used in the future to better characterize the dynamic response of coolant-boundary structures in the PB-FHR. The method used to derive the analytical solution for the PBHTX test section can be extended to other scaled experiments in which an oscillatory function is imposed.

Most of the work in this dissertation focused on isolating a phenomenon of interest and studying it through experimental and computational means. However in the prototypical system phenomena are generally coupled to each other. Closure equations are required to perform system-wide calculations, and these are generally empirically derived, as is the case with the interfacial heat transfer coefficient in the reactor core, which was found in Chapter 3.

Modelling thermal hydraulic systems requires the use of systems codes. Code V&V was performed using Flownex, a code that had been used previously to study accident transients in the PBMR. Flownex was shown to be a satisfactory tool to model FHR systems. It is important to be able to provide diversification of simulation codes. A steady-state coupled natural circulation code was modeled and the ensuing results were compared to experimental data from CIET, an IET scaled to the PB-FHR. The results were with 14% of the experimental data, with 80% of the data within 10%. It was concluded

that improvements to the pipe heat loss model were necessary for Flownex to depict CIET for realistically. Natural circulation is generally a challenging phenomenon to model, and Flownex provides a valid alternative to RELAP5-3D. The next step is to model accident transients such as LOFC. It will also be equally important to model the start-up of natural circulation.

Ultimately, this dissertation shows that using scaled experiments to simulate FHR systems is a powerful way to not only gain a better understanding of the phenomena of interest, but also to attain directly relevant data for the Mk1 PB-FHR. This work shows a path forward for designing SETs for FHRs. The strategies delineated in this work regarding experimental design will allow FHRs to form a pivotal part of the nuclear industry and become a commercial reality.

5.1 Acknowledgements

This dissertation is based upon work supported by the National Science Foundation Graduate Research Fellowship under Grant No DGE 1106400 and supported by the US Department of Energy Office of Nuclear Energy University Programs Integrated Research Project.

BIBLIOGRAPHY

[1] "World Energy Needs and Nuclear Power." [Online]. Available: http://world-nuclear.org/information-library/current-and-future-generation/world-energy-needs-and-nuclear-power.aspx.

[2] International Energy Agency, "World Energy Outlook," 2015.

[3] C. Andreades, A. T. Cisneros, J. K. Choi, A. Y. K. Chong, M. Fratoni, S. Hong, L. R. Huddar, K. D. Huff, J. C. Kendrick, D. L. Krumwiede, M. R. Laufer, M. Munk, R. O. Scarlat, N. Zweibaum, E. Greenspan, X. Wang, and P. F. Peterson, "Design summary of the Mark-I pebble-bed, fluoride-salt-cooled, high-temperature reactor commercial power plant," *Nucl. Technol.*, vol. 195, pp. 223–238, 2016.

[4] H. Singh, R. P. Saini, and J. S. Saini, "A review on packed bed solar energy storage systems," *Renew. Sustain. Energy Rev.*, vol. 14, no. 3, pp. 1059–1069, 2010.

[5] P. L. Singh, S. D. Deshpandey, and P. C. Jena, "Energy for Sustainable Development Thermal performance of packed bed heat storage system for solar air heaters," *Energy Sustain. Dev.*, vol. 29, pp. 112–117, 2015.

[6] C. Andreades, A. T. Cisneros, J. K. Choi, A. Y. K. Chong, M. Fratoni, S. Hong, L. R. Huddar, K. D. Huff, D. L. Krumwiede, M. R. Laufer, M. Munk, R. O. Scarlat, N. Zweibaum, E. Greenspan, and P. F. Peterson, "Technical Description of the 'Mark 1' Pebble-Bed Fluoride-Salt-Cooled High-Temperature Reactor (PB-FHR) Power Plant," Berkeley, 2014.

[7] L. Huddar, R. Scarlat, D. Krumwiede, N. Zweibaum, and P. F. Peterson, "OVERVIEW OF PASSIVE SAFETY FEATURES AND TRANSIENT MODEL VALIDATION FOR THE PEBBLE-BED FLUORIDE-SALT COOLED , HIGH-TEMPERATURE NUCLEAR REACTOR (PB-FHR)," in *Proceedings of American Institute of Chemical Engineers (AICHE) Annual Conference*, 2013.

[8] A. Tokuhiro, "Integral-Effect and Separate-Effect Experiments: Facilities and Measurements," Idaho Falls, 2014.

[9] P. M. Bardet and P. F. Peterson, "Options for Scaled Experiments for High Temperature Liquid Salt and Helium Fluid Mechanics and Convective Heat Transfer," *Nucl. Technol.*, vol. 163, pp. 344–357, 2008.

[10] F. A. L. Dullien, "Pore Structure," in *Porous Media*, Second Edi., vol. 219, 1966, pp. 211–219.

[11] N. Kohtz and H. Haque, "Meeting fuel temperature limits in an HTR-Module

Reactor during depressurized core heat-up," *Nucl. Eng. Des.*, vol. 137, no. 1, pp. 115–124, 1992.

[12] M. A. Ebner, P. Sharpe, and S. M. Sohal, "Engineering Database of Liquid Salt Thermophysical and Thermochemical Properties, INL/EXT-10-18297," 2010.

[13] F. P. Incropera, D. P. DeWitt, T. L. Bergman, and A. S. Lavine, *Fundamentals of Heat and Mass Transfer*, vol. 6th. John Wiley & Sons, 2007.

[14] T. Wakao, N., Funazkri, "EFFECT OF FLUID DISPERSION COEFFICIENTS PARTICLE-TO-FLUID HEAT TRANSFER COEFFICIENTS IN PACKED BEDS," *Chem. Eng. Sci.*, 1979.

[15] D. a. Nield and A. Bejan, "Convection in Porous Media," pp. 31–47, 2013.

[16] A. Narasimhan, *Essentials of Heat and Fluid Flow in Porous Media*, 1st ed. CRC Press, Taylor & Francis Group.

[17] D. A. Nield, "Resolution of a Paradox Involving Viscous Dissipation and Nonlinear Drag in a Porous Medium," no. 1, pp. 349–357, 2000.

[18] I. By, G. Atomics, and D. O. F. Energy, "Graphite design handbook," *System*, no. September 1988, 1991.

[19] M. Kaviany, *Principles of Heat Transfer in Porous Media*, Second. Springer New York, 1995.

[20] M. Elsari and R. Hughes, "Axial effective thermal conductivities of packed beds," *Appl. Therm. Eng.*, vol. 22, no. 18, pp. 1969–1980, 2002.

[21] B. Alazmi and K. Vafai, "Analysis of Variable Porosity , Thermal Dispersion , and Local Thermal Nonequilibrium on Free Surface Flows Through Porous," *J. Heat Transfer*, vol. 126, no. June, pp. 389–399, 2004.

[22] C. T. Hsu and P. Cheng, "Thermal dispersion in a porous medium," *Int. J. Heat Mass Transf.*, vol. 33, no. 8, pp. 1587–1597, 1990.

[23] N. Wakao and S. Kaguei, *Heat Transfer in Packed Beds*. New York: Gordon and Breach Science, New York, 1982.

[24] G. Lauriat and R. Ghafir, "Forced Convective Heat Transfer in Porous Media," in *Handbook of Porous Media*, K. Vafai and H. A. Hadim, Eds. CRC Press, 2000, p. 201.

[25] H. Petersen, "The Properties of Helium: Density, Specific Heats, Viscosity, and Thermal Conductivity at Pressures from 1 to 100 bar and from Room Temperature to about 1800 K," Copenhagen, Denmark, 1970.

[26] F. Reitsma, “The Pebble Bed Modular Reactor Layout and Neutronics Design of the Equilibrium Cycle,” 2004.

[27] T. Dudley, W. Bouwer, P. de Villiers, and Z. Wang, “The Thermal–Hydraulic model for the pebble bed modular reactor (PBMR) plant operator training simulator system,” *Nucl. Eng. Des.*, vol. 238, no. 11, pp. 3102–3113, Nov. 2008.

[28] J. Ambrosek, M. Anderson, K. Sridharan, and T. Allen, “CURRENT STATUS OF KNOWLEDGE OF THE FLUORIDE SALT (FLiNaK) HEAT TRANSFER,” 2009.

[29] G. L. Yoder, “Examination of Liquid Fluoride Salt Heat Transfer,” in *Proceedings of ICAPP 2014*, 2014, pp. 1765–1774.

[30] L. Huddar and P. F. Peterson, “EXPERIMENTAL AND NUMERICAL INVESTIGATION OF TIME DEPENDENT NATURAL CONVECTION BOUNDARY LAYER FLOW OVER SPHERES IN FLUORIDE SALTS,” in *Advances in Thermal Hydraulics, Embedded Topic at the American Nuclear Society Annual Meeting*, 2014.

[31] A. Bejan and A. D. Kraus, *Heat Transfer Handbook*. John Wiley and Sons, 2003.

[32] S. Mohanty, S. Majumdar, M. Srinivasan, and U. S. N. R. Commission, “HTGR Graphite Core Component Stress Analysis Research Program – Task 1 Technical Letter Report,” 2011.

[33] OriginLab Corportation, “Origin 9.1 User Guide,” 2013. [Online]. Available: http://cloud.originlab.com/pdfs/Origin91_Documentation/English/Origin_9.1_User_Guide_E.pdf.

[34] S. W. Churchill, “COMPREHENSIVE , THEORETICALLY BASED , CORRELATING EQUATIONS FOR FREE CONVECTION FROM ISOTHERMAL SPHERES,” *Chem. Eng. Commun.*, vol. 24:4-6, pp. 339–352, 1983.

[35] N. Madsen, “The Functionally Near-Equivalency of Reynolds and Grashof Numbers,” in *AICHE journal*, 1975, pp. 609–610.

[36] A. Bejan, *Convection Heat Transfer*, Third Edit. Wiley Student Edition, 2004.

[37] S. Balachandar and M. Y. Ha, “Unsteady heat transfer from a sphere in a uniform cross-flow,” *Phys. Fluids*, vol. 13, no. 12, p. 3714, 2001.

[38] “Engineering Material Properties.” [Online]. Available: http://www.engineeringtoolbox.com/metal-alloys-densities-d_50.html. [Accessed: 05-Dec-2016].

[39] The Dow Chemical Company, “Dowtherm A Heat Transfer Fluid : Product

Technical Data," 1997.

[40] G. L. Yoder, M. Caja, and J. Jordan, "Liquid Fluoride Salt Experiment Using a Small Natural Circulation Cell," Oak Ridge, TN, 2014.

[41] A. Bejan, "External Natural Convection," in *Convection Heat Transfer*, 2004, pp. 185–186.

[42] Omega Engineering, "OMEGABOND High Temperature Air-Set Cements." [Online]. Available: http://www.omega.com/temperature/pdf/OB_OMEGABOND_AIR_SET.pdf. [Accessed: 01-Jan-2016].

[43] W. M. Rohsenow and H. Y. Choi, *Heat, Mass and Momentum Transfer*, First Edit. Englewood Cliffs, N.J.: Prentice-Hall, Inc, 1961.

[44] R. W. Fox, A. T. MacDonald, and P. J. Pritchard, *Introduction to Fluid Mechanics*, Sixth Edit. John Wiley & Sons, 2004.

[45] Y. Jaluria, "Natural Convection," in *Handbook of heat transfer*, 1997, pp. 410–499.

[46] A. Bejan and J. L. Lage, "The Prandtl Number Effect on the Transition in Natural Convection along a Vertical Surface," *J. Heat Transfer*, vol. 112, pp. 787–790, 1990.

[47] and B. S. Gebhart, Benjamin, Yogesh Jaluria, Roop L. Mahajan, *Buoyancy-Induced Flows and Transport*, Reference. Hemisphere Publishing Corporation, 1988.

[48] E. J. Le Fevre, "Laminar Free Convection from a Vertical Plane Surface," in *Proceedings of the 9th International Congress of Applied Mechanics*, 1956, p. Vol 4 168-174.

[49] N. Wakao and T. Funazkri, "Effect of fluid dispersion coefficients on particle-to-fluid mass transfer coefficients in packed beds," *Chem. Eng. Sci.*, vol. 33, pp. 1375–1384, 1978.

[50] P. J. Handley, D., Heggs, "THE EFFECT PACKING OF THERMAL CONDUCTIVITY BED OF THE MATERIAL ON TRANSIENT IN A FIXED," *Int. J. Heat Mass Transf.*, vol. 12, pp. 549–570, 1969.

[51] N. Wakao and S. Kagei, "Heat Transfer Coefficients," in *Heat Transfer in Packed Beds*, 1st Editio., Gordon and Breach Science, New York, 1982, pp. 266–272.

[52] L. Huddar, J. C. Kendrick, C. Poresky, X. Wang, and P. F. Peterson, "APPLICATION OF FREQUENCY RESPONSE METHODS IN SEPARATE AND INTEGRAL EFFECTS TESTS FOR MOLTEN SALT COOLED AND FUELED REACTORS," in *High Temperature Reactors Embedded Topic at the American Nuclear*

Society Winter Meeting, 2016.

[53] N. Wakao and S. Kagei, *Heat and Mass Transfer in Packed Beds*. Gordon and Breach Science, New York, 1982.

[54] L. P. Carillo, "Convective heat transfer for viscous fluid flow through a metallic packed bed," *Interciencia*, vol. 30, no. 2, p. 81, 2005.

[55] D. Geb and I. Catton, "Internal Heat Transfer Coefficient Determination in a Packed Bed From the Transient Response Due to Solid Phase Induction Heating," vol. 134, no. April, 2012.

[56] P. J. Handley, D., Heggs, "Momentum and Heat Transfer Mechanisms in Regular Shaped Packings," *Trans. Inst. Chem. Eng.*, vol. 46, no. 9, 1968.

[57] H. Littman, R. G. Barile, and A. H. Pulsifer, "Gas-Particle Heat Transfer Coefficients in Packed Beds at Low Reynolds Numbers," *I EC Fundam.*, vol. 7, no. 4, pp. 554–561, 1968.

[58] D. J. Gunn and J. F. C. De Souza, "Heat transfer and axial dispersion in packed beds," *Chem. Eng. Sci.*, vol. 29, pp. 1363–1371, 1974.

[59] T. W. Kerlin, E. M. Katz, A. L. Chen, J. Thakkar, and S. Chang, "Dynamic Testing in Nuclear Power Plants for Model Validation," in *Transactions of the ASME*, 1976, vol. September, no. 76.

[60] S. J. Ball and T. W. Kerlin, "Stability Analysis of the Molten-Salt Reactor Experiment," Oak Ridge, TN, 1965.

[61] T. W. Kerlin, *Frequency Response Testing in Nuclear Reactors*. New York and London: Academic Press, 1974.

[62] P. M. Bardet, C. Debonnel, J. Freeman, G. Fukuda, B. Supiot, and P. F. Peterson, "Dynamics of Liquid-Protected Fusion Chambers," *Fusion Sci. Technol.*, vol. 47, pp. 626–632, 2005.

[63] L. Huddar and P. F. Peterson, "EXPERIMENTAL STRATEGY FOR THE DETERMINATION OF HEAT TRANSFER COEFFICIENTS IN PEBBLE-BEDS COOLED BY FLUORIDE SALTS," in *NURETH-16, Chicago, IL, August 30-September 4, 2015*, 2015, pp. 1659–1675.

[64] N. Zweibaum and E. Al, "Design of the compact integral effects test facility and validation of best estimate models for fluoride-salt-cooled, high-temperature reactors," *Nucl. Technol. (in Press.*

[65] Eemax, "Electric Tankless Water Heaters (EX95DL)," no. 3556. 2014.

[66] D. C. Company, "DOWTHERM™ HIGH TEMPERATURE THERMAL FLUIDS MATERIAL COMPATIBILITY INFORMATION, Dow Chemical Company," 2011.

[67] N. S. S. C. (KTA), "Nuclear Safety Standards Commission (KTA) Reactor Core Design of High-Temperature Gas-Cooled Reactors Part 2 : Heat Transfer in Spherical Fuel Elements (June 1983)," 1983.

[68] D. L. Dixon, A. G., Cresswell, "Theoretical Prediction of Effective Heat Transfer Parameters in Packed Beds," *AIChE J.*, vol. 25, no. 4, pp. 663–676, 1979.

[69] Omega Engineering, "Thermocouples - using thermocouples in temperature measurements," 2016. [Online]. Available: http://www.omega.com/prodinfo/thermocouples.html. [Accessed: 10-Jul-2016].

[70] E. S. Chaleff, T. Blue, and P. Sabharwall, "Radiation Heat Transfer in the Molten Salt FLiNaK," *Nucl. Technol.*, vol. 196, no. 1, pp. 1–9, 2016.

[71] Mikron Instrument Company, "Table of Emissivity of Various Surfaces."

[72] W. L. Oberkampf and T. G. Trucano, "Verification and validation benchmarks," *Nucl. Eng. Des.*, vol. 238, no. 3, pp. 716–743, 2008.

[73] N. Zweibaum, Z. Guo, J. C. Kendrick, and P. F. Peterson, "Design of the Compact Integral Effects Test Facility and Validation of Best-Estimate Models for Fluoride Salt-Cooled High-Temperature Reactors," *Nucl. Technol.*, vol. 196, no. 3, 2016.

[74] Flownex SE, *Flownex Theory Manual*, no. October. 2015.

[75] P. A. J. Van Rensburg, "UNCERTAINTY ANALYSIS FOR A DEPRESSURISED LOSS OF FORCED," in *Proceedings of ICONE14 International Conference on Nuclear Engineering*, 2006, pp. 1–10.

[76] Z. Guo, N. Zweibaum, M. Shao, L. R. Huddar, P. F. Peterson, and S. Qiu, "Development of the FHR advanced natural circulation analysis code and application to FHR safety analysis," *Prog. Nucl. Energy*, vol. 91, pp. 56–67, 2016.

[77] N. Zweibaum, "Experimental Validation of Passive Safety System Models : Application to Design and Optimization of Fluoride-Salt-Cooled , High-Temperature Reactors," 2015.

[78] B. T. Swapnalee and P. K. Vijayan, "A generalized flow equation for single phase natural circulation loops obeying multiple friction laws," *Int. J. Heat Mass Transf.*, vol. 54, no. 11–12, pp. 2618–2629, 2011.

[79] "AMDX-10-8, SEC Heat Exchangers." Belfast, Canada, 2015.

APPENDIX A FLOWNEX INPUT AND OUTPUT

This appendix shows an example of the input and output files from Flownex that were used in the calculations for Chapter 4. The heater power in this example was 1.479 kW. Figure A-1 shows an example input. Flownex has a graphical user interface.

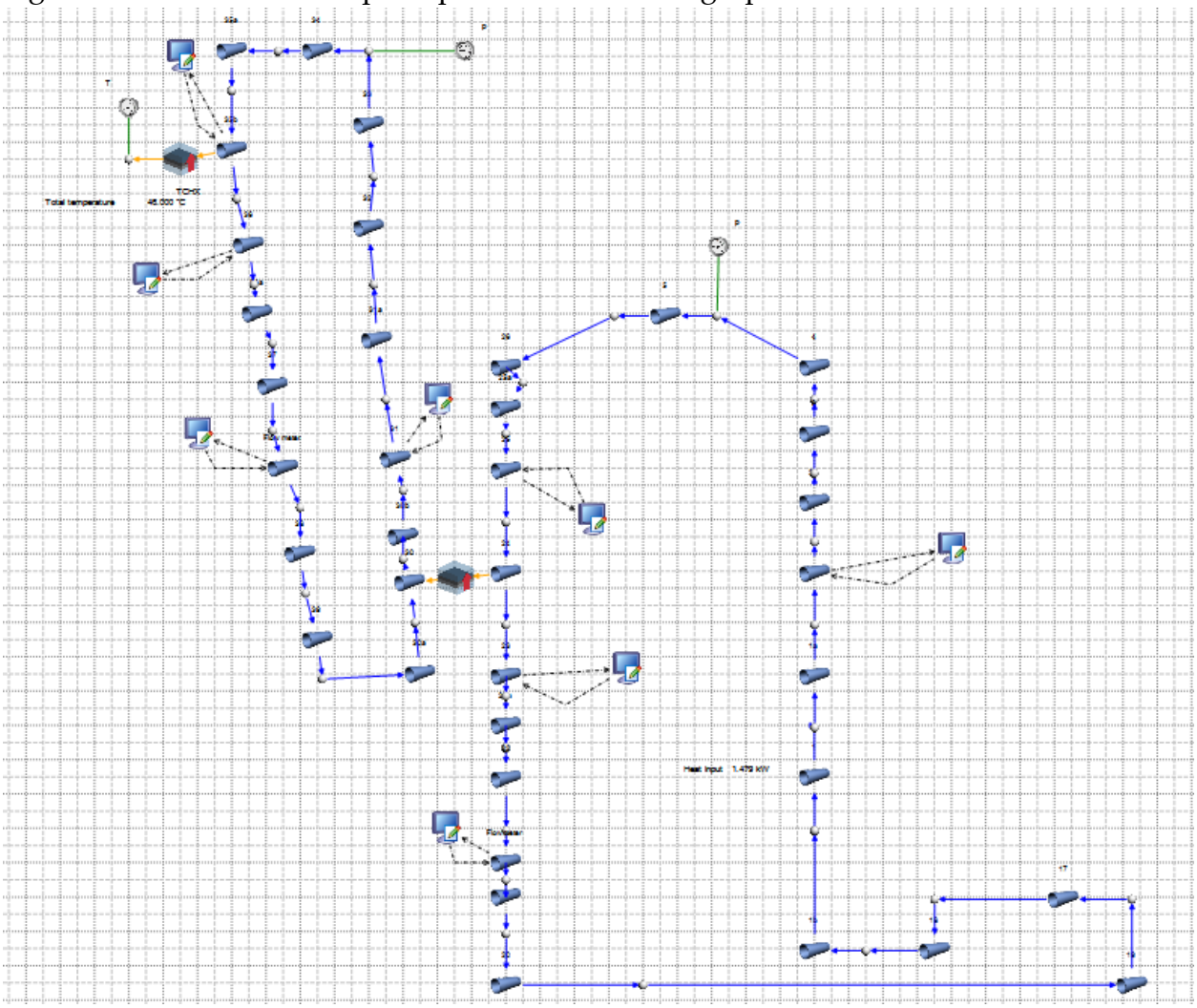

Figure A-1: Flownex example input, with pipe elements, heat transfer elements and scritping elements to input custom friction factors in certain components

An example output is shown in Figure A-2. This is the output for the heater element. Results from each pipe, node or heat transfer element can be extracted in a similar way.

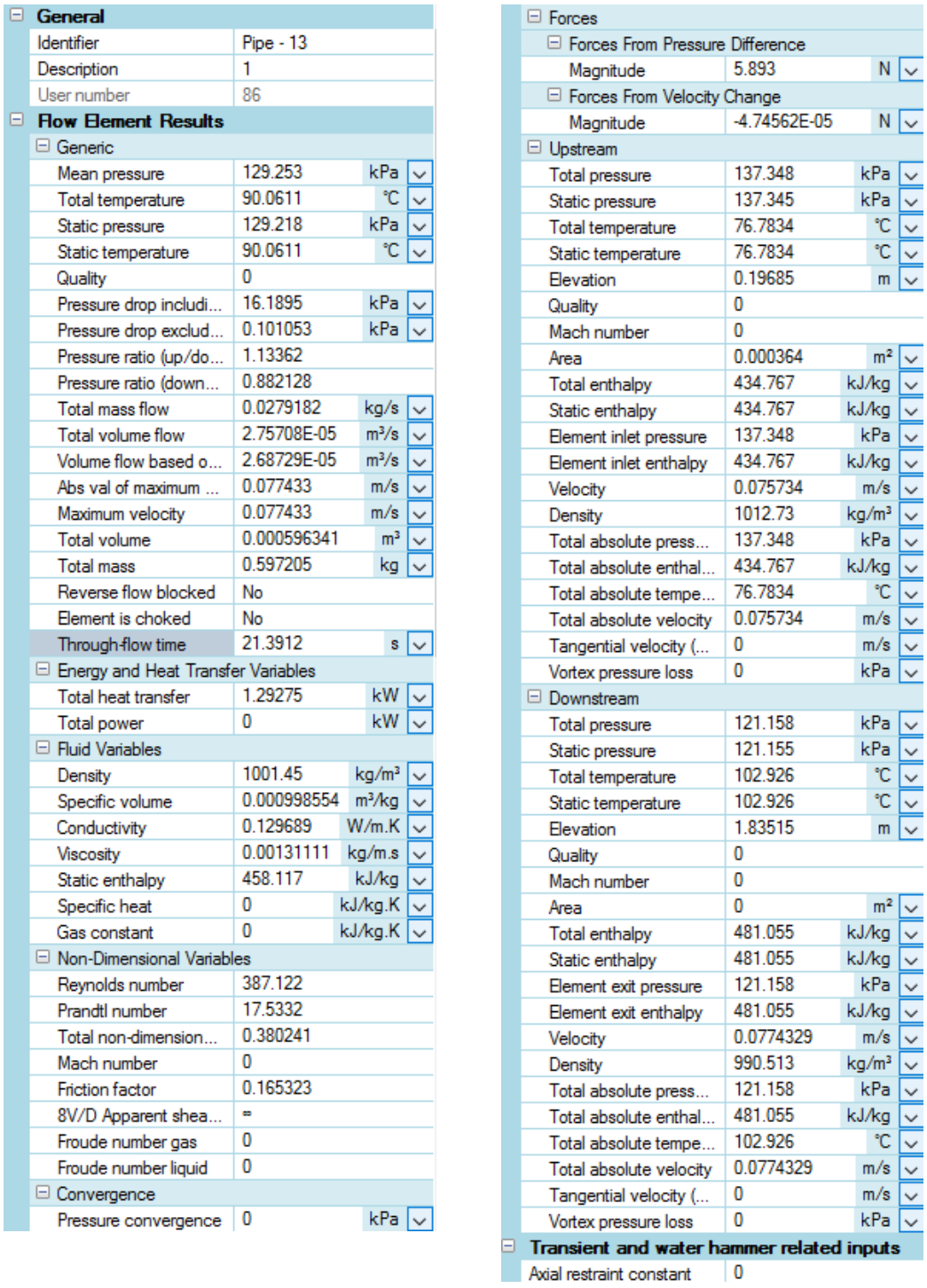

General		
Identifier	Pipe - 13	
Description	1	
User number	86	
Flow Element Results		
Generic		
Mean pressure	129.253	kPa
Total temperature	90.0611	°C
Static pressure	129.218	kPa
Static temperature	90.0611	°C
Quality	0	
Pressure drop includi...	16.1895	kPa
Pressure drop exclud...	0.101053	kPa
Pressure ratio (up/do...	1.13362	
Pressure ratio (down...	0.882128	
Total mass flow	0.0279182	kg/s
Total volume flow	2.75708E-05	m³/s
Volume flow based o...	2.68729E-05	m³/s
Abs val of maximum ...	0.077433	m/s
Maximum velocity	0.077433	m/s
Total volume	0.000596341	m³
Total mass	0.597205	kg
Reverse flow blocked	No	
Element is choked	No	
Through-flow time	21.3912	s
Energy and Heat Transfer Variables		
Total heat transfer	1.29275	kW
Total power	0	kW
Fluid Variables		
Density	1001.45	kg/m³
Specific volume	0.000998554	m³/kg
Conductivity	0.129689	W/m.K
Viscosity	0.00131111	kg/m.s
Static enthalpy	458.117	kJ/kg
Specific heat	0	kJ/kg.K
Gas constant	0	kJ/kg.K
Non-Dimensional Variables		
Reynolds number	387.122	
Prandtl number	17.5332	
Total non-dimension...	0.380241	
Mach number	0	
Friction factor	0.165323	
8V/D Apparent shea...	∞	
Froude number gas	0	
Froude number liquid	0	
Convergence		
Pressure convergence	0	kPa

Forces		
Forces From Pressure Difference		
Magnitude	5.893	N
Forces From Velocity Change		
Magnitude	-4.74562E-05	N
Upstream		
Total pressure	137.348	kPa
Static pressure	137.345	kPa
Total temperature	76.7834	°C
Static temperature	76.7834	°C
Elevation	0.19685	m
Quality	0	
Mach number	0	
Area	0.000364	m²
Total enthalpy	434.767	kJ/kg
Static enthalpy	434.767	kJ/kg
Element inlet pressure	137.348	kPa
Element inlet enthalpy	434.767	kJ/kg
Velocity	0.075734	m/s
Density	1012.73	kg/m³
Total absolute press...	137.348	kPa
Total absolute enthal...	434.767	kJ/kg
Total absolute tempe...	76.7834	°C
Total absolute velocity	0.075734	m/s
Tangential velocity (...	0	m/s
Vortex pressure loss	0	kPa
Downstream		
Total pressure	121.158	kPa
Static pressure	121.155	kPa
Total temperature	102.926	°C
Static temperature	102.926	°C
Elevation	1.83515	m
Quality	0	
Mach number	0	
Area	0	m²
Total enthalpy	481.055	kJ/kg
Static enthalpy	481.055	kJ/kg
Element exit pressure	121.158	kPa
Element exit enthalpy	481.055	kJ/kg
Velocity	0.0774329	m/s
Density	990.513	kg/m³
Total absolute press...	121.158	kPa
Total absolute enthal...	481.055	kJ/kg
Total absolute tempe...	102.926	°C
Total absolute velocity	0.0774329	m/s
Tangential velocity (...	0	m/s
Vortex pressure loss	0	kPa
Transient and water hammer related inputs		
Axial restraint constant	0	

Figure A-2: Example output data for the heater element